Spectroscopic techniques for monitoring carbonation reactions and quantification of their products

PETRA KRISTOVA

A thesis submitted in partial fulfilment of the requirements of the University of Brighton for the degree of Doctor of Philosophy

July 2016

Abstract

Synthetic and naturally occurring calcium and magnesium carbonate minerals are widely used in a range of industrial and environmental applications where the mineral quality and purity is often critical for their intended use. Hence accurate characterisation of the mineral assemblages is essential. Equally important is an understanding of the chemical and physical pathways leading to mineral formation and their roles in carbon sequestration from greenhouse gases. This study investigates the application of Raman and infrared spectroscopies to Ca-Mg carbonate analysis.

A full quantitative calibration has been achieved for quaternary mixtures by Raman spectroscopy (RS) employing monovariable and multivariable methods. The method was validated by X-ray powder diffraction (XRD). The lowest error on component values was obtained by Principal Component Regression with application of Standard Normal Variate. The quantifications show that RS is comparable to XRD.

The effect of particle size on the fundamental vibrations of the [CO_3^{2-}] anion in calcite is investigated by mid-infrared and RS. While the effect of particle size on the infrared signature of internal modes of the [CO_3^{2-}] anion is well documented, this thesis documents associated changes in Raman spectra as a function of particle size. With decreasing size spectral contrast diminishes and changes in the relative ratios of the internal modes occur. For RS the turnaround from optically thick to thin material occurs in the 42-59 μm size range with further changes occurring at ≤ 5 μm.

RS was also utilized to monitor carbonate reaction kinetics after dissolution of [$Mg(OH)_2$] by CO_2 sparging in the presence of calcium salts at 35 °C, 30 days duration. Four experiments employing different calcium salts, Ca:Mg ratios and effect of hydromagnesite [$Mg_5(CO_3)_4(OH)_2.xH_2O$] seeding were examined utilizing vibrational spectroscopies, XRD and SEM. Results suggest that carbonate mineral paragenesis is driven by geochemical feedback between a range of calcium and magnesium carbonate dissolution-precipitation events where decomposition of nesquehonite [$Mg(HCO_3,OH)\cdot 2H_2O$] leads to formation of magnesium carbonate hydrates [$Mg_5(CO_3)_4(OH)_2.xH_2O$]. XRD confirmed that these hydrated phases contain 8 and/or 5 molecules of crystalline water. However, RS cannot distinguish these phases. Traces of barringtonite [$Mg(CO_3)\cdot 2H_2O$] found at the end of experiments were interpreted as an indicator of incongruent dissolution of nesquehonite. Findings suggest that the Raman active ν_1 mode of barringtonite is situated at *ca.* 1094-1095 cm^{-1}.

The limitations of Raman analysis in the context of mineral assemblage quantification, short range ordering and particle size effects are discussed in the context of these findings.

Majority of this thesis has been published in three research papers:

Kristova, P., Hopkinson, L., Rutt, K., Hunter, H. and Cressey, G. (2013) Quantitative analyses of powdered multi-minerallic carbonate aggregates using a portable Raman spectrometer. *American Mineralogist,* 98, 401-409.

Kristova, P., Hopkinson, L. J., Rutt, K. J., Hunter, M. A. and Cressey, G. (2014) Carbonate mineral paragenesis and reaction kinetics in the system MgO–CaO–CO_2–H_2O in presence of chloride or nitrate ions at near surface ambient temperatures. *Applied Geochemistry*, 16-24.

Kristova, P., Hopkinson, L. J. and Rutt, K. J. (2015) The Effect of the Particle Size on the Fundamental Vibrations of the [CO_3^{2-}] Anion in Calcite. *Journal of Physical Chemistry A,* 119, 4891-4897.

Table of Contents

List of Figures

List of Tables

Abbreviations

ACC - amorphous calcium carbonate

arbitr. units - arbitrary units

ATR-IR - attenuated total reflectance mid-infrared

CCD - detector, charge-coupled device

CNMNC - Commission on New Minerals and Mineral Names

EPMA - elemental analysis, electron probe micro-analyser

FWHM - full width at half maximum

HCMC - hydrous Ca-bearing magnesium carbonate

HM - hydromagnesite

ICDD - International Centre for Diffraction Data

IMA - International Mineralogical Association

IR - infrared or infrared spectroscopy

MHC – monohydrous calcite

MSC - multiplicative scatter correction

N - nesquehonite

N/A – not applicable

NIR - near-infrared spectroscopy

NIST - National Institute of Standards and Technology

PCR+ - Principal Component Regression

PLS - Partial Least Squares

PSA - particle size analyser

PSD - position sensitive detector

QPA - quantitative phase analysis

R – Raman

rpm - revolutions per minute

RS - Raman spectroscopy

SEM - scanning electron microscopy

SNV - standard normal variation

XRD - X-ray diffraction

Symbols

A - absorbance

α - absorption coefficient

c - represents concentration (in moles per litre),

d - mean photon path length

D_3h - molecular symmetry of carbonate anion (planar triangle)

λ - wavelength

ε - constant, the molar absorptivity

I - the intensity of light passing through sample

I_o - the intensity of light passing through reference, in RS I_o represents intensity of excitation light

I(v) - represents the Raman intensity at Raman shift *(v)*

k - imaginary component of refractive index

l - refers to the path length given in centimetres

n - refers to number of sample molecules, i.e. sample concentration

n - real component of refractive index

N (n) - number of atoms in molecule (primitive unit cell)

v_1 - symmetric stretch (Raman active),

v_2 - out-of-plane bend (IR active),

v_3 - asymmetric stretch (Raman and IR active)

v_4 - in-plane bend (Raman and IR active)

pCO_2 - partial pressure of CO_2

r(v) - covers a number of factors such as spectrometer response, self-absorption, molecular scattering properties of a measured sample

T - transmittance

wt % - weight percent

w/w % - weight in weight percent

Symbols for symmetry operations, group theory and vibrational spectroscopy are omitted here and explained in respective tables:

Table 1.2: Symmetry operations and their symbols (page 25)

Table 1.3: Calcite (D3d) symmetries (e.g. Burns 1977; Lou et al. 2007), irreducible ($\chi_m(R)$) and reducible representations ($\chi(R)$). (page 28)

Acknowledgement

I would like to express my sincere gratitude to my supervisors Dr. Laurence Hopkinson and Dr. Ken Rutt for their support, help and encouragement. Their willingness to motivate and inspire me contributed tremendously to my project.

I also thank to Dr. Hazel Hunter and Dr. Gordon Cressey from Natural History Museum in London for their help with X-ray powder diffraction analyses. I would like to take this opportunity to thank editors of American Mineralogist, Applied Geochemistry and Journal of Physical Chemistry, reviewers Prof. Frost, Prof. Jehlicka and all anonymous reviewers of our three publications coming from this research project for their very useful comments.

I am grateful to my colleagues and especially to my line manager Christine Smith for her support and care during my research. University of Brighton is thanked for support.

I would like to thank my family for never-ending love and support and mainly to my husband who supported me in the hardest moments during my work, pregnancy and finally motherhood alongside this PhD thesis. I would never finish without you!

Declaration

I declare that the research contained in this thesis, unless otherwise formally indicated within the text, is the original work of the author. The thesis has not been previously submitted to this or any other university for a degree, and does not incorporate any material already submitted for a degree.

Signed

Dated

1 Literature review

1.1 Introduction

The magnesium and calcium bearing carbonates represent an important mineral group which is mined extensively. Select carbonates are also synthesised on an industrial scale. Basic magnesium and calcium carbonate minerals (e.g. hydromagnesite [$Mg_5(CO_3)_4(OH)_2{\cdot}4H_2O$], magnesite [$MgCO_3$], calcite [$CaCO_3$] etc.) together with calcium magnesium double carbonates (e.g. huntite [$CaMg_3(CO_3)_4$], dolomite [$CaMg(CO_3)_2$]) are widely used in many industrial sectors e.g. pharmaceutical and cosmetic industries, paint formulations and bulk applications including concrete and magnesia (MgO) production. In recent years, they have also been utilized as flame retardants in plastics (as customized mixtures) for their beneficial thermal, rheological properties and whiteness (Haurie 2005; Hollingberry and Hull 2010, 2012).

The quality and purity of synthetic and naturally processed carbonate mineral assemblages varies greatly and is often critical for their intended use. Hence accurate characterisation of natural and processed mineral assemblages is essential. Equally important is an understanding of the chemical and physical pathways leading to mineral formation and transformation and their roles in carbon sequestration from greenhouse gases (e.g., Hales et al., 2008; Frost et al., 2008a). Sequestration of atmospheric and waste CO_2 gases is another potentially important process. Carbonate mineral formation is frequently very complex and does not follow thermodynamically predicted equilibrium (Morse and Casey 1988). This field of research is considered an important precursor to the eventual aim of storing carbon dioxide in relatively stable minerals (Ballirano et al., 2013), including many magnesium and calcium bearing carbonates, by pumping liquefied carbon dioxide several kilometres below ground into magnesium-rich silicate rock types such as serpentinites (e.g. Cipolli et al., 2004; Orlando et al., 2012). Hence low temperature reaction kinetics of carbonate minerals and their thermal stability need to be understood. In the case of magnesium carbonates one of the likely reaction pathways to magnesite (the most stable Mg carbonate under ambient Earth surface conditions) is assumed to be via nesquehonite [$MgCO_3{\cdot}3H_2O$] to dypingite [$Mg_5(CO_3)_4(OH)_2.5H_2O$] (or hydromagnesite [$Mg_5(CO_3)_4(OH)_2.4H_2O$]) transitions. Hales et al., (2008) have determined safe sequestration of CO_2 in synthetic nesquehonite, defining its structure to

be [$Mg(OH)(HCO_3).2H_2O$] by hot-stage Raman spectroscopy and showing a stability up to 400 °C. A study by Frost et al., (2008) on the thermal stability of dypingite [$Mg_5(CO_3)_4(OH)_2 \cdot XH_2O$] suggests that atmospheric CO_2 removal by geosequestration is feasible providing that the temperature does not exceed 350-355 °C. However natural near surface aqueous solutions capable of yielding magnesium carbonates overwhelmingly contain at least some calcium. Accordingly, the aims of this thesis are two-fold. Firstly, to evaluate Raman and near-infrared vibrational spectroscopic techniques in relation to accurate assessment of carbonate mineral assemblages, thereby to construct methods for quantitative analysis of carbonate mineral assemblages. Secondly, to employ these techniques to examine the kinetics of experimental low temperature carbonate reaction pathways in the system $CaO\text{-}MgO\text{-}H_2O\text{-}CO_2$.

1.2 Magnesium and calcium carbonate minerals

1.2.1 Hydrated and basic calcium carbonate minerals

Six forms of calcium carbonate have been identified (e.g., Lipmann 1973). Polymorphic calcium carbonate minerals [$CaCO_3$] are calcite, aragonite, vaterite, amorphous calcium carbonate and two hydrated forms, a monohydrate i.e. monohydrous calcite (MHC) [$CaCO_3 \cdot H_2O$], and a hexahydrate called ikaite [$CaCO_3 \cdot 6H_2O$]. The polymorphic minerals calcite and aragonite are two of the most investigated and widespread naturally occurring carbonate minerals (e.g., Morse et al., 2007).

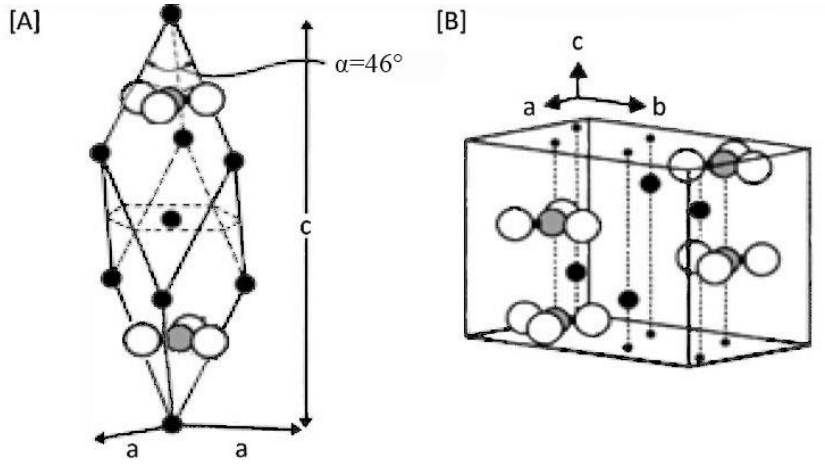

Figure 1.1: Unit cells of calcium carbonate polymorphs calcite [A] and aragonite [B]. Adapted after Doner and Lynn (1989) and Terada et al., (2003).

Calcite forms rhombohedral (trigonal) crystal units with a unit cell containing two carbonate ions pointing in opposite direction (Figure 1.1). Calcite precipitates from water in many different environments (marine, freshwater) and also is an important biomineral forming shells of invertebrates (e.g. molluscs) (Nesse 2012). Most of the calcite deposited as limestone is of a biologic origin (Nesse 2012). There are several methods for laboratory precipitation of calcium carbonate minerals differentiated by the source of [CO_3^{2-}], other ions, temperature used, presence of additives etc. Firstly, calcium carbonate can be yielded by mixing two solutions, a solution of calcium salt (chloride, nitrate, sulphate, hydroxide) and a solution of soluble carbonate (sodium, ammonium) (Lipmann 1973;

Andersen and Brecevic 1991, Kitamura et al., 2002). Secondly, precipitation of calcium carbonate can be achieved by bubbling CO_2 gas through calcium hydroxide slurry (Uebo et al., 1992; Domingo et al., 2006; Kedra-Krolik and Gyericz 2009). Synthetic calcite polymorphs can be precipitated from solutions of a calcium salt (calcium chloride) and sodium carbonate, although there are variations in conditions and length of the experiments described in the literature, e.g. 7 days of stirring at room temperature (Dandeu et al., 2006), precipitation at 30 °C of mixed phases of calcite and vaterite transforming to pure calcite after 3 hours of stirring (Nan et al., 2007).

Aragonite forms needle-like crystals of orthorhombic crystal structure with four carbonate ions in its unit cell. Conditions favourable for crystallization of aragonite are near-surface low temperature deposits which can include warm sea, cave and hot spring environments and the presence of Mg^{2+} ions in solution (e.g. Park et al., 2008; Hu et al., 2009, Nesse 2012). Aragonite is also often found as a metamorphic mineral (in glaucophane schist rocks) at low temperatures (below 300 °C) and high pressure (e.g. Nesse 2012) or the mineral can have a biogenic origin (corals, molluscs). Aragonite is metastable with respect to calcite. Precipitation of aragonite under laboratory conditions can be achieved from various calcium salt solutions (chloride, sulphate, nitrate) reacting with slowly added carbonate solution (e.g. sodium or ammonium carbonate) above 60-70 °C (e.g. Hu and Deng 2003, 2004; Dandeu et al., 2006; Kaabar et al., 2011). However, synthetic aragonite may show different morphologies including rosettes (Tai and Chen, 1998). In order to precipitate aragonite shaped as needles, there have been studies aimed at both inorganic and organic additives (including magnesium-containing compounds) (Hu and Deng 2003; Park et al., 2008; Hu et al., 2009). The attention has been paid to the study of needle-like aragonite due to its potential advantages using as filler in rubber, plastics and papermaking (Hu and Deng 2004).

Other carbonate minerals often have the same crystal structure as calcite or aragonite and can be classified into notional classes by the size of the divalent cations involved. Divalent cations of intermediate size such as Mg, Mn and Fe form rhombohedral calcite structure (e.g. magnesite [$MgCO_3$], rhodosite [$MnCO_3$] and siderite [$FeCO_3$]) and large divalent cations such as Sr, Ba and Pb form orthorhombic aragonite structure (e.g. strontianite [$SrCO_3$], witherite [$BaCO_3$] and cerussite [$PbCO_3$]) (White 1974).

In contrast to calcite and aragonite, the third polymorph vaterite is the most unstable crystalline calcium carbonate with highest solubility. The mineral is rare in biological and geological settings. However it is relatively common under laboratory conditions (Lipmann 1973). Vaterite can be synthesised from calcium chloride solution with additives such as polyaspartic acid in the presence of $(NH_4)_2CO_3$, (Wehrmeister et al., 2010 after Loges et al., 2006) or e.g. by mixing solutions of calcium nitrate and sodium carbonate rapidly stirred with subsequent drying at 100 °C (Dandeu et al., 2006). Vaterite converts into more stable aragonite or calcite and therefore is sometimes viewed as their precursor in bio-mineralization (Hasse et al., 2000). Structurally, vaterite can be classified as an end member of a solid solution series of calcium carbonates containing rare-earth elements and fluoride (Yang et al., 2008). The vaterite crystal structure is hexagonal affected by stacking-faults and shifts of carbonate group layers. It is plausible that vaterite possesses at least three structurally different carbonate groups (Wehrmeister et al., 2010).

Hydrated calcium carbonate minerals

Amorphous calcium carbonate (ACC) has been described either as a highly unstable transient precursor to crystalline calcite and aragonite or a biogenic form. The biogenic form is stable and shows structural differences including the degree of hydration (Addadi et al., 2003; Raz et al., 2003). Synthetic ACC is described as both a hydrated and dehydrated metastable phase detected on a transition pathway from hydrated carbonates to anhydrous phases (Lam et al., 2007; Radha et al., 2010). Absence of water in synthetic [$CaCO_3$] was experimentally investigated by differential thermal analysis by Raz et al. (2003). However in a slightly older work the authors suggest that it is a microcrystalline monohydrate (Tlili et al., 2001).

Monohydrous calcite (MHC) [$CaCO_3.H_2O$] is a rare mineral requiring the presence of magnesium ions in its formation conditions although they are not incorporated in its structure (Nishiyama et al., 2013). The role of magnesium in the formation of aragonite and monohydrocalcite is probably similar (Lipmann 1973). Magnesium ions possess larger hydration energy than calcium and are strongly adsorbed on surface of calcite nuclei. Calcite growth is inhibited due to a layer of hydrated magnesium ions whose incorporation into a calcite lattice is dependent on foregoing dehydration (Loste et al.,

2003). Conversely magnesium ions do not create a significant obstacle in reaction kinetics of aragonite (Lipmann 1973). Moreover, paragenesis of hydrated magnesium carbonates seems to prolong existence of unstable hydrated calcium carbonate phases although the role of magnesium in their formation is not fully understood (Nishiyama et al., 2013).

Amorphous and monohydrous calcium carbonates have been investigated as key precursors in biomineralization (Addadi et al., 2003; Kimura and Koga 2011).

The hexahydrate calcium carbonate ikaite [$CaCO_3 \cdot 6H_2O$] is a monoclinic unstable hydrated calcium carbonate phase which is considered to be metastable dehydrating above 4 °C to vaterite or calcite (Omelon et al., 2001; Coleyshaw et al., 2003; Rysgaard et al., 2012). The mineral is rare in nature, occurring in Arctic and Antarctic sea ice (Rysgaard et al., 2012) but also precipitating during storage of frozen seafood (Carache et al., 2002). Due to its stability only at near-freezing temperatures, ancient ikaite is considered to be an indicator (of cold glaciomarine environments) used in climate change studies (Selleck et al., 2007).

1.2.2 Hydrated and basic magnesium carbonates

[$MgCO_3 \cdot XH_2O$] minerals

A number of hydrated magnesium carbonates have been identified in the system MgO-CO_2-H_2O (Figure 1.2). All are monoclinic, and separate into three groups. The first group of hydrated magnesium carbonates have as their basis magnesite with variable numbers of water molecules. Naturally occurring minerals include: lansfordite, nesquehonite and barringtonite (Figure 1.2). Lansfordite and nesquehonite are typically found in caves and coal mines, or associated with weathered surfaces of basic or ultramafic rocks, where temperatures are low and CO_2 pressures are often more than ten times atmospheric (Langmuir 1965). At CO_2 partial pressure of 1 atmosphere lansfordite transforms to nesquehonite at 10 ± 2 °C. Replacement is spontaneous and irreversible (Hill et al., 1982). Nesquehonite also occurs as evaporative films on magnesium-rich alkaline wetland

waters (Power et al., 2007) and in association with dypingite and hydromagnesite in lake shore-line and shallow water carbonate hardgrounds (Last et al., 2010). Pure nesquehonite can be prepared in the laboratory by various methods such as mixing solutions, e.g. magnesium nitrate solution with bicarbonate solution at 45 °C after one week (Hales et al., 2008). Other methods involve bubling CO_2 gas through solution of various magnesium salts, for example magnesium chloride at room temperature with subsequent pH adjustment by aqueous ammonia (Ferrini et al., 2009; Ballirano et al., 2010), or magnesium hydroxide solution with subsequent degassing (by sonicating) at slightly elevated temperatures (Hopkinson et al., 2012). Various combinations of these methods also exist, such as magnesium chloride and sodium carbonate in solution bubbling with CO_2 gas (Hänchen et al., 2008) or dissolving magnesium carbonate in CO_2 saturated water at room temperature with degassing at 35 °C (Lanqmuir 1965).

Barringtonite has been identified in association with nesquehonite in precipitates derived from groundwater circulating through weathered basalts (Nashar 1965). Moreover, the thermal behaviour of synthetic nesquehonite and its dissociation process at *ca.* 100 °C, results in water loss to yield an unidentified $MgCO_3 \cdot 2H_2O$ phase (Ballirano et al., 2010). Magnesium monohydrate carbonate has not been identified in nature, but has been synthesised by desiccating nesquehonite (Menzel and Brückner 1930). A range of [$MgCO_3 \cdot XH_20$] phases (X =<3) have also been synthesised by reaction between potassium carbonate solution and magnesium nitrate solution at varying temperatures and pH (adjusted by HNO_3 or KOH) (Zhang et al., 2006). The variation in the structural water content is attributed to varying conditions of synthesis. The [$MgCO_3 \cdot XH_20$] phases (X =<3) show mid-infrared bands matching the internal modes of the [CO_3^{2-}] anion in nesquehonite. However, no x-ray diffraction (XRD) data was reported in the above mentioned study. Complexity in this part of the system is further compounded by similarities between the thermal behaviour of nesquehonite and hydromagnesite (e.g., Beck 1950; Kazakov et al., 1959; Lanas and Alvarez 2004), and evidence for bicarbonate in some synthesised and natural samples of nesquehonite. These attributes have led some investigators to assign a basic magnesium carbonate formula to nesquehonite: [$Mg(OH, HCO_3) \cdot 2H_2O$] (e.g., Wells 1915; Beck 1950; Kazakov et al., 1959; Hales et al., 2008). Hence, either nesquehonite ranges in composition, or there is a structural isomer of the mineral (Hales et al., 2008).

[$Mg_5(CO_3)_4(OH)_2.XH_2O$] minerals

A second group consists of [$Mg_5(CO_3)_4(OH)_2$] with waters of crystallization ranging from four to eleven H_2O molecules. They are represented by: hydromagnesite (e.g., Königsberger et al., 1999); dypingite (Raade 1970; Canterford et al., 1984); giorgiosite (Raade 1970; Friedel 1975); an unnamed mineral [$Mg_5(CO_3)_4(OH)_2{\cdot}8H_2O$] (Suzuki and Ito 1973); and protohydromagnesite (Davies and Bubela 1973; Davies et al., 1977; Canterford et al., 1984). In the MgO-CO_2-H_2O system these [$Mg_5(CO_3)_4(OH)_2.X$H2O] mineral phases fall on a line which connects protohydromagnesite with hydromagnesite (Figure 1.2). The International Mineralogical Association – Commission on New Minerals and Mineral Names (IMA/CNMNC) status of giorgiosite is questionable. The status of nesquehonite is grandfathered: i.e. the original description preceded the establishment of the CNMNC in 1959, listed formula is [$MgCO_3{\cdot}3H_2O$]. The unnamed mineral [$Mg_5(CO_3)_4(OH)_2{\cdot}8H_2O$] is not listed.

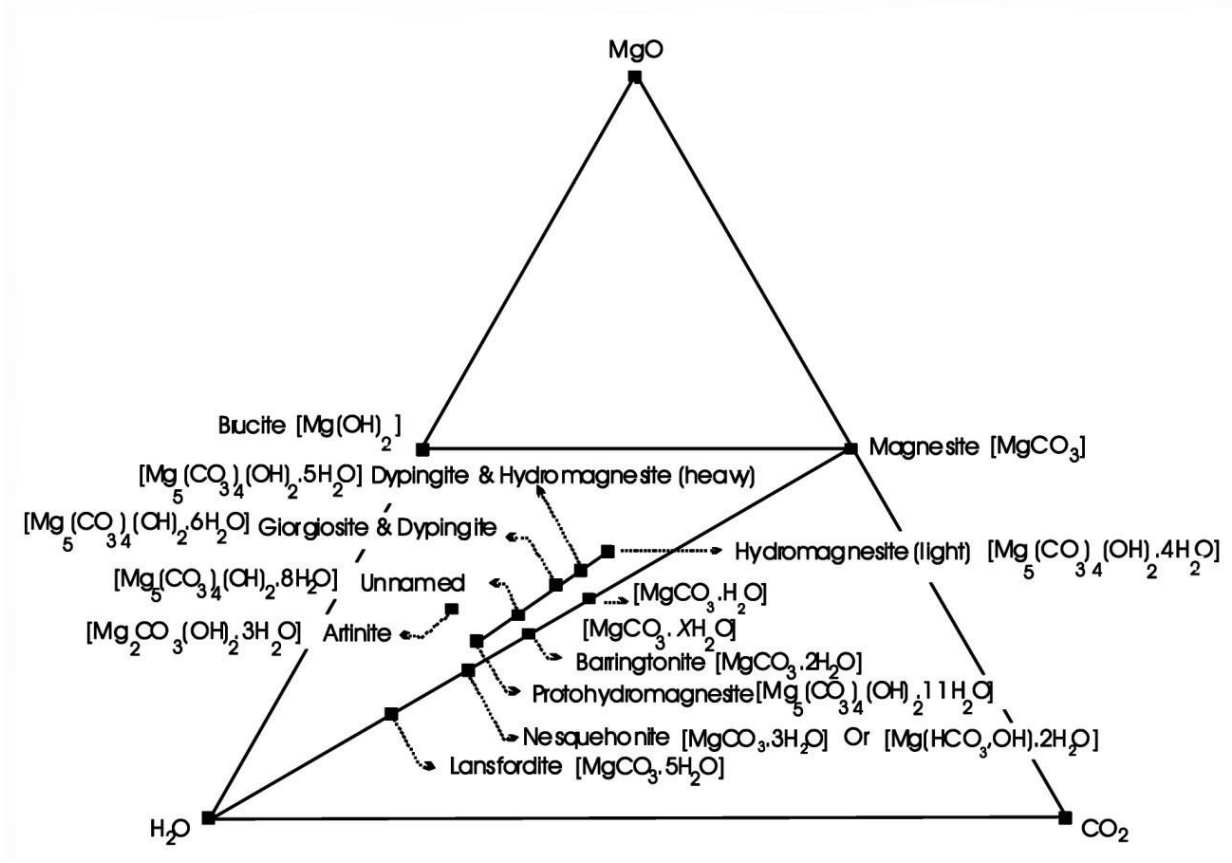

Figure 1.2: Ternary phase diagram for magnesium carbonates - The hydrated magnesium carbonate minerals in the system CO_2-MgO-H_2O (adapted from Canterford et al., 1984; Hopkinson et al., 2012). Specified values of *X* in synthesised $MgCO_3.XH_2O$ phases include 1.3 and 0.3 H_2O (Zhang et al., 2006).

Hydromagnesite [$Mg_5(CO_3)_4(OH)_2{\cdot}4H_2O$] is by far the most common naturally occurring mineral in the group. The mineral appears as a weathering product on mafic and ultramafic rocks, cave deposits derived from water that has seeped through magnesium-rich rocks, and as an abiogenic or biogenic mediated deposit in lakes, alkaline wetlands and evaporitic basins (e.g., Stamatakis 1995; Russell et al., 1999; Martinez-Arkarazo et al., 2007; Power et al., 2009; Last et al., 2010). Accounts of dypingite are far less widespread, although it has been described in similar settings, frequently in association with hydromagnesite (e.g., Power et al., 2007; Last et al., 2010). Dypingite also occurs as a precipitate derived from cold leaching solutions affecting serpentinite and magnesite spoil (Raade 1970). The chemical formula of dypingite may show 5 or 6 H_2O molecules (Xiong and Lord 2008).

Rarer still, giorgiosite and the unnamed mineral are described from their type localities in association with bodies of water situated on weathered volcanics (Suzuki and Ito 1973; Friedel 1975). Dypingite and protohydromagnesite have been synthesised individually during the [N→HM] transition in separate experimental studies (Davies and Bubela 1973; Hopkinson et al., 2008), although protohydromagnesite has not been identified in nature.

The vibrational spectra of the [$Mg_5(CO_3)_4(OH)_2.xH_2O$] phases are undocumented except for hydromagnesite and dypingite. The latter mineral shows infrared-active internal modes of the [CO_3^{2-}] anion indistinguishable from hydromagnesite (e.g., Raade 1970; Canterford et al., 1984). This necessitates that the two minerals share extensively similar or identical short range order, yet, disparate long range crystal order. More recent spectroscopic studies of dypingite show that variation in the intensity of water stretching bands occurs, indicating that differences in the chemical formula exist, and that [CO_3^{2-}] units are variably distorted (Frost et al., 2008a; Frost et al., 2009). Differential thermal analysis of dypingite at temperatures above 125 °C is essentially identical to hydromagnesite. However, dypingite also shows endothermic peaks at 55 and 125 °C, indicating that dypingite contains some loosely bound water which is lost at low temperatures (e.g., Raade 1970). Further heating of dypingite results in its conversion to hydromagnesite (Raade 1970; Botha and Strydom 2001). Laboratory synthesis of hydromagnesite and dypingite phases can be achieved by transformation of nesquehonite above 50 °C (Hänchen et al., 2008; Hopkinson et al., 2008, 2012). However, the reaction

pathways show diffusion and reaction-limited control with presence of metastable intermediates, and variations in the chemistry of nesquehonite implies that its transition to hydromagnesite is very complex and not fully understood (Hopkinson et al., 2008, 2012).

[$Mg_2(CO_3)$-$(OH)_2$].*X*H_2O minerals

The third group of hydrated magnesium carbonates [$Mg_2(CO_3)(OH)_2$].*X*H_2O is represented by the mineral artinite, reported with between two and four water molecules of crystallization (e.g., Beck 1950; Kazakov et al., 1959), and pokrovskite, with an empirical formula [$Mg_2(CO_3)(OH)_2$] (Perchiazzi and Merlino 2006). The generation of artinite during the solvent mediated decomposition of nesquehonite and subsequent transformation to hydromagnesite and then magnesite has been reported (Kazakov et al., 1959). Kazakov et al., (1959) observed an artinite type mineral precipitating in a 'low CO_2' experiment with MgO (determining pCO_2 partial pressure to be approximately one third of atmospheric pCO_2). The artinite phase was observed after 42-54 days of aging and was determined by thermal analysis. However, the study preceded identification of several [$Mg_5(CO_3)_4(OH)_2{\cdot}xH_2O$] phases. Moreover, Langmuir (1965) noted that artinite had not been described in natural settings in association with lansfordite or nesquehonite. In addition, recent experimental studies suggest that the [N → HM] transition proceeds with the apparent absence of artinite-type intermediate(s) (e.g., Davies and Bubela 1973; Davies et al., 1977; Zhang et al., 2006; Hopkinson et al., 2008). However all of the latter mentioned experiments were conducted at different conditions from Kazakov et al., (1959) which varied in time scale, presence of other salts such as chloride or nitrate, and CO_2 concentration.

[$MgCO_3$] Magnesite

Magnesite is the most stable magnesium carbonate under near surface ambient conditions (e.g. Königsberger et al., 1999; Hänchen et al., 2008). Investigations of magnesite deposits indicate two possible modes of formation: 1) formation at high temperatures and partial pressures of CO_2 with subsequent transportation to the surface, 2) through

transformation of hydromagnesite (Zachmann 1989). The first mode of formation cannot be applied to all magnesite deposits, e.g. lake sediments (Graf et al., 1961; Alderman 1965) although the second mode is recognised as the so called 'magnesite problem'. Magnesium carbonate's paragenesis is kinetically controlled, although magnesite precipitation is kinetically inhibited at normal near surface temperatures and pressures, possibly due to the high hydration energy of the Mg^{2+} ion (Hänchen et al., 2008). The high charge/radius ratio of Mg^{2+} leads to strong interaction with dipolar water molecules, thus inhibiting the dehydration process of hydrated magnesium carbonates (nesquehonite [$MgCO_3.3H_2O$] and hydromagnesite [$Mg_5(CO_3)_4(OH)_2.4H_2O$]) (Lipmann 1973).

1.2.3 Calcium magnesium carbonate minerals

Magnesian calcium carbonates

Magnesian calcium carbonates are a group of biogenic or inorganic minerals with Mg^{2+} ion substituted for some Ca^{2+}. Bischoff et al., (1985) investigated synthetic and biogenic magnesian calcites with up to 25 mol % concentration of $MgCO_3$. This process of introducing magnesium ions into the calcite structure is probably random where the end members of solid solutions are calcite and magnesite (Bischoff et al., 1985) (Figure 1.3). Similarly magnesian vaterite has been synthetized by Wehrmeister et al., (2009). It is plausible that these are possibly formed by contact of calcium carbonates with magnesium bearing solutions. Magnesian calcites demonstrate carbonate ion positional disorder which can be observed by Raman spectroscopy (Bischoff et al., 1985; Urmos et al., 1991). A greater amount of disorder was exhibited by biogenic magnesian calcites than by their synthetic analogues with the same amount of Mg^{2+} (Urmos et al., 1991). The amount of disorder plays a key role in determining relative chemical stabilities and further reaction pathways (Bischoff et al., 1993). The relative stability of Mg-Ca phases proposed by Bischoff (1993) increases with decreasing solubility from higher magnesian calcites (above 4 molar % of Mg^{2+}) to lower magnesian calcites (below 4 molar % of Mg^{2+}) and dolomite. Magnesian calcites can be laboratory prepared e.g. by reaction of sodium hydrogen carbonate solution with magnesium and calcium chloride solutions of varying Mg: Ca ratios (Loste et al., 2003).

Dolomite

Dolomite [$CaMg(CO_3)_2$] has ordering of magnesium and calcium ions in two different layers of its crystal structure (Scheetz and White 1977). Unlike huntite it is a mineral forming large platforms, e.g. the Dolomite Mountains in Northern Italy, also occurring in limestone and caves (e.g. McKenzie and Vasconcelos 2009; Alonso-Zarza et al., 2011; Martin-Perez et al., 2012). The origin(s) of dolomite are still uncertain although the so called 'dolomite problem' has been discussed in a vast amount of literature to date proposing several theories of its origin (e.g. Brady et al., 1996; Burns et al., 2000; McKenzie and Vasconcelos 2009; Sanchez-Roman et al., 2009). Laboratory synthesis of dolomite has been successful only at extreme conditions e.g. high temperatures, high supersaturations, precipitation in highly sulphate- and nitrate-rich solutions, or bacterial participation (e.g. Liebermann 1967; Brady et al., 1995; Deelman 1999). However, the abundance of dolomite and its occurrence together with other sedimentary minerals does not comply with these conditions. Dolomite precipitation was unsuccessful at low temperatures (Land 1998). One explanation of possible kinetic inhibition might be the high hydration of Mg^{2+} ions (de Leeuw and Parker 2001). Moreover, recently grown dolomite seems to be rare in the natural environments (Burns et al., 2000; Alonso-Zarza and Martin-Perez 2008), suggesting the presence of an inhibitor or absence of a catalyst in most low temperature settings. Furthermore mineral growth on dolomite surfaces is self-limited and although growth of a first layer of various concentrations of Mg/Ca ions could be observed at high saturation state by lateral force microscopy, the second layer was already highly inhibited (Higgins and Hu 2005). Dolomite growth with respect to surface complexation, rate-limiting steps of dehydration and carbonation of Mg ion are discussed by several authors (Lipmann 1973; Brady et al., 1996; de Leeuw and Parker 2001). A hypothesis currently taking the forefront is microbial dolomitization (Vasconselos et al., 1995; Vasconselos and McKenzie 1997; McKenzie and Vasconcelos 2009). The microbial precipitation of dolomite has been described to happen by several metabolic processes of various bacteria. These include bacterial sulphate reduction (Vasconselos et al., 1995; Warthmann et al., 2000), methanogenesis (Roberts et al., 2004) and aerobic respiration at the water-sediment interface (Sanchez-Roman et al., 2009). The latter mentioned mechanism is based on a metabolically mediated pH shift and

associated increase in alkality with precipitation of dolomite by bacteria in hypersaline environment (Sanchez-Roman et al., 2009).

Huntite

Huntite [$CaMg_3(CO_3)_4$], also reported as [$CaMg_4(CO_3)_4$] by Stanger (1986), has a superstructure of calcite with magnesium and calcium ions ordering within one layer (Scheetz and White 1977). The mineral is scarce in nature and possibly has uncommon formation conditions (Walling et al., 1995). The mineral precipitates either directly from aqueous solutions or results from secondary interaction of such solutions with pre-existing carbonates e.g. by ion replacement (Kinsman 1967; Dollase and Reeder 1986; Zachmann 1989; Calvo et al., 1995). Mechanisms of huntite formation are not fully understood although several characteristics of natural huntite samples could be in favour of a late stage primary precipitation. From elemental analysis of huntite with respect to its host rock it could be concluded that huntite has a lower chloride content, indicating freshwater rather than early marine conditions, and usually contains significant amounts of strontium (Shayan 1984) which is more typical for primary carbonates (Stanger 1986). Its occurrence is consistent with freshwater precipitation, particularly from descending low temperature solutions bearing magnesium and calcium ions (Cole and Lancucki 1975).

Synthetic huntite was reported during transformation of nesquehonite to hydromagnesite in the system CaO-MgO-H_2O-CO_2 by Hopkinson et al., (2008) where slurry containing magnesium hydroxide and calcium chloride was sparged with CO_2 gas and subsequently degassed by stepwise increasing temperature up to 60 °C and filtration. Formation of huntite has been also reported during a simulation of carbonate diagenetic processes in a tank system with organic rich sedimentary basin conditions (Davies et al., 1977). The layers in this experiment consisted of crushed dolomite, calcite, decaying algae, nesquehonite and brine. Huntite precipitated within the nesquehonite layer after a ten months period at varying temperatures (10-28 °C) (Davies et al., 1977). Huntite is in nature intriguingly sparse which suggests its formation conditions are uncommon (Walling et al., 1995) and/or subsequent diagenesis leads to equilibria of dolomite with magnesite and/or calcite (e.g. Lipmann 1973).

Hydrated calcium magnesium carbonate

Hydrous Ca-bearing magnesium carbonate (HCMC) with stochiometry ($Mg_{0.92}$,$Ca_{0.08}$)CO_3.$3H_2O$ has been reported by Queralt et al., (1997) in saline sediments in Spain with an approximate ratio of magnesium to calcium ions of 7:1.

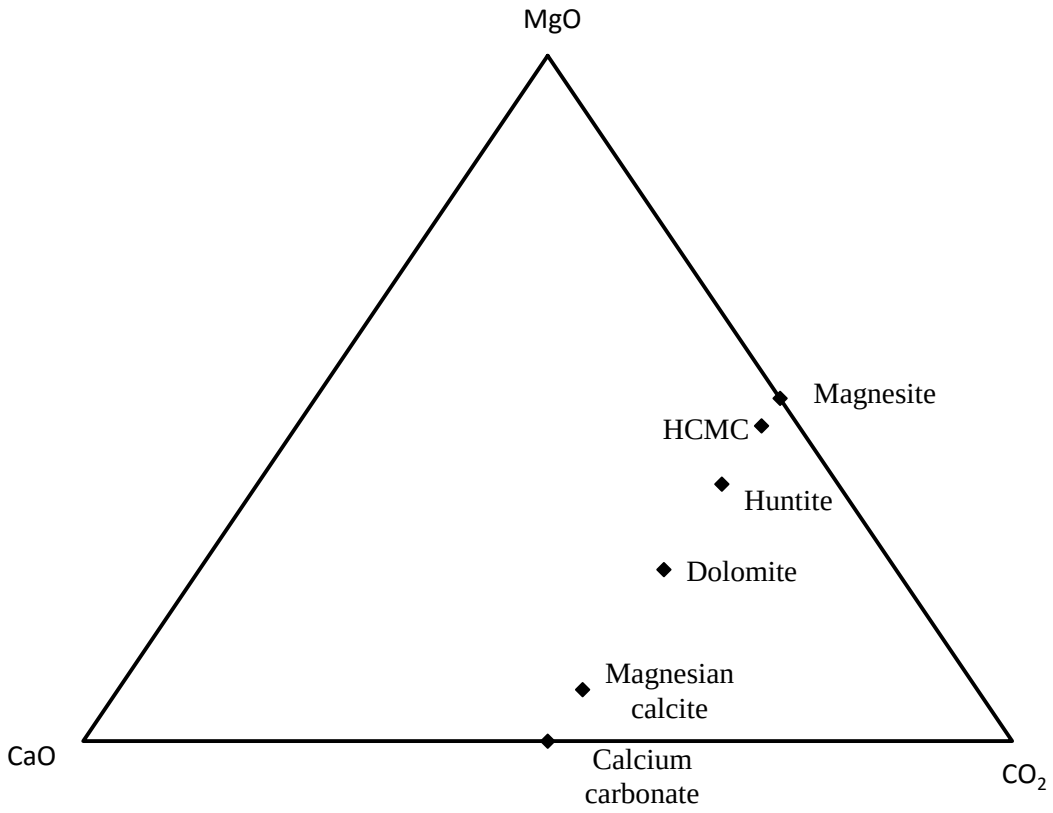

Figure 1.3: Ternary phase diagram of calcium magnesium carbonates. HCMC – hydrous calcium bearing magnesium carbonate.

Calcium and magnesium minerals discussed in this section and their formulas are summarized in Table 1.1.

Hydrated and basic calcium carbonates	
calcite	$CaCO_3$
aragonite	$CaCO_3$
vaterite	$CaCO_3$
amorphous calcium carbonate (ACC)	$CaCO_3$

monohydrous calcite (MHC)	$CaCO_3 \cdot H_2O$
ikaite	$CaCO_3 \cdot 6H_2O$
Hydrated and basic magnesium carbonates	
lansfordite	$MgCO_3 \cdot 5H_2O$
nesquehonite	$MgCO_3 \cdot 3H_2O$ or $Mg(HCO_3,OH) \cdot 2H_2O$
barringtonite	$MgCO_3 \cdot 2H_2O$
hydromagnesite	$Mg_5(CO_3)_4(OH)_2 \cdot 4H_2O$ or $Mg_5(CO_3)_4(OH)_2 \cdot 5H_2O$ (heavy)
dypingite	$Mg_5(CO_3)_4(OH)_2 \cdot 5H_2O$ or $Mg_5(CO_3)_4(OH)_2 \cdot 6H_2O$
giorgiosite	$Mg_5(CO_3)_4(OH)_2 \cdot 6H_2O$
unnamed mineral	$Mg_5(CO_3)_4(OH)_2 \cdot 8H_2O$
protohydromagnesite	$Mg_5(CO_3)_4(OH)_2 \cdot 11H_2O$
artinite	$Mg_2(CO_3)(OH)_2 \cdot XH_2O$ (X ranges between 2 to 4)
pokrovskite	$Mg_2(CO_3)(OH)_2 \cdot 0.5H_2O$
magnesite	$MgCO_3$
Calcium magnesium carbonates	
magnesian calcium carbonates	
dolomite	$CaMg(CO_3)_2$
huntite	$CaMg_3(CO_3)_4$ or $CaMg_4(CO_3)_4$
hydrous Ca-bearing magnesium carbonate (HCMC)	$(Mg_{0.92},Ca_{0.08})CO_3.3H_2O$

Table 1.1: Summary of magnesium and calcium carbonate minerals and their chemical formulas

1.2.4 Analytical characterisation of carbonate minerals

In recent sediments carbonate minerals in the system $CaO\text{-}MgO\text{-}H_2O\text{-}CO_2$ are frequently intimately intermixed. It is established that the huntite and hydromagnesite components in sediments and rocks are subject to progressive replacement, by the equilibrium assemblages magnesite-dolomite and dolomite-calcite during diagenesis (e.g., Kinsman

1967; Lippmann 1973; Stamatakis 1995). Mineral identification and mineral assemblage characterisation are commonly conducted by x-ray diffraction (XRD). The technique is still almost invariably laboratory based and frequently remote from field exposures and sites of mineral processing. Further, quantitative determination of assemblages by XRD can be problematic (e.g., Vagenas and Kontoyannis 2003), due to difficulties in obtaining appropriate reference materials. Moreover, the degree of long range crystal order of Mg-Ca carbonates is variable (e.g., Hopkinson et al. 2008, 2012). Mid-infrared spectroscopy (mid-IR) has proved useful for the qualitative identification and quantitative analysis of carbonates in rocks and other minerals (White 1974). However, mid-IR is used significantly less compared to XRD. The sample particle size requirements are *ca.* 2 μm or less (Vagenas and Kontoyannis 2003). The IR spectral bands are relatively broad, often with indefinite baseline. In addition, significant overlap occurs in the spectra of the Mg-Ca carbonates. These reasons make applications of XRD or IR techniques in many cases inconvenient and hence there is a need for an alternative method. Raman spectroscopy, although considered as a classic technique in academia, seems to be rarely used in mineral processing. Raman and infrared spectra of calcium and magnesium carbonates have also been included in many studies and spectroscopic compilations of inorganic materials (e.g. White 1974; Scheetz 1977; Edwards et al., 2005; Frost 2011). With progress of modern technology, mainly in the area of laser equipment and its miniaturization, large spectroscopic instruments have become portable, allowing what were originally laboratory procedures to be field-based (Smith and Dent 2008). This enables many applications of spectroscopic analysis to be carried out *in situ* (e.g., Jehlicka et al., 2009) for new users, and the development of new turn-key methods for possibly non-scientific operators. All of the above make Raman spectroscopy, known for its rapid results and universality in material identification, a potentially attractive alternative to traditional analytical techniques, although research in the field of Raman quantitative measurements is needed.

1.3 Vibrational spectroscopy

Raman and infrared spectroscopies are rapid analytical techniques used to detect vibrations in molecules. Both of the techniques are based on interaction with light i.e. inelastic scattering and absorption for RS and IR respectively (Figure 1.5). The measured samples on interaction with light provide information in the form of specific spectral patterns, consisting of peak positions and their intensity ratios, which can be used for material identification and semi-quantitative determination.

The individual spectral peaks arise from various molecular vibrations (e.g. symmetric or antisymmetric stretch, in plane and out of plane bend, etc.) The number of vibrations is associated with degrees of freedom of a molecule. A molecule of N atoms has 3N degrees of freedom as its three-dimensional description, where its energy is translational, rotational and vibrational. The number of molecular fundamental vibrations is equal to 3N - 6 (or 3N - 5 for linear molecules) degrees of freedom, where three degrees are subtracted as a translation of a molecule, and three represent rotation of a molecule (only two for linear molecules) (e.g. Burns 1977; Smith and Dent 2008).

For crystals it is not just atoms forming a molecule but all atoms in a unit cell of crystal lattice that are considered. The neighbouring unit cells can also vibrate in phase and antiphase. Then if n equals the number of atoms in a primitive unit cell the number of normal modes is 3n-3 where the three modes subtracted are for all cell units moving in phase (Burns 1977).

Raman and infrared spectroscopies are two complementary techniques having different selection rules. This in a simplified way means that some molecular vibrations are only Raman or infrared active, some vibrations appear in both spectroscopies, generally weak peaks on infrared spectra give strong signals in Raman spectra and *vice versa*. Group theory is used to predict Raman (R) or infrared (IR) active vibrations.

1.3.1 Group theory

The molecules are classified into point groups by their symmetry elements like mirror planes, axes of rotation, centers of inversion, etc. The spectra of solids are different from liquids. The main differences are caused by intermolecular forces in solids which are responsible for lowering the symmetry. For crystals one also needs to take into account the space group of crystallographic symmetry and the site groups. These result in splitting or broadening of degenerate vibrations and the appearance of otherwise silent modes in IR and Raman. The symmetry properties of each point group are expressed as a character table. The details of symmetry elements and operations can be found in many mathematical and chemistry textbooks (e.g. Jaffe and Orchin 1965; Burns 1977; Tsukerblat 2006). The symmetry operations describing a stationary molecule are listed in Table 1.2.

Symmetry operation	Symbols	Description
The identity	E or I	pseudo-operation, defines original state and has got mainly mathematical importance
Rotations	C_n	a rotation of $2\pi/n$ radians about an axis, where n is an integer. The axis with the highest value of n is the principal axis (z)
Reflections (mirror planes)	σ_v, σ_h, σ_d	vertical planes (σ_v) contain the principal z-axis i.e. xz plane and yz plane, similarly horizontal planes (σ_h) and dihedral or diagonal planes (σ_d)
Rotation-Inversion axes	S_n	a rotation in conjunction with reflection or inversion also called improper rotation.
A centre of inversion (or reflection)	i	atom is reflected in the same atom through a centre, in Cartesian system (x,y,z) becomes (-x,-y,-z).

Table 1.2: Symmetry operations and their symbols. Adapted after Jaffe and Orchin (1965), Burns (1977).

A point group is a combination of symmetry elements where the product of any two elements of the set is another element of the set. Motions of a molecule are best described

as vectorial properties of matter i.e. having magnitude as well as direction (e.g. Jaffe and Orchin 1965). It is the motion under a symmetry operation with respect to Cartesian coordinates (x,y,z, see Figure 1.4) which is considered and transcribed as +1 or -1 should it be symmetrical or anti-symmetrical motion respectively. These are known as reducible representations. There are different symmetry types (symmetry species) conventionally labeled A and B. Vibration modes symmetric with respect to the principal axis are A and antisymmetric B. If the molecule possesses a centre of symmetry then subscripts g and u meaning even, phase (gerade) and odd, anti-phase (ungerade), respectively are assigned. (These are explaining whether the given motion is symmetric (g) or antisymmetric (u) with respect to centre of symmetry). Similarly motions of electrons can be described using lower case (a, b). If there are two or more vectors (or tensors) of equivalent quantity then the vibration mode is degenerate, i.e. doubly (E) and triply degenerate representation (T).

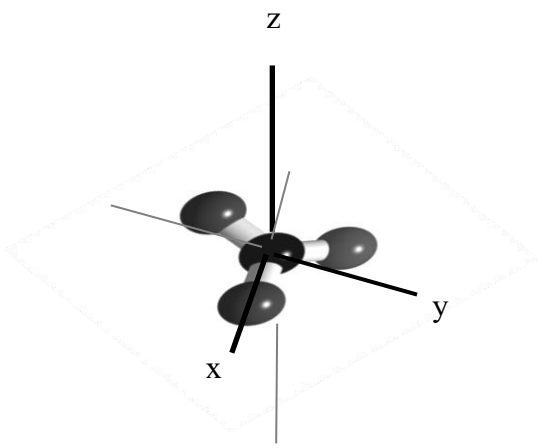

Figure 1.4: Cartesian coordinates and carbonate ion.

The reducible representations are the combinations of symmetry operations coming from symmetry elements. Transformation of coordinates can be represented by a matrix (a reducible representation) which can be simplified to a combination of irreducible representations.

The carbonate anion [CO_3^{2-}] forms a planar triangle with molecular symmetry D_3h. In isolation its vibrational spectrum consists of four normal (internal) modes - ν_1 symmetric stretch (Raman active), ν_2 out-of-plane bend (IR active), ν_3 asymmetric stretch and ν_4 in-plane bend, which are both Raman and IR active. In carbonate minerals the [CO_3^{2-}] anion

is bonded to cations within the crystal lattice and operates under symmetrical constraints, distinctive to the specific mineral species (White 1974). The vibrational spectra and band assignments of the Mg-Ca carbonates are well documented (e.g. Edwards et al., 2005; Frost and Dickfos 2007a).

The site symmetry of the CO_3^{2-} group is determined by cation environment and modulates the selection rules as well as spectral positions (Kaabar et al., 2011). Therefore e.g. calcite [$CaCO_3$] restricted by symmetrical constraints belongs to site group D_3 with space group D_3d. The structure of calcite is formed by Ca and CO_3 in a face centred rhombohedron. The unit cell of calcite contains two reversely oriented carbonate groups, one situated above the central calcium ion and one below it (Figure 1.1). There are ten atoms in the unit cell - two calcium atoms (central atom and eight Ca atoms contributing only by 1/8), two carbon atoms and six oxygen atoms (Lou et al., 2007). Therefore the unit cell contains two formula units of calcium carbonate [$CaCO_3$]. These two carbonate ions give two similar sets of internal vibrations and are under symmetry constraints in phase or anti-phase to each other with respect to centre of symmetry (White 1974). The reducible representations of calcite are expressed in Table 1.3, representations for the carbonate ion are showed in Table 1.4.

D_3d	E	$2C_3$	$3C_2$	I	$2S_6$	$3\sigma_d$	linear, rotations
U(R)	10	4	4	2	2	0	
ω(R)	3	0	-1	-3	0	1	
χ(R)	30	0	-4	-6	0	0	
A_{1g}	1	1	1	1	1	1	
A_{2g}	1	1	-1	1	1	-1	R_z
E_g	2	-1	0	2	-1	0	R_x,R_y
A_{1u}	1	1	1	-1	-1	-1	
A_{2u}	1	1	-1	-1	-1	1	T_z
E_u	2	-1	0	-2	1	0	T_x,T_y

Table 1.3: Calcite (D3d) symmetries (e.g. Burns 1977; Lou et al. 2007), reducible representations and character table. U(R) is number of unshifted atoms under symmetry operation (R), ω(R) denotes contribution per atom, χ(R) are reducible representations where χ(R)= U(R) x ω(R).

D_3h	E	$2C_3$	$3C_2$	σ_h	$2S_3$	$3\sigma_v$	linear, rotations
U(R)	4	1	2	4	1	2	
ω(R)	3	0	-1	1	-2	1	
χ(R)	12	0	-2	4	-2	2	
A'_1	1	1	1	1	1	1	
A'_2	1	1	-1	1	1	-1	Rz
E’	2	-1	0	2	-1	0	T_x,T_y
A''_1	1	1	1	-1	-1	-1	
A''_2	1	1	-1	-1	-1	1	z
E’’	2	-1	0	-2	1	0	(x,y)

Table 1.4: Carbonate ion (D3h) symmetries (e.g. Burns 1977; Lou et al., 2007), reducible representations and character table. U(R) is number of unshifted atoms under symmetry operation (R), ω(R) denotes contribution per atom, χ(R) are reducible representations where χ(R)= U(R) x ω(R).

A number of modes (n_m) can be calculated by following the equation of factor group symmetry analysis:

$$n_m = \frac{1}{h} \sum_R g(R)\chi(R)\chi_m(R) \qquad \text{(Equation 1.1) (Lou et al. 2007)}$$

h is order of the group

$g(R)$ number of operations in the class

$\chi(R)$ reducible representations

$\chi_m(R)$ irreducible representations

A mode distribution for calcite structure is shown in Table 1.5.

D3d	Total	Trans	Rot	Internal	Selection rules
A_{1g}	1	0	0	1 (ν_1)	Raman active
A_{2g}	3	1	1	1 (ν_2)	Inactive
E_g	4	1	1	2 (ν_3, ν_4)	Raman active
A_{1u}	2	1	0	1 (ν_1)	Inactive
A_{2u}	4	1	1	1 (ν_2)	IR active
E_u	6	2	1	2 (ν_3, ν_4)	IR active

Table 1.5: Mode distribution and selection rules for calcite structures adapted after White (1974) and Lou et al. (2007).

1.3.2 Raman spectroscopy

Raman spectroscopy (RS) is a well-established non-destructive analytical technique that offers rapid identification of materials and their polymorphs with many applications (e.g., Daudeu et al., 2006, Kiefer 2007). Raman (inelastic) scattering can be measured for molecules exhibiting polarizability changes in vibrational modes. Light waves propagate an oscillating dipole which can interact with a molecular structure and distort the cloud of electrons around the nuclei. The electrons are polarized and move to their higher energy state, the molecule is excited to a virtual state. This energetic state is very unstable and the light energy is released as scattered radiation (Smith and Dent, 2008).

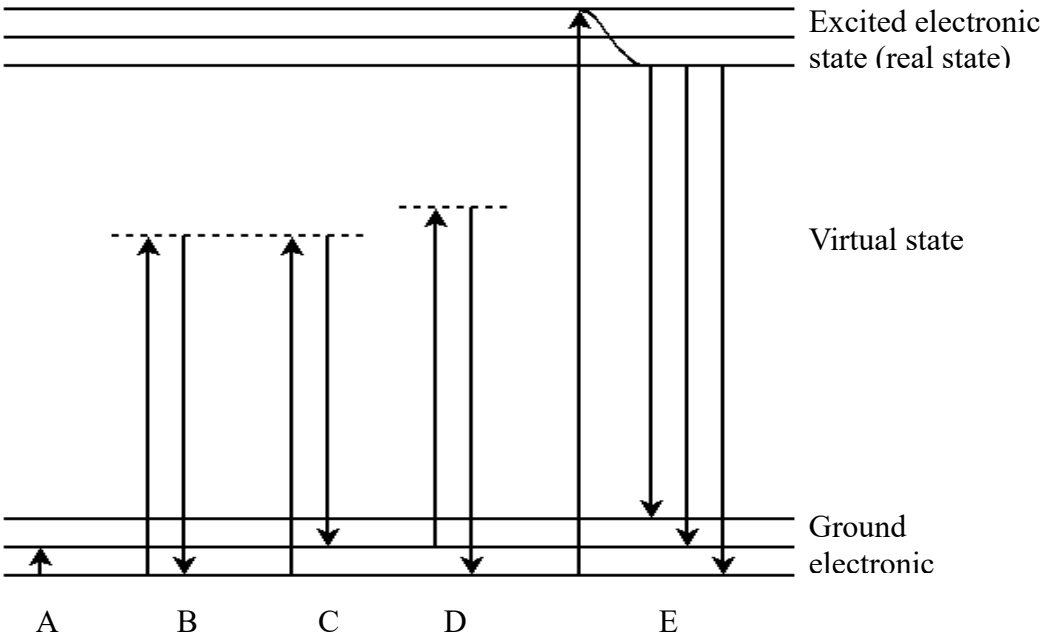

Figure 1.5: Schematic representations of light absorption and scattering in comparison to fluorescence. A) Infrared absorption, B) Rayleigh scattering, C) Stokes Raman scattering, D) anti-Stokes Raman scattering, E) fluorescence.

The electron cloud is distorted in all directions therefore molecular polarizability is also described as a tensor on all three Cartesian axes. Hence the symmetry concepts play an important role and this spectroscopy gives complex information about bands and backbone structure. The pattern of shifted wavenumbers is used for identification including distinguishing of polymorphs which cannot always be performed by infrared spectroscopy. The change in molecular polarizability appearing as peak intensity has a potential for quantitative work. Raman intensity is formed by a complex expression although for analytical work can be expressed as an analogue to the Lambert-Beer Law (Equation 1.2 and 1.3) (Chen et al., 2012).

Lambert-Beer law:

$$A = log_{10} I_o / I = \varepsilon \, l \, c \qquad \text{(Equation 1.2)}$$

A absorbance

I_o the intensity of light passing through reference

I the intensity of light passing through sample

ε constant, the molar absorptivity

c represents concentration (in moles per litre),

l refers to the path length given in centimetres

$$I(v) = n \cdot r(v) \cdot I_o \qquad \text{(Equation 1.3)}$$

I(v) represents the Raman intensity at Raman shift *(v)*

I_o represents intensity of excitation light

n refers to number of sample molecules, i.e. sample concentration

r(v) covers a number of factors such as spectrometer response, self-absorption, molecular scattering properties of a measured sample (Chen et al., 2012)

Although frequency shifts are in the infrared region, the excitation and emission wavelengths are in the visible or near-infrared. This eliminates one serious disadvantage of infrared spectroscopy which is the absorption of the radiation by containers such as glass. Interference from water is significantly lower than in infrared spectroscopy enabling solution/suspension studies to be made.

1.3.3 Near-Infrared spectroscopy

Infrared spectroscopy (IR) can be split into three spectral ranges i.e. near-infrared (15000-4000 cm^{-1}), mid-infrared (4000-400 cm^{-1}) and far-infrared range (400–10 cm^{-1}). The mid-infrared range is the most commonly used range, mainly for identification of substances, although near-IR spectroscopy has gained increased interest, especially in process control applications. Infrared spectrometry relies on absorption of energy of the infrared beam. Near-infrared spectroscopy (NIR) covers a spectral range defined between 15000-4000 cm^{-1} (666-2500 nm). It is characterised by broad peaks with curved baseline. This method appears to have great potential in quantitative work and although it has been used in pharmaceutical applications, its utilization to quantify geological samples is infrequent. Thanks to relatively weak optical absorption this technique allows analysis of larger samples with little or no sample preparation. NIR is sometimes called proton spectroscopy and compounds containing protons can be characterized by overtones and combination of fundamental bands occurring in the mid-infrared region (4000-400 cm^{-1}). Overtones appear at approximately multiples of fundamental wavenumbers and are 10-100 times weaker than the fundamental bands (Blanco and Villarroya 2002). The near-

infrared band intensity depends on the change in dipole moment and the anharmonicity of the bond (Blanco and Villarroya 2002). This spectroscopic technique was found to be highly applicable to hydroxyl- and hydrated carbonates (Frost 2008). Similarly to RS, near-infrared spectrometers have recently been developed into portable instruments.

1.3.4 Limitations of Raman and near-infrared spectroscopic analyses

Both vibrational spectroscopies (NIR and RS) have technique-specific limitations. The most significant limitation of Raman spectroscopy is fluorescence. In case of near-infrared spectroscopy it is water/moisture sensitivity. For carbonate minerals it means that in the region at *ca.* 5200 cm^{-1} absorptions may be masked by overtones caused by H_2O. Both techniques, RS and NIR, give limited information about structure. Raman spectroscopy also operates with a small sample size which might not be representative e.g. for coarse grained mixtures (Bugay 2001). Both vibrational spectroscopies lack detailed elemental analytical data although some information can be obtained e.g. on cation substitution within mineral lattice (Frost et al. 2009, Gaffey 1986).

The phenomenon of fluorescence in Raman spectra has been investigated in several studies (e.g Bell et al., 1998; Matousek et al., 2002) because it can potentially mask a Raman spectrum (Mossier-Boss et al., 1995). During fluorescence, the molecule absorbs radiation (incident photon) and is brought to a real state having a variable lifetime (Figure 1.5). Subsequently a photon with a different frequency is re-emitted and the molecule relaxes back to the ground energetic state. Fluorescence is dependent on incident light wavelength and often can be avoided by selection of different irradiation source e.g. near-infrared laser compared to ultra-violet (Schrader et al., 1991), in comparison Raman scattering is a constant shift from incident light of any frequency. Based on the above there are several different strategies to suppress fluorescence for particular samples although none of them is universally successful (Bell et al., 1998). These options include background correction, operation at specific laser wavelength, analysis in the anti-Stokes part of spectra, shifted excitation Raman difference spectroscopy (Mosier-Boss et al., 1995; Schrader et al., 1991). Based on the fact that Raman inelastic scattering is faster (picoseconds) than the response from fluorescence (nanoseconds) led to development of gated detectors for super short signal collection (Matousek et al., 2002). However

portable Raman devices are overwhelmingly ungated (dispersive), in these cases fluorescent background can be reduced by photo-bleaching prior to Raman measurement. Photo-bleaching involves exposing the sample to Raman laser irradiation inducing photolytic decomposition which can in some cases successfully degrade fluorescent molecules and reduce fluorescence background (Dennis 2007). This can be particularly useful if the fluorescence originates from an impurity.

1.4 Aims of this investigation

The first aim of this work is to provide an analytical means to employ portable Raman and NIR spectroscopies in a capacity for fully quantitative analysis of carbonate mineral mixtures. With respect to the first aim, the relationship between intensity ratio of Raman peaks and weight fraction of carbonate mixtures will be a critical parameter. Calibration curves are constructed by using mixtures of reference material and calibrated against x-ray diffraction. Similar experiments were then performed using near-infrared spectroscopy and compared. NIR appears to have great potential in quantitative work and although it has been used in a few pharmaceutical applications, there is limited evidence of its application on admixtures of Mg-Ca carbonates. The usage of chemometric treatment of Raman and NIR spectra and spectral manipulation such as peak deconvolution will also be investigated.

Previous work has shown that synthesis of certain carbonate minerals is feasible e.g. hydromagnesite can be synthesized in the laboratory by sequestration of carbon dioxide and the general procedure has been established (Botha and Strydom 2001; Hopkinson et al., 2008; Hänchen et al., 2008; Hopkinson et al., 2012). However the chemical steps in the process appear to be very complex, and strongly kinetically controlled. To this end the second aim of this thesis is to apply the spectroscopic findings to advanced understanding of the real time kinetics of reaction pathways in low temperature experimental settings in the system $CaO\text{-}MgO\text{-}CO_2\text{-}H_2O$.

2 Quantification of natural carbonates

2.1 Carbonate minerals in near-infrared and Raman spectroscopy and their quantification

The carbonate minerals dolomite [$MgCa(CO_3)_2$], magnesite [$MgCO_3$] hydromagnesite [$Mg_5(CO_3)_4(OH)_2.4H_2O$] and huntite [$CaMg_3(CO_3)_4$] frequently occur intimately intermixed in recent sediments. Collectively, the four Mg-Ca carbonate minerals are commercially important, with applications in finely powdered forms, in many branches of industry, e.g. pharmaceutical, cosmetic, paint formulations, flame retardants and bulk applications. Commonly, the purity of the powders with respect to the modal abundance of the different carbonate mineral phases is of prime concern. For instance hydromagnesite and huntite are often used in conjunction in customized mixtures (Hollingberry and Hull 2010; 2012). Hence, a method that facilitates rapid and accurate characterization of carbonate mineral assemblages is important.

Mineral identification and mineral assemblage characterization are commonly conducted by X-ray diffraction (XRD) although this can be problematic (Vagenas and Kontoyannis 2003). Less used and also debatable seems to be IR in its mid-infrared range. This is discussed in the introduction. The need for an enhanced and quick characterization technique is obvious. Two spectroscopic techniques, Raman and near-infrared, were investigated to assess whether they could be used for quantification and further research of carbonate minerals. Current development of portable spectrometers, ranging in size from handheld to larger transportable equipment, could also bring new possible industrial or geological applications. The Raman measurements under field conditions have been tested by e.g. Jehlicka et al., (2011), Vitek et al., (2012) and also a few pioneer studies investigated their reliability for a possible quantitative detection with applications aimed at planetary exploration (Culka et al., 2011; Vandenabeele et al., 2012). An extensive review of mobile Raman spectrometers and their applications can be found in Vandenabeele et al., (2014). Near-infrared spectroscopy, although blossoming in quantification in other industries, is noticeably absent in applications to carbonate mineral samples and assemblages. The purpose of this work is to explore the spectroscopic signature of powdered mixed assemblages of finely ground hydromagnesite, huntite,

dolomite and magnesite based on the intensity of Raman and near-infrared peaks of known weight fractions admixtures of the four mineral phases. The effects of sample packing and size are also discussed to evaluate additional effects on spectra.

2.1.1 Near-infrared spectroscopy

Near-infrared spectroscopy (NIR) is a rapid non-destructive analytical technique with fast growing usage mainly in quality control areas, raw materials analysis, medical applications and quantification. The reflectance spectroscopy quantitative applications to carbonate mineral assemblages are relatively unexplored although the mid-infrared spectroscopic range has been described in great detail (e.g. White 1974). So far there have been only a few studies linking chemical as well as mineralogical properties to near infrared spectra (e.g. Frost et al., 2008a; Gaffey 1986) although NIR can in some cases recognise difficult to resolve minerals (Gaffey 1986). Nevertheless, thanks to the larger illumination area NIR analyses comparatively larger areas of a given specimen than mid-infrared spectroscopy and therefore allows for more representative sampling of bulk materials. However, the technique is based mainly on overtones of hydrogen bond stretching modes and therefore is highly sensitive to moisture (Bugay 2001).

NIR is often used as a semi-quantitative method although absolute values are particle size and compaction dependent and therefore are generally expressed as relative spectral ratios (Gaffey 1986). Spectral information obtained from NIR is characterised by broad bands that often overlap which are inconvenient for monovariable quantifications, hence multivariable models such as Partial Least Squares (PLS) or Principal Component Regression (PCR+) are used (Berntsson et al., 2000; Choquette et al., 2002; Rinnan et al., 2009). Second derivatives are also often calculated to resolve overlapping bands. The quantifications obtained are in general linear or close to linear although non-linear calibrations are also described (e.g. Blanco et al., 1999; Rinnan et al., 2009). The NIR spectral range 15000-4000 cm^{-1} (666-2500 nm) consists of overtone and combination bands occurring in the mid-infrared region. The baseline of a NIR spectrum is naturally curved rising at lower wavenumbers with wavelength dependent peak intensity (Gunasekaran et al., 2006).

Assignment of near-infrared spectra of carbonate minerals is problematic mainly due to variations in natural mineral samples containing inclusions and different approaches of authors to data manipulation, deconvolution and peak fitting of the broad spectral bands (Gaffey 1986). The spectral information can be divided into three main areas. In the region above 7500 cm^{-1} there are electronic bands and weak bands of the second overtone of the OH stretch. The second main area, between 7200 and 6300 cm^{-1}, shows first overtone bands of OH stretch. In the third region, below 6300 cm^{-1} combination bands for carbonate ion, hydroxyl group and water occur (Reddy et al., 2008). Seven main bands between 1.6 μm (6250 cm^{-1}) to 2.55 μm (3922 cm^{-1}) due to absorption of carbonate ion have been described (Gaffey 1985, 1986). Calcite band positions analysed using a Gaussian function were described as 2.532 μm, 2.337 μm, 2.265 μm, 2.171 μm, 1.995 μm, 1.882 μm and 1.756 μm (corresponding to *ca.* 3949 cm^{-1}, 4278 cm^{-1}, 4415 cm^{-1}, 4606 cm^{-1}, 5012 cm^{-1}, 5313 and 5694 cm^{-1}), where differences in peak positions for other carbonate minerals are related to differences in their fundamental modes (Gaffey 1986).

The presence of at least some water in natural samples of nominally anhydrous carbonate minerals is potentially possible as water may still be present as aqueous fluid inclusions (Gaffey 1985) or possibly adsorbed moisture. The water molecule has three fundamental bands in the mid-infrared region i.e. symmetric OH stretch (ν_1), bending mode (ν_2) and asymmetric OH stretch (ν_3). These bands give rise to five prominent peaks at NIR spectra described by Curcio and Petty (1951), these are 0.76 μm, 0.97 μm, 1.19 μm, 1.45 μm, and 1.94 μm (corresponding to *ca.* 13158 cm^{-1}, 10309 cm^{-1}, 8403 cm^{-1}, 6896 cm^{-1} and 5155 cm^{-1}). The presence of water or OH group(s) within a mineral will also have a strong effect on an NIR spectrum. The hydrated carbonate spectral information will show stretching and bending modes at wavenumbers similar to the water peaks described above. Electronic bands are often observed in crystals with distorted structure and are generally assigned to metal cation (Mn^{2+}, Fe^{2+}) replacement (Gaffey 1985; Gaffey 1986; Frost et al., 2009).

2.1.2 Raman spectroscopy

Raman spectroscopy is often used as a semi-quantitative method, using line ratios or standard addition, thereby producing generally simple calibrations based on single peak height or area measurements (Vagenas et al., 2003; Noguchi et al., 2009). Amongst the quantitative investigations of carbonate mineral phases by Raman, binary mixtures of calcite in dolomitic marble have been investigated by standard addition (Vagenas and Kontoyannis 2003) and by monovariable calibration by peak height against weight fraction. The same techniques have been applied to calcium carbonate fillers in high-density polyethylene (Pakjamsai and Suwanprateeb 2000) and silicate and calcium carbonate assemblages using Raman micro-spectrometry (Noguchi et al., 2009). However, less attention has been paid to quantitative analysis of ternary or multi-component admixtures of carbonate mineral assemblages although multivariable methods, utilizing all Raman active bands i.e. Partial Least Squares (PLS), have been successfully employed to quantify the modal abundances of calcite, aragonite and vaterite in powdered mixtures of the three $CaCO_3$ polymorphs (Dandeu et al., 2006; Jehlicka et al., 2009). A close link between Raman band positions and chemical composition of rhombohedral carbonates forming solid solutions in Ca-Mg-Fe system was demonstrated by Rividi et al., (2010). Moreover, mixtures of calcium, strontium and barium carbonates have been investigated by Raman spectroscopy, employing the full width at half maximum (FWHM) intensity of the v_1 modes of the carbonate anion for the three mineral phases (Kaabar et al., 2011). The study by Kaabar et al. (2011) showed that the calcium carbonate precipitated in mixtures with barium and strontium cations dominated the Raman spectral frequencies even at relatively low concentration of *ca*. 17 %. This was assigned to discrepancy in size between Ca^{2+} ion and Sr^{2+} and Ba^{2+} where strontium and barium have significantly larger cations. The RS measurements by FWHM show that carbonates containing two or more unequal cations can show varying peak width in comparison to single cation carbonate or carbonates containing cations with similar radius. At present a standard methodology for quantitative calibration of multi-minerallic carbonate assemblages is absent (Fevotte 2007) and accounts of quaternary calibration procedures for carbonate assemblages are lacking.

The Raman spectra of calcium and magnesium carbonates are divisible into three wavenumber regions: 1500–1000 cm^{-1}, 1000–500 cm^{-1}, and 500–100 cm^{-1} (Scheetz 1977;

Edwards et al., 2005; Frost and Dickfos 2007a, 2007b; Frost 2011). In general, bands at frequencies above 500 cm^{-1} are due to the internal motions of the molecular carbonate anion (internal modes). Those below 500 cm^{-1} are due to motions involving the entire lattice cell (lattice modes). Within the 1500–1000 cm^{-1} region, the symmetrical stretching mode v_1 of the [CO_3^{2-}] anion is the strongest band observed in the Raman spectrum of the four carbonate mineral phases. The Raman shift of the v_1 mode for magnesium carbonates occurs at higher wavenumbers than for calcium bearing counterparts. However, in the case of the double carbonate minerals, the v_1 position depends on whether the Ca and Mg cations are ordered into two different layers as is the case for dolomite, or whether the crystal has a superstructure of calcite with cation ordering within one layer as is the case for huntite (Scheetz 1977). For all Mg-Ca carbonates the v_3 asymmetric stretching mode shows low intensity peaks at *ca.* 1450 cm^{-1}. The v_4 in-plane bending mode occurs as a weak band at *ca.* 700 cm^{-1} (Edwards et al., 2005). The lattice modes involve translatory and rotational oscillations (Gunasekaran et al., 2006) and can be diagnostic of specific mineral phases. For instance, dolomite and magnesite show high intensity peaks at 300 cm^{-1} and 330 cm^{-1} respectively (Edwards et al., 2005).

2.2 Analytical methods

Raman analyses were conducted employing a portable Raman spectrometer (Perkin Elmer, Raman Identicheck), fitted with a 785 nm laser, with CCD detector and fibre optic probe with 70 mV laser power. The fibre optic probe has a 100 µm spot size at a working distance of 7.5 mm. The samples were measured in the spectral range of 1500-150 cm^{-1} at a resolution of 2 cm^{-1}. Each spectrum was collected from 8 scans for 2 seconds at room temperature and repeated six times on randomly selected subsamples in order to ensure representative spectral information. The spectra were averaged, baseline corrected and deconvoluted to be used in monovariable quantification. Data manipulation was performed using the software Spectrum (Perkin Elmer) and PeakFit (Jandel, Scientific Software). A near-infrared spectrometer (Perkin Elmer, Spectrum 100N) was employed in quantification of twenty samples. The powdered samples were measured in glass vials using Near Infrared Reflectance Accessory (NIRA) in the range 10 000-4000 cm^{-1} with resolution 16 cm^{-1}. Each spectrum was collected from 5 scans as an interleaved measurement and displayed in absorbance mode. Each sample was measured six times to

ensure a representative measurement. Data manipulation and chemometric analysis were performed using the software package Quant+ (Spectrum, Perkin Elmer). Samples were quantified using PCR+ and PLS methods with and without corrections. Reference independent corrections were preferred (rather than reference dependent) i.e. second derivative and standard normal variation were applied using parts or the full range of the measured spectra.

The effects of packing on samples were investigated using synthetic magnesium carbonate hydrate (hydromagnesite, Fisher Scientific, lot. n. 1129583). Five gram samples were weighed and pressed into pellets in aluminium holders (20 ton press, Herzog) using 10 kN to 60 kN force. To achieve similar measurements to those of powder in glass vials the compressed pellets were scanned through glass microscopic slides of *ca*. 1 mm thickness. The effect of sample size was also investigated by increasing the depth of hydromagnesite sample from 2.5 mm to 15 mm in a glass vial.

Particle sizes and shapes of the powdered aggregates were monitored by scanning electron microscopy (SEM), model: Zeiss Sigma FEG-SEM and a Malvern Mastersizer 2000 particle size analyzer (PSA), with a Malvern Hydro 2000G dispersion unit. All above mentioned analytical techniques were performed at the University of Brighton, U.K.

X-ray powder diffraction data (performed at the Natural History Museum, London, U.K.) were collected using a Nonius PDS 120 powder diffraction system with an INEL curved position sensitive detector (PSD). This detector has an output array of 4096 digital channels representing an arc of 120° 2θ and permits the simultaneous measurement of diffracted X-ray intensities at all angles of 2θ across 120° with a static beam-sample-detector geometry. Copper $K\alpha_1$ radiation was selected from the primary beam using a germanium 111 single-crystal monochromator and slit system. Horizontal and vertical slits were used to restrict the beam to 0.10 by 5.0 mm respectively. For phase identification, each powdered sample was mounted on a single-crystal sapphire substrate as a thin smear. For phase quantification, each mixture sample was packed into a 1 mm deep well. All measurements were made in reflection geometry with the sample surface (spinning in its own plane) at an angle of 5° to the incident beam. Data collection times were 15 minutes for each sample. NIST silicon powder SRM640 and silver behenate were

used as external 2θ calibration standards and the 2θ linearization of the detector was performed using a least-squares cubic spline function. Search-match procedures using STOE WinXPOW software, containing the Powder Diffraction File PDF-2 supplied by the International Centre for Diffraction Data (ICDD), were employed to identify the mineral phases present.

2.3 Reference material fabrication

Mineral reference materials were fabricated from natural samples of huntite, dolomite and magnesite. Synthetic hydromagnesite purchased from Fisher Scientific (lot no. 1129583) was used as the nearest match to natural hydromagnesite, due to high impurity concentrations in all sampled natural hydromagnesite materials. The dolomite sample contained $CaCO_3$ impurities as evident by staining with 0.25 % Alizarin Red S in 0.25 % hydrochloric acid (HCl). Based on reaction rates with acids, the dolomite standard was purified by treatment with 0.05 M HCl and 0.1 M HCl until the red staining disappeared and was then washed with deionised water. All minerals were powdered, using a ZrO_2 (Fritsch, planetary monomill) ball mill operating at 400 rpm for 10 min, and sieved through a 100 μm mesh to ensure homogeneity.

XRD analysis of the huntite, hydromagnesite and magnesite reference materials showed no resolvable mineral impurities (Figure 2.1), suggesting that if impurities are present they are at concentrations below the detection limit, i.e. less than *ca.* 2 % modal abundance. Dolomite contained traces of calcite which is detectable at 1-2 % level. An assessment of the amount of calcite in the dolomite standard by quantitative phase analysis (QPA) XRD was repeated three times and gave consistent results of 0.024-0.025 fit fraction for calcite, equivalent to 1.6-1.7 wt % calcite. The dolomite concentrations in mixtures of the reference materials were recalculated accordingly. The Raman active vibrational modes for the four fabricated reference materials (Figure 2.2) are in good agreement with published values (Edwards et al., 2005).

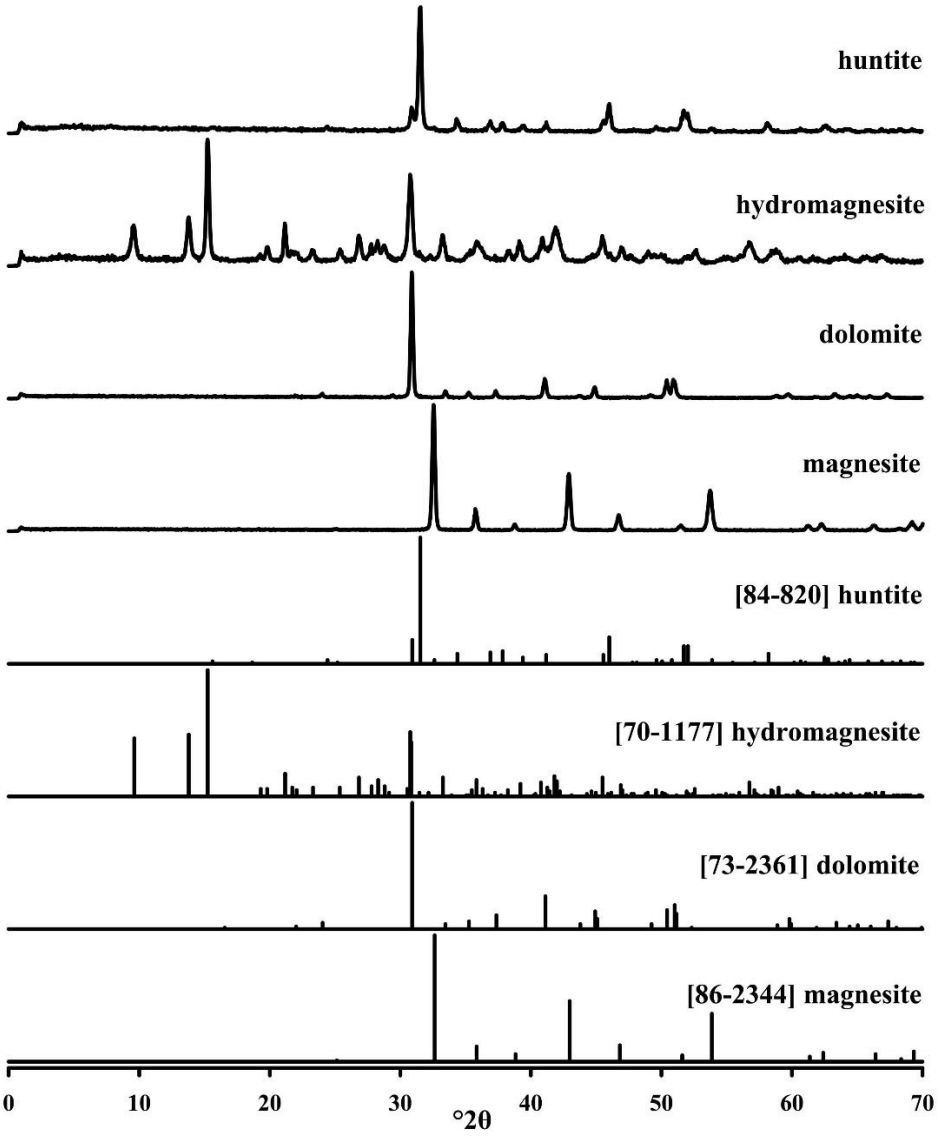

Figure 2.1: XRD-PSD patterns of the phases used to produce the mixtures, together with identification fingerprints from the ICDD database.

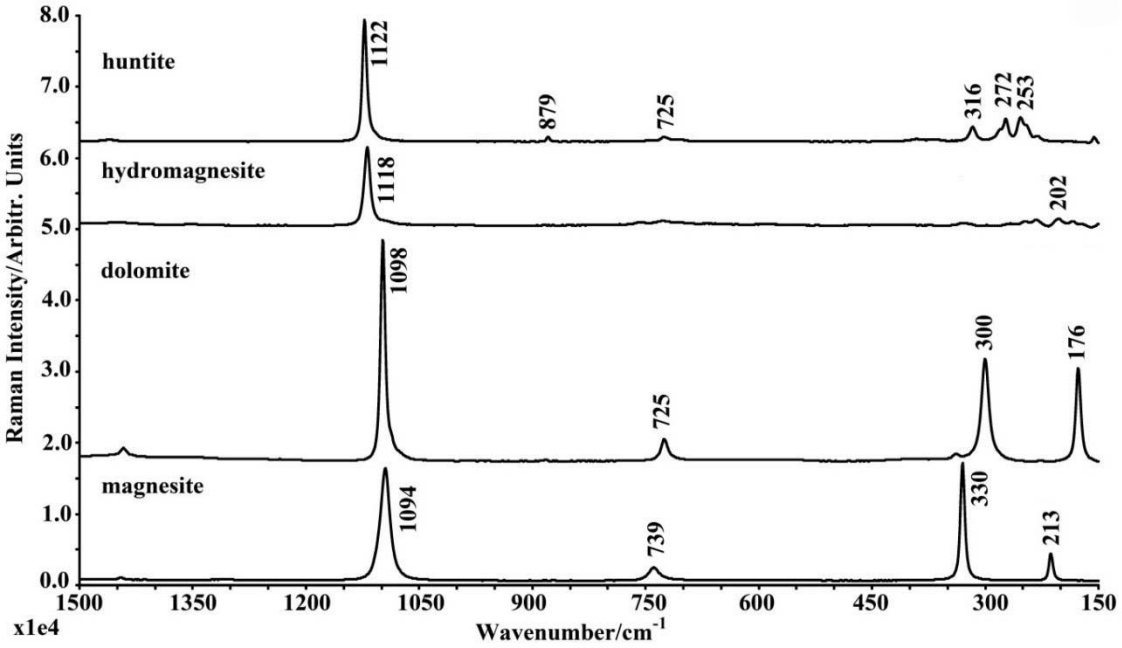

Figure 2.2: Raman spectra of the fabricated reference materials.

SEM analysis indicates that the dolomite sample consisted of well cleaved tabular crystals, up to *ca.* 8 μm in length (Figure 2.3a). The crystals showed locally intense conchoidal fracturing and were interspersed with abundant finer grained anhedral particles which range in size from a few microns to <0.5 μm. The particles showed the presence of Mg, Ca and C, with no Mn or Fe or trace metals detected, suggesting that the dolomite closely approaches stochiometric [$MgCa(CO_3)_2$]. The huntite sample consisted of uniform platy rhomboidal crystals which ranged in size from 1.5 to 0.5 μm, arranged in *ca.* 10-20 μm wide agglomerates (Figure 2.3b) which showed a correspondence of Ca, Mg, and C. The synthetic hydromagnesite sample consisted of agglomerates of well cleaved platy crystals, showing uneven fracture, with particle sizes ranging from *ca.* 1.5 μm to *ca.* 0.1 μm (Figure 2.3c). The magnesite sample consisted of conchoidal fragments of the mineral, which ranged in size from *ca.* 2 μm to *ca.* 0.1 μm, together with lesser quantities of large (2-6 μm length) variably fragmented equant rhombic crystals, which displayed well developed cleavages (Figure 2.3d). The powder was devoid of evidence for elements other than Mg and C, suggesting that the crystals approached stochiometric [$MgCO_3$].

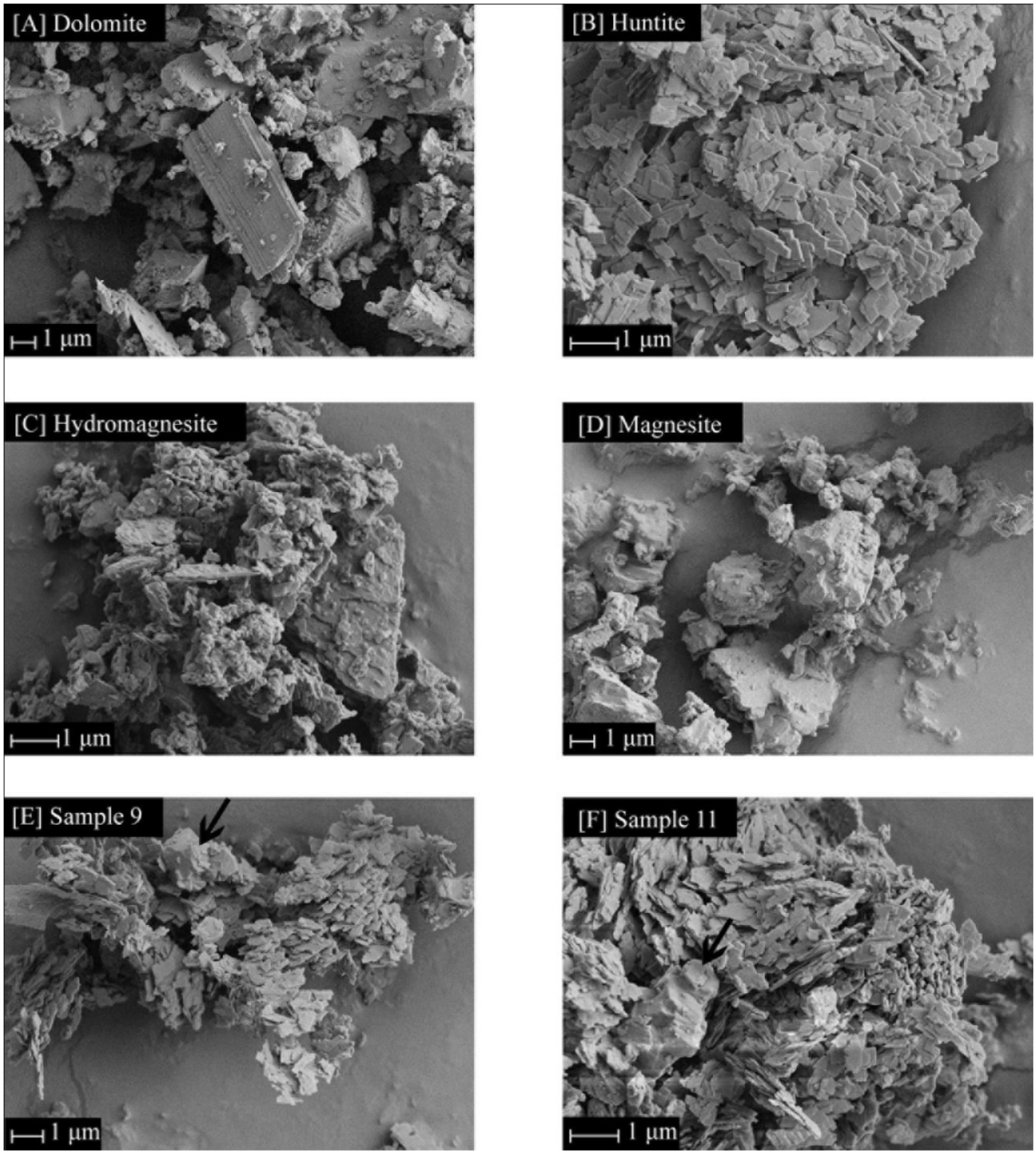

Figure 2.3: Back-scattered scanning electron microscope images of reference materials and samples. a) Dolomite reference material, b) Huntite reference material, c) Synthetic hydromagnesite reference material, d) Magnesite reference material, e) Aggregate of interspersed hydromagnesite and huntite platelets, with conchoidal fractured magnesite rhomb, marked with arrow (sample 9, Table 2.1), f) Aggregate of micron-sized huntite plates, interspersed with similarly sized fragments of dolomite, alongside a *ca*. 1.4 µm long residual coarse grained dolomite crystal, marked with arrow (sample 11, Table 2.1).

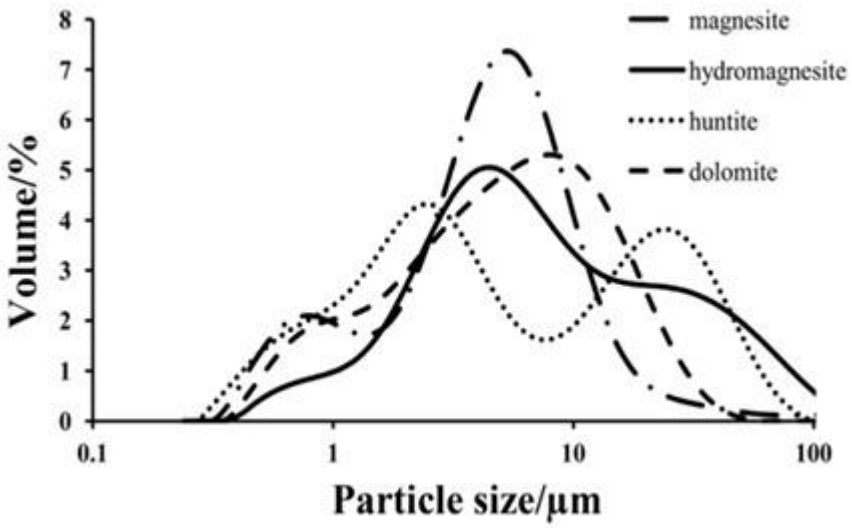

Figure 2.4: The particle size analysis by laser diffraction showing volume distribution profiles on logarithmic scale of the four fabricated reference materials. See text for details.

PSA analysis of the fabricated reference materials indicated a measured mode grain size of 4-7 μm. The minerals showed a size distribution profile consistent with SEM evidence for agglomerations of particle aggregates (Figure 2.4). The agglomeration of particles was particularly evident in huntite, where, although there were no particles bigger than *ca*. 1.5 μm observed under SEM, presence of agglomerates caused huntite's particle size distribution measured by laser diffraction to show two different modes.

The four reference material powders were weighed and mixed in varying proportions. The sample mixtures (1.5 gram) were weighed using 4-place analytical balances and manually mixed for 20 minutes in glass vials (25 ml). Mixtures of the minerals were constructed with huntite and hydromagnesite as the main components. Dolomite and magnesite were used in modal abundances up to 16 weight in weight percentage (Table 2.1). The lower concentrations for magnesite and dolomite were used because the prime industrial interest is currently in huntite and hydromagnesite (as fire retardant fillers in plastics) where higher contamination would not be acceptable. Dolomite and magnesite are in this case viewed as impurities. The homogeneity and particle size distribution of the mixed powders was monitored by SEM (e.g. Figure 2.3e and 2.3f). Spectroscopic analyses were performed on the day of mixture preparation from lightly pressed samples in aluminum sample holders. Twenty samples were prepared to construct the quantification models. To provide overall method error, fifteen randomly selected

samples were employed in calibration and five mixtures were used to test the quantification procedures.

Sample	Dolomite [%]	Magnesite [%]	Huntite [%]	Hydromagnesite [%]
1	12.07	7.96	15.06	64.92
2	-	5.02	92.96	2.02
3	12.05	-	-	87.95
4	8.02	11.92	50.07	29.99
5	2.02	3.96	32.10	61.93
6	14.03	2.00	62.04	21.93
7	15.99	-	84.01	-
8	-	16.09	-	83.91
9	6.01	14.01	69.97	10.01
10	10.01	9.96	39.94	40.09
11	7.87	12.09	70.24	9.80
12	4.00	6.01	-	89.99
13	-	-	25.79	74.21
14	-	-	50.29	49.71
15	14.93	4.27	-	80.80
16	5.98	15.98	78.04	-
17	-	2.12	4.02	93.86
18	13.85	5.13	10.95	70.08
19	-	-	100	-
20	-	-	-	100

Table 2.1: Mixture compositions as weight in weight percentage [%] - minerals were weighed on an analytical balance to 0.01 mg for one gram samples giving an error 0.001 %.

2.4 Results

2.4.1 Quaternary quantification of Mg-Ca carbonate mixtures by NIR

All near-infrared spectroscopic measurements of carbonate standards and powdered mixtures displayed a significantly curved baseline (Figure 2.5). This was adjusted by automatic baseline correction.

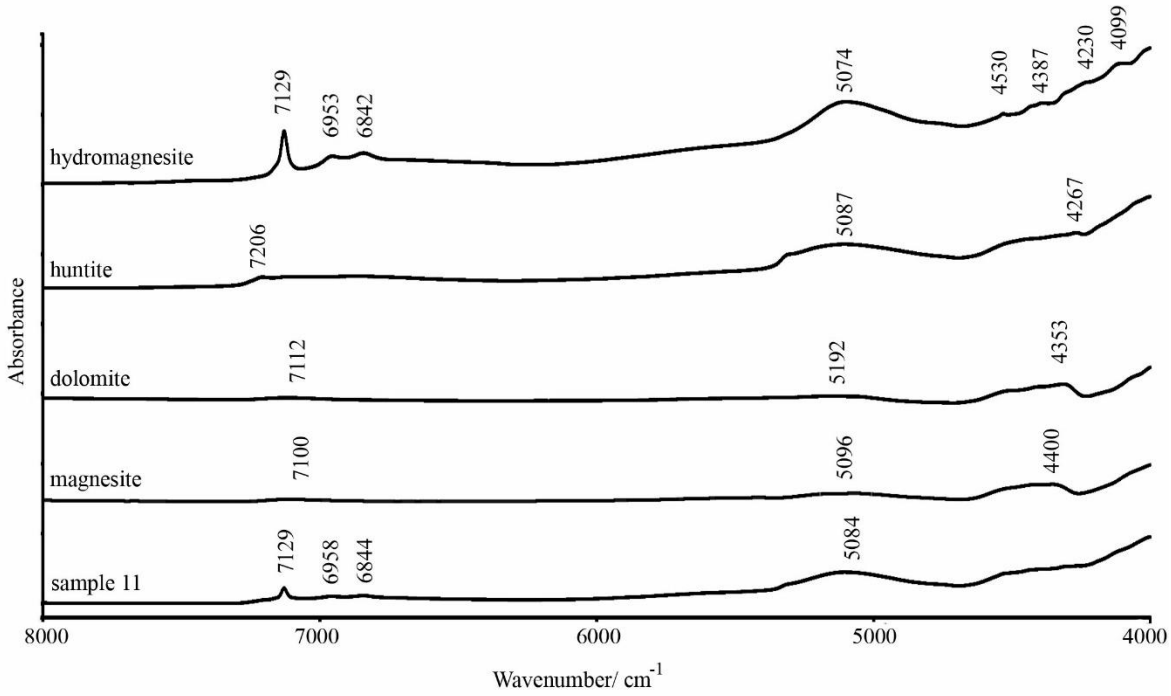

Figure 2.5: Examples of uncorrected NIR spectra - labelling band centre, spectra are offset for clarity. For composition of sample 11 see Table 2.1.

The near infrared spectra of standards after correction are presented in Figure 2.6 (more detailed view of overlaid spectra can be found in Appendix, Figure A.1). The quoted carbonate spectral band wavenumbers vary slightly between presented figures due to NIR measurements being collected at the resolution of 16 cm^{-1} and / or baseline correction.
The spectrum of hydrated magnesium carbonate (hydromagnesite) is distinctly different to the measured non-hydrous minerals due to presence of crystalline water and hydroxyl (OH) groups which are manifested by a sharp band at 7129 cm^{-1} (assigned to OH stretch overtone) followed by doublet peak at 6955 and 6844 cm^{-1}, a strong peak at *ca.* 5099 cm^{-1} and multiple weaker peaks below 4600 cm^{-1}. Also a very broad weak peak is evident at 8365 cm^{-1}.

Huntite, dolomite and magnesite show similar near-infrared spectra. The carbonate minerals characteristically show broad bands which could be described as three main peak areas at *ca.* 7100 cm^{-1}, 5100 cm^{-1} and 4400 cm^{-1}.

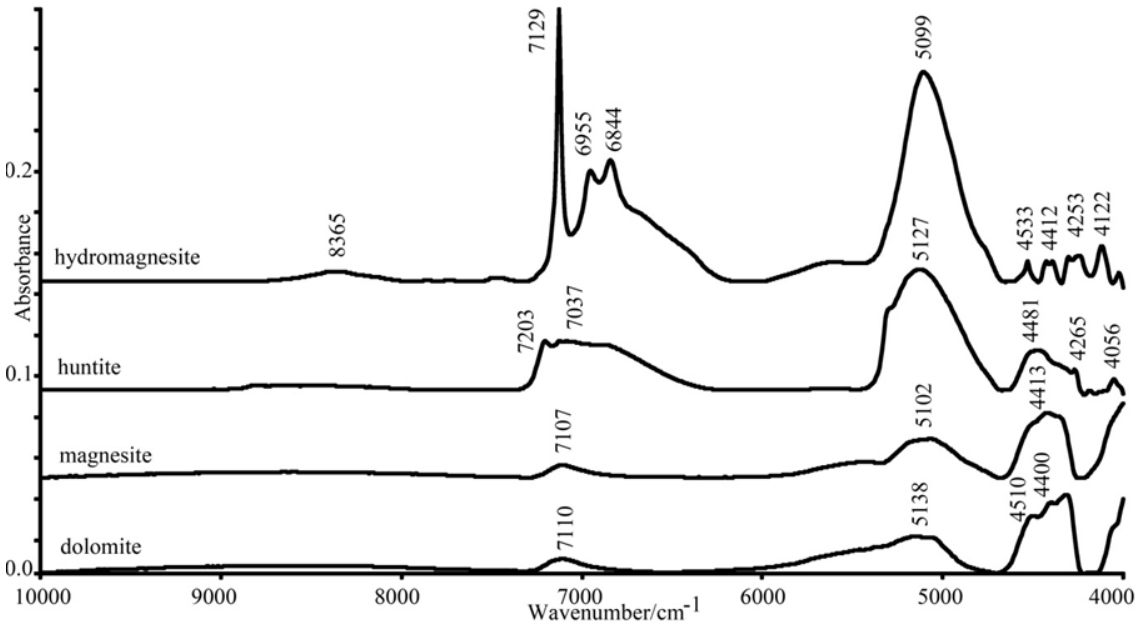

Figure 2.6: Near-infrared spectra of mineral standards after baseline correction –labelling band centre, spectra are offset for clarity.

Spectra of four representative mixtures are shown in Figure 2.7 (further examples of raw spectra can be found in Appendix, Figure A.2). The spectra are shown with decreasing hydromagnesite concentration (from top to bottom: 64.92 %, 21.93 %, 10.01 % and 0 % respectively). It is apparent that the hydromagnesite contribution to the spectra is dominant even at lower concentrations at *ca.* 22 % of weight fraction.

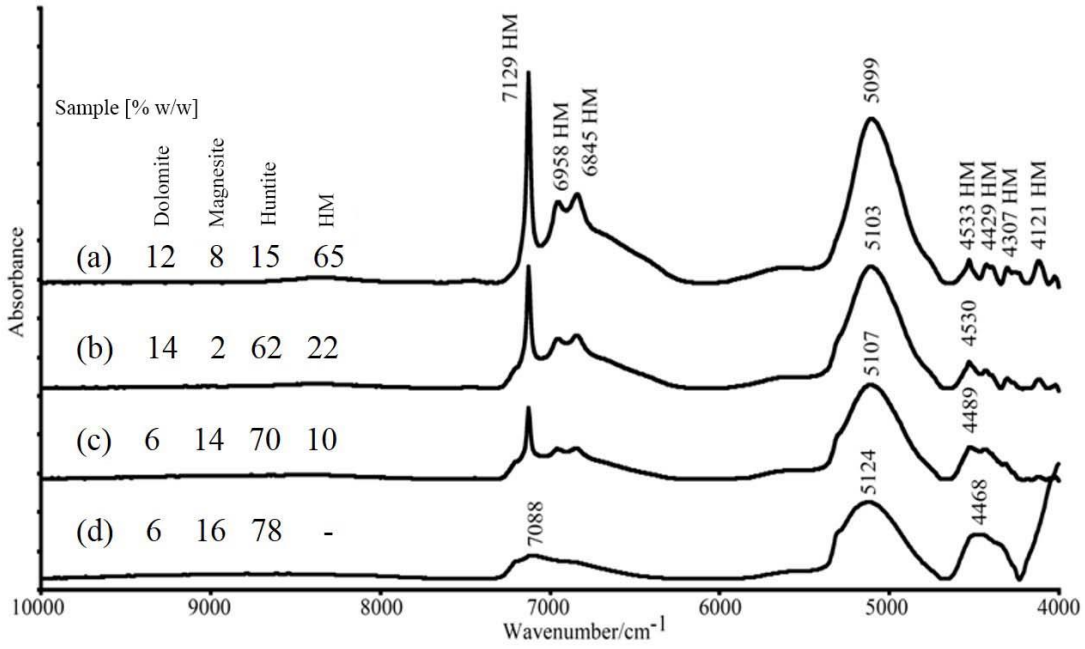

Figure 2.7: Near-infrared spectra of mixtures after baseline correction –(a) sample 1, (b) sample 6, (c) sample 9 and (d) sample 16 (Table 2.1) with their approximate compositions, labelling HM - hydromagnesite, labelling band centre, spectra are offset for clarity.

Chemometric techniques, Partial Least Square (PLS) and Principal Component Regression (PCR+) (Perkin Elmer, Spectrum Quant+), were employed to quantify the four component mixtures. To remove the sloping baselines, the spectra were either pre-processed using second derivatization (9 points) or automatically baseline corrected with the Standard Normal Variate (SNV) algorithm applied. Near-infrared spectra of mineral standards as second derivatives (9 points) are shown in Appendix, Figure A.3. Different ranges of the spectra were chosen 10000-4000, 6200/6000-4000 and 4670-4000 cm^{-1} respectively. A group of randomly selected (five) samples were measured to test the methods. The calibrations were assessed by two statistical errors i.e. total error and error on values. The total error was calculated as a difference between measured and true value of a quantity of interest i.e. concentration of the individual minerals in mixture (Total error, Table 2.2). All calculated total errors were in order of 5 % or larger. Total errors were then recalculated per component value (Error on value, Table 2.2). The error on value is calculated as total error subsequently divided by the component value and expressed as a percentage. Errors on value for this particular calibration were in the order of *ca.* 27 % or greater.

Method	Range [cm^{-1}]	Correction	Total error [%]	Error on value [%]
PCR+	10000-4000	Second derivative	6.08	34.0
PCR+	6200-4000	Second derivative	5.40	27.2
PCR+	4670-4000	Second derivative	5.32	32.9
PCR+	10000-4000	SNV	13.32	237.3
PCR+	6000-4000	SNV	7.71	97.1
PCR+	4670-4000	SNV	6.94	41.1
PLS	10000-4000	Second derivative	5.86	30.6
PLS	6200-4000	Second derivative	5.45	29.5
PLS	4670-4000	Second derivative	6.46	46.8
PLS	10000-4000	SNV	13.56	224.3
PLS	6000-4000	SNV	6.09	68.2
PLS	4670-4000	SNV	7.41	35.9

Table 2.2: Assessment of NIR quantitative calibration models for quaternary mixture where PCR+ = principal component regression, PLS = partial least squares and SNV = standard normal variation.

The graphs displayed in Figure 2.8 show the best fit which was gained by PCR+ method using second derivative in range 4670-4000 cm^{-1}. The graphs of estimated versus specified values show that the calibrations for individual minerals do not follow linear relationship but give values with a rather polynomial profile. Moreover, measurements for lower concentration components were erratic with detection of absent components which in case of huntite was up to 18 % (instead 0 %). This method operated with average total error of 5.32 % and average error on value of 32.9 %.

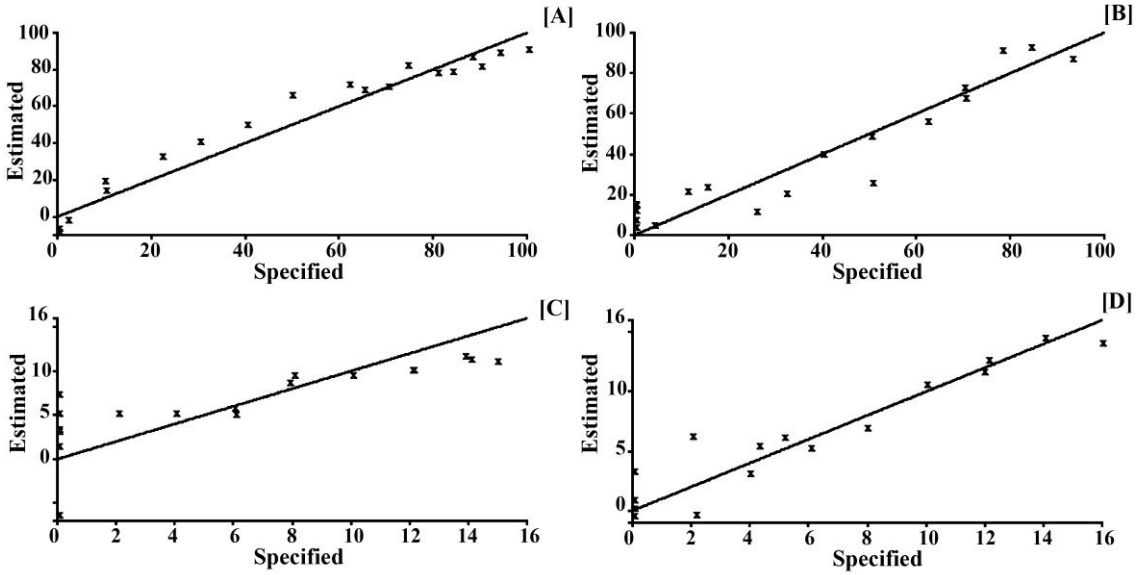

Figure 2.8: NIR calibration graphs for PCR+ method (in range 4670-4000 cm^{-1}) with second derivatives correction applied showing estimated versus specified values: a) Hydromagnesite, b) Huntite, c) Dolomite, d) Magnesite.

Hydromagnesite shows a strong sharp peak at 7129 cm^{-1}. The intensity of this peak (measured as peak maximum) in absorbance (baselined at 7171 cm^{-1} and 7060 cm^{-1}) was plotted against weight fraction of hydromagnesite to provide a monovariable calibration curve (Figure 2.9).

The calibration curve shows visual signs of deviation from linearity with R^2 value of 0.9499 for linear fitting and R^2 value of 0.9880 for polynomial fitting.

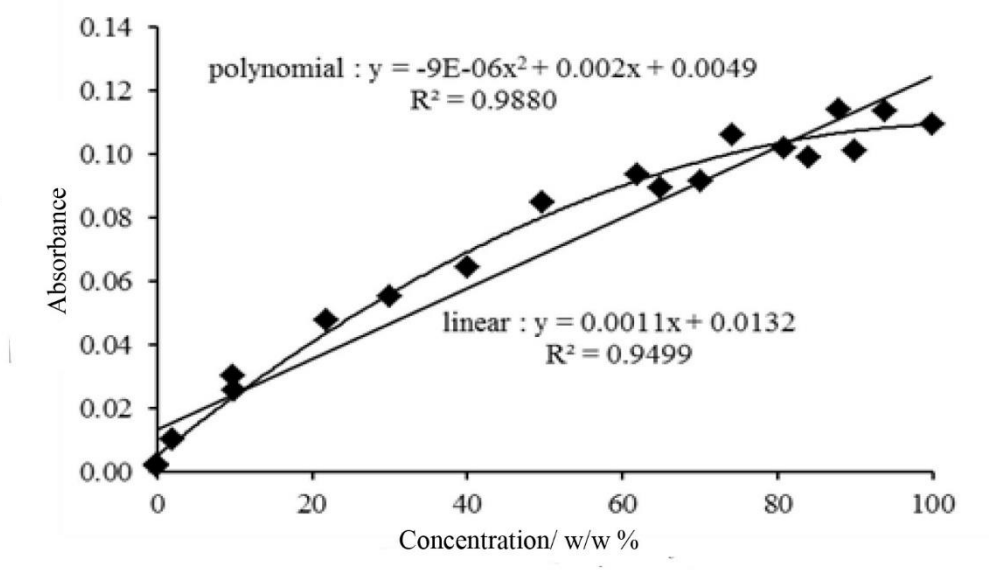

Figure 2.9: NIR monovariate calibration graph for hydromagnesite at 7129 cm^{-1} peak.

Sample preparation effects - Compression and sample size (thickness)

Packing of a sample is one of the main reasons for non-linearity of NIR calibrations reported in literature (Blanco et al., 1999). To ascertain the effects of compression and sample size two experiments were performed using the hydromagnesite sample. Seven hydromagnesite samples of varying compression were investigated in the experiment looking at the effect of compression on the NIR spectra. The results showed a nearly linear regression curve when plotted as absorbance to force (Figure 2.10) in the measured range between uncompressed sample and force up to 60 kN used to press a pellet. Compacting of the sample contribution to the overall absorbance (intensity) was *ca.* 17 % of the total absorbance when calculated against maxima found for sample compressed at 60 kN.

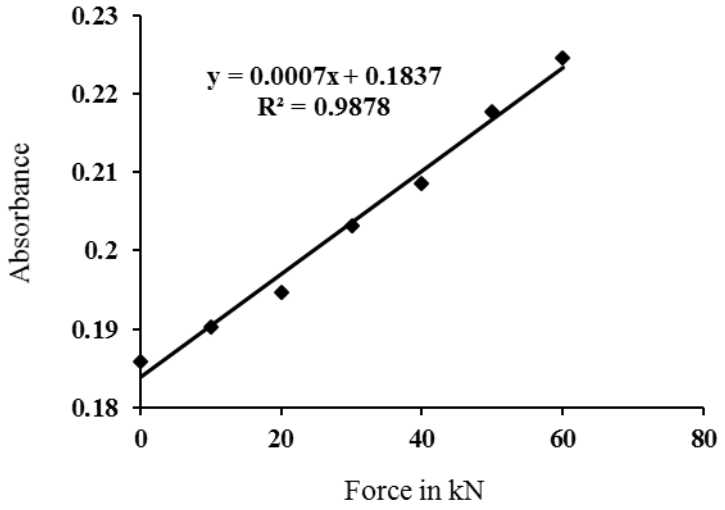

Figure 2.10: Effect of sample compaction on NIR spectrum of hydromagnesite sample plotted as force against NIR absorbance.

Sample size effect was measured as varying sample thickness for 2.5 mm, 5 mm, 10 mm and 15 mm and the values are shown in the Table 2.3. All different sample sizes measured varied within 2 % of absorbance.

Sample thickness [mm]	Absorbance at 7129 cm^{-1}	Total [%]
2.5	0.1895	100.0
5	0.1858	98.0
10	0.1859	98.1
15	0.1855	97.9

Table 2.3: Effect of sample size on NIR spectrum of hydromagnesite.

2.4.2 Quaternary quantification of Mg-Ca carbonate mixtures by Raman

Examples of raw, baseline corrected and deconvoluted Raman spectra are shown in figure 2.11. (further examples of RS data can be found in Appendix, Figure A.4). The spectra of four component carbonate mixtures show variable numbers of peaks of different intensities and merged multi-component bands. In particular, the two strong intensity doublet peaks assigned to the C-O symmetric stretch (v_1 mode) overlapping huntite with hydromagnesite and dolomite with magnesite occur in the ranges of *ca.* 1121-1118 cm^{-1} and 1097-1095 cm^{-1} respectively (Figure 2.12a). In the lattice mode region the spectra are characterized by a number of medium and low intensity vibrations, which can be assigned to the four constituent minerals. The v_1 modes of the constituent minerals and peaks in the lattice mode region (magnesite at 330 cm^{-1}, dolomite 300 cm^{-1}, huntite 272 and 252 cm^{-1} and hydromagnesite 202 and 184 cm^{-1}) were used to identify the contribution of each mineral phase to the observed spectra (Figure 2.12) and employed to construct quantitative calibration procedures, applying monovariable and multivariable regressions to the spectra.

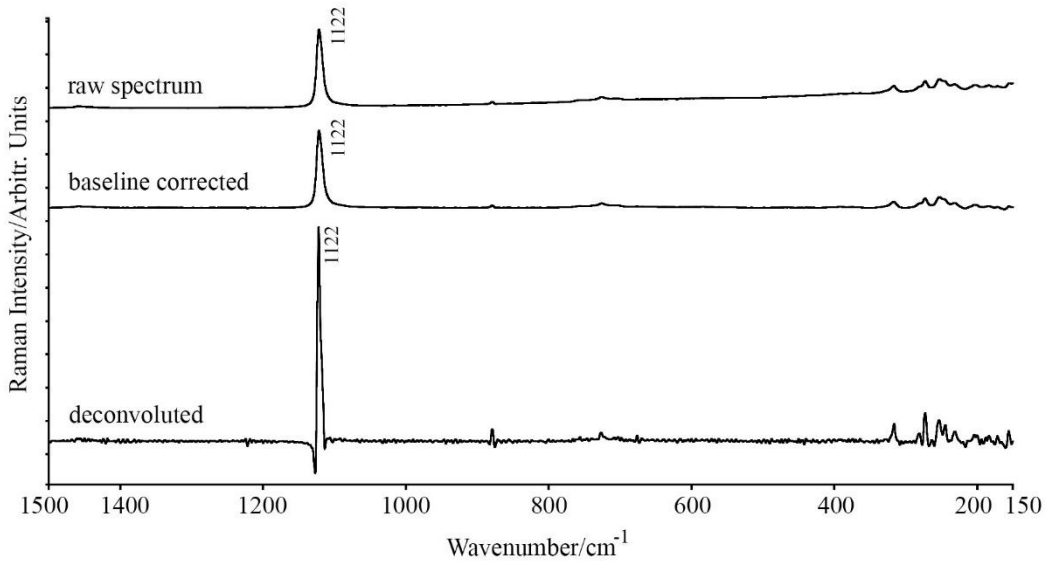

Figure 2.11: Examples of mixed carbonate Raman spectra (containing 50 % huntite and 50 % hydromagnesite) shown as uncorrected, baseline corrected and deconvoluted spectra. Spectra are offset for clarity.

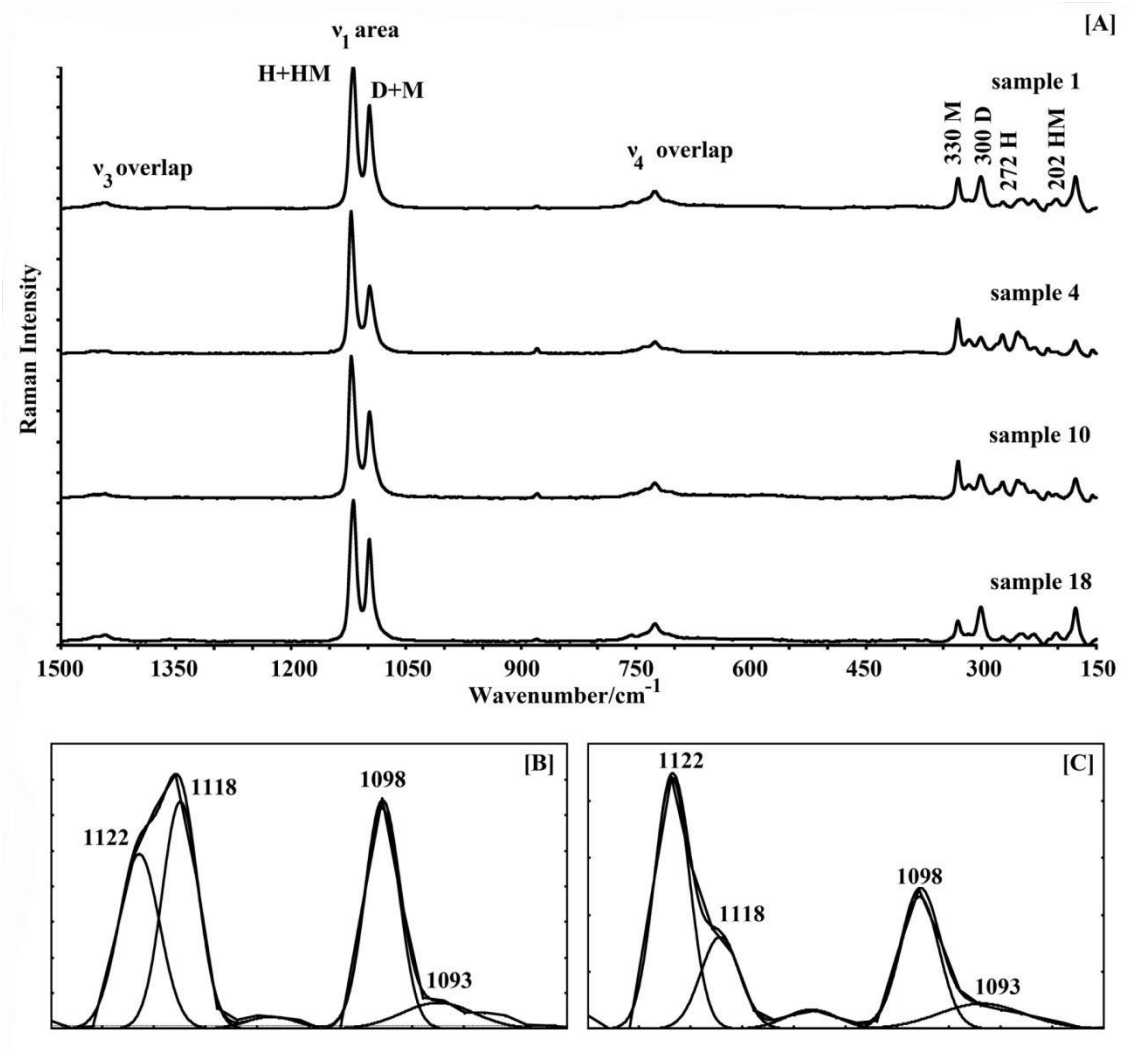

Figure 2.12: a) Representative Raman spectra of mixed carbonate powders: sample 1, sample 4, sample 10, sample 18 (Table 2.1) where abbreviated labelling is as follows: H = huntite, HM = hydromagnesite, D = dolomite and M = magnesite. b) Detail of curve fitting for Raman spectra after deconvolution in the range 1130-1080 cm^{-1} (sample 1, Table 2.1). c) Detail of curve fitting for Raman spectra after deconvolution in the range 1130-1080 cm^{-1} (sample 10, Table 2.1).

The monovariable calibration method was created using maximum peak heights of the most intense bands plotted against weight fraction. Maximum peak heights were utilized rather than peak areas or measurements using widths (FWHM) due to varying widths of RS peaks described for carbonate minerals (Kaabar et al., 2011) and possibility of increasing erroneous measurements due to spectral overlaps.

Huntite and hydromagnesite were quantified using the ν_1 mode peaks. In the case of magnesite and dolomite this was done in conjunction with the medium to high intensity lattice mode bands at 330 cm^{-1} and 300 cm^{-1} respectively. The calibration was described

by a linear regression trend line for each mineral (Figure 2.13), R^2 values and an error on test samples were calculated. The correlation coefficients for individual minerals were R^2 = 0.9860, 0.9859, 0.9734 and 0.9505 for huntite, hydromagnesite, dolomite and magnesite respectively (Figure 2.13). The average difference between the calculated and real value of test sample mineral concentration (sample error) was on average 20 % of its value. To evaluate repeatability of the spectroscopic measurements and data manipulation, replicate measurements were taken on one sample to provide six groups of six measurements. Spectra in each group were averaged, baseline corrected, deconvoluted, peak fitted and compared. The relative standard error for quaternary mixtures for these six measurements was calculated to be on average 9.6 % on v_1 peak height that was used in the monovariable model. This error includes potential effects of mixture inhomogeneities. Details are shown in Appendix, Table A.1- Repeatability of the Raman spectroscopic measurement and data manipulation.

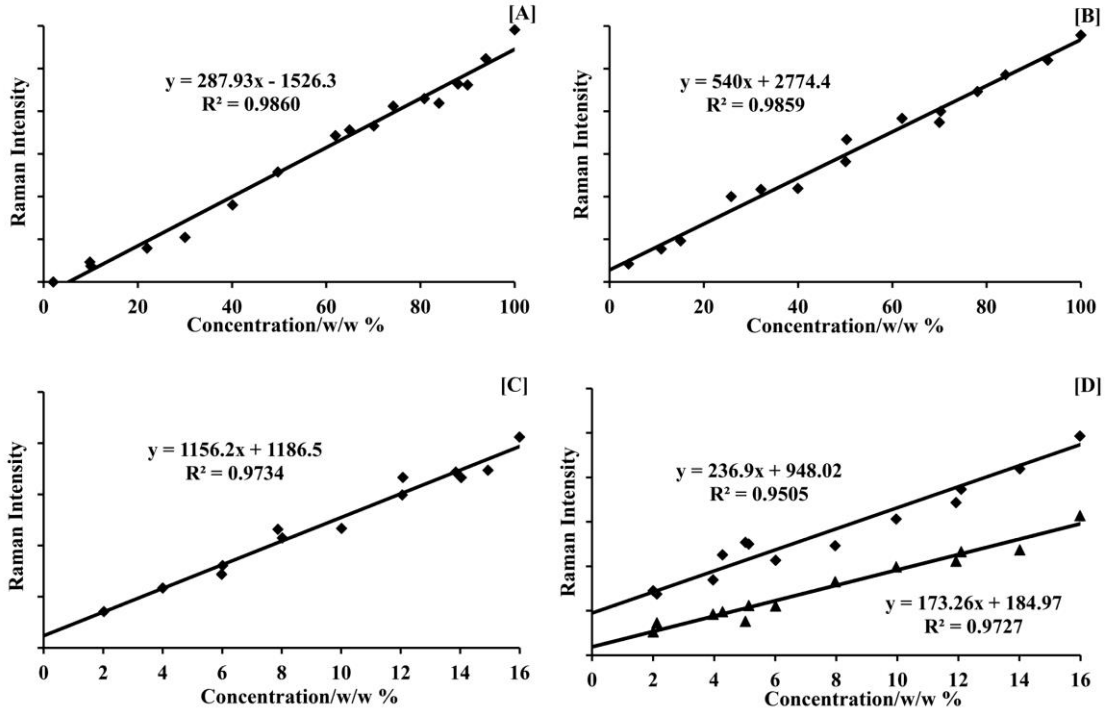

Figure 2.13: RS calibration graphs for monovariable method in absolute values plotted against weight fraction: a) Hydromagnesite - peak height at *ca*. 1118 cm^{-1}, b) Huntite - peak height at *ca*. 1122 cm^{-1}, c) Dolomite - maximum peak height at *ca*. 1097 cm^{-1}, d) Magnesite - peak height at *ca*. 1094 cm^{-1} (diamonds) and at *ca*. 331 cm^{-1} (triangles).

The multivariable methodologies based on Principal Component Regression (PCR+) and Partial Least Squares (PLS) were conducted with software Spectrum Quant+ (Perkin Elmer) applied to the spectra. Two models were created, with and without an applied normalization algorithm, i.e. Standard Normal Variate (SNV) for both multivariable methods. SNV transformation was used to remove the multiplicative interferences of scatter. The models were described by the error on test set samples. A summary of the calibration parameters examined for PCR+ and PLS methods are presented in Table 2.4. Results show that the multivariable methods achieved superior calibration correlations to the monovariable method, with results further improved by SNV correction. The PCR+ quantification with SNV correction yielded the best results, with calculated average sample error of 10.8 % on values (details are shown in Appendix, Tables A.2-A.6). Graphs for individual components comparing specified *versus* estimated values are shown in Figure 2.14. The calibrations using PCR+, PLS and PLS with SNV achieved sample errors 12.6 %, 13.6 % and 14.0 % respectively. The differences between the six spectroscopic measurements of one sample were found to be on average 9.6 % of the components value after data manipulation. The limit of detection for the Raman spectrometer is *ca.* 2 w/w % or better.

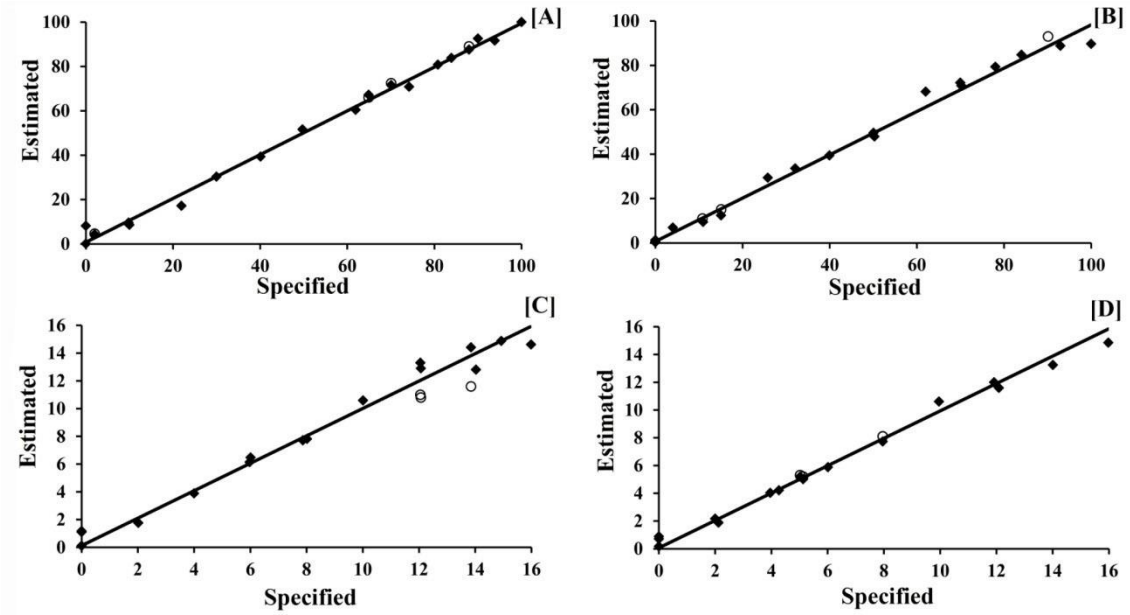

Figure 2.14: RS calibration graphs for PCR+ method with SNV correction applied showing estimated *versus* specified values (solid diamonds) with XRD-PSD data superimposed (open circles): a) Hydromagnesite, b) Huntite, c) Dolomite and d) Magnesite.

2.4.3 Quaternary quantification of Mg-Ca carbonate mixtures by XRD-PSD

To further ascertain the accuracy of the calibration procedures, four samples of mixed powders were quantitatively analysed by XRD. Diffraction patterns of these four mixtures are presented in Figure 2.15. Their phase proportions have been determined by proportional matching the single-phase patterns against each of the mixture patterns using a least-squares fitting program (LinkFit version 1.0.4). The least-squares fits were performed using the moderate-to-high 2θ range, because for this region the PSD records patterns that represent diffraction from close-to-random crystallite orientations for all the phases present. The lower-angle peaks were not used in the fitting as they can arise from preferred orientation of crystallites in the mount and therefore their intensities are less reliable for quantification purposes. Corrections for the effects of X-ray absorption were applied using the mass absorption coefficients for each phase in the mixture in order to convert from pattern fit proportions to weight percent values (Le Blond et al., 2009). The XRD-PSD quantification yielded results with calculated average sample error of 14.06 % on values (Table 2.4). The peak intensity for hydromagnesite was significantly lower than the intensities of the other carbonates.

Analytical method	Calibration method	Correction	Error Total [%]	Error on values [%]
RS	PCR+	none	2.3	12.6
RS	PCR+	SNV	1.7	10.8
RS	PLS	none	2.4	13.6
RS	PLS	SNV	1.9	14
RS	monovariable	none	3.1	20
XRD-PSD	least-squares fitting	absorption	1.2*	14.1

Table 2.4: Assessment of quantitative calibration models for quaternary mixture where RS = Raman spectroscopy, PCR+ = principal component regression, PLS = partial least squares, XRD = X-ray diffraction and SNV = standard normal variation. * only 4 samples measured by XRD.

The quantifications by Raman spectroscopy and XRD-PSD were compared to each other by error on sample values (Table 2.4). Both XRD and Raman spectroscopy when combined with PLS showed *ca.* 14 % error on the component value. The average error on values obtained by XRD-PSD was 14 % and by Raman spectroscopy *ca*. 11 % and 20 % for chemometric and monovariable methods respectively. Hence, the results show that both analytical techniques are comparable and successfully quantify carbonate mixtures.

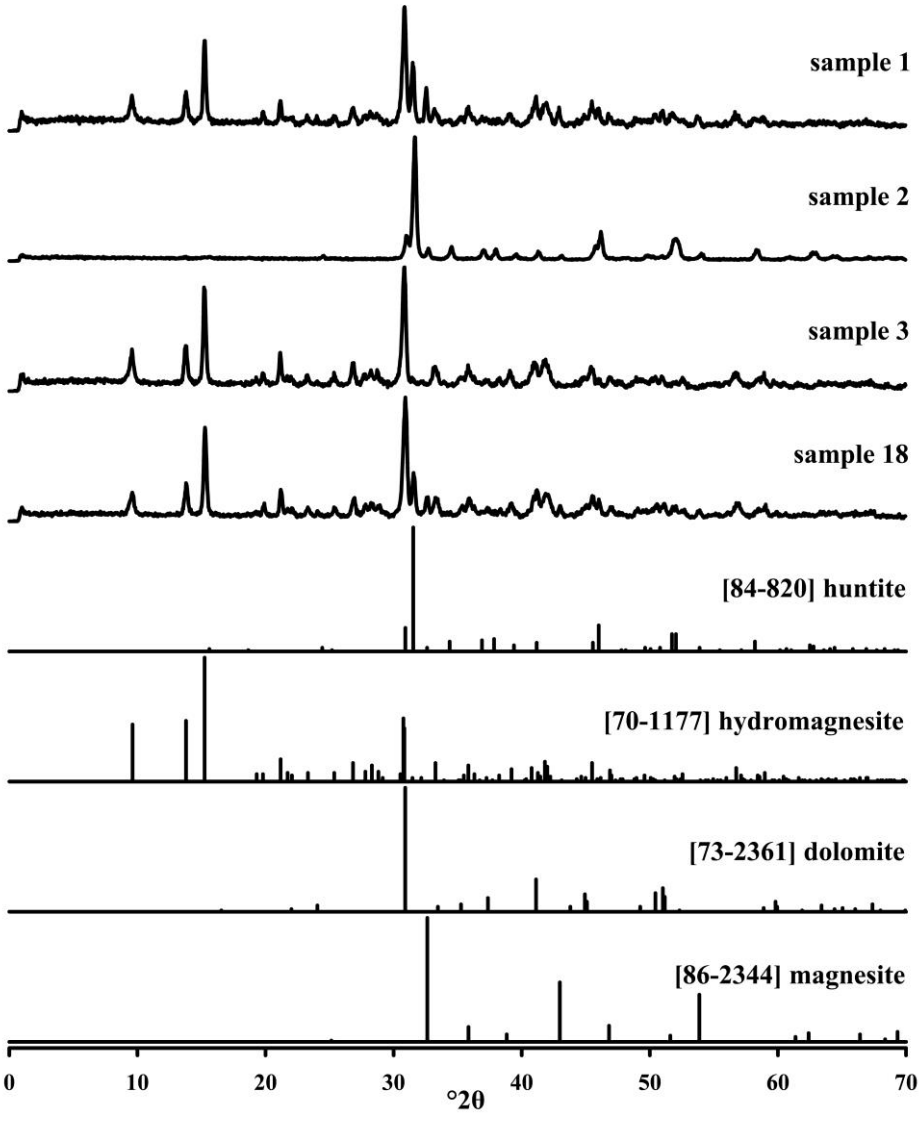

Figure 2.15: XRD-PSD patterns of selected mixtures (samples 1, 2, 3, and 18) (Table 2.1) together with identification fingerprints from the ICDD database.

2.5 Discussion

2.5.1 Near-infrared spectroscopy quantification

NIR spectra showed strong features for hydrated carbonate (hydromagnesite) which to a certain extent obscured the non-hydrous carbonate components in mixtures (Figure 2.7). Therefore the NIR method did not yield a successful four-way quantification model even though data manipulation was performed in combination with several spectral pre-processing methods. These strong modes resulted from OH groups. Because dolomite, magnesite and huntite do not possess any hydrogen bonds within their molecules it is interpreted that all observed bands can be assigned to adsorbed moisture or C-O bands and / or occluded water trapped in intracrystalline defects. Moreover the C-O atoms are close in mass which might be the reason for a low contribution to NIR spectra as their first and strongest overtone lies within the mid-IR spectral range (Stephenson et al., 2001). This appears particularly evident in spectra of magnesite and dolomite.

The NIR spectral intensity is related to concentration although it has been reported that its absolute value can be influenced by sample packing, grain size, presence of air moisture etc. Due to the fact that NIR spectra show generally weak broad overlapping bands there are various chemometric and pre-processing techniques which can reduce this problem to a certain extent by correction of near-infrared spectra e.g. by first or second derivation or by applying normalization algorithms (SNV, MSC) (Blanco 1997).

Particle size effects in NIR spectra are known to have an effect on spectral intensity (Gaffey 1985, 1986). In this investigation powders were finely ground to modal particle sizes between *ca.* 4-7 microns measured by laser diffraction with SEM evidence of even smaller particles *ca*. 1 micron (Figures 2.3 and 2.4). It is possible that the large surface area of particles within the samples had two possible contributions to the observed NIR spectra. Firstly particle size affects light penetration through samples where light travels farther in coarse-grained samples than in very fine powders as most light is scattered at crystal-air interfaces (Gaffey 1986). This phenomenon may also explain why with increasing sample compression the resultant spectra showed higher absorbance as sample compression would serve to decrease the amount of random scattering. Secondly broad weak peaks at *ca.* 7100 cm^{-1} are observed to a greater or lesser extent

in all carbonate samples. Similar peaks were observed in highly hygroscopic indomethacin mixtures by Heinz et al., (2007) falling between *ca.* 7400-6900 cm^{-1}. It is plausible that these bands arise as a consequence of adsorbed moisture although intracrystalline defects hosting occluded water might have a similar effect.

The hydromagnesite concentration was also measured using monovariable calibration where peak height at 7129 cm^{-1} was plotted against weight fraction. The calibration in this part of hydromagnesite spectra shows signs of non-linearity, particularly between 80-100 % weight fractions. Non-linear calibration systems are difficult to handle because traditional chemometric methods based on Beer's law fail to correct major deviation (Blanco et al., 1999). This may be a reason contributing to overall failure of the four – way polynomial calibration method because the software (Quant+, Perkin Elmer) employed to create polynomial calibration although it is specifically designed for IR and NIR offers only a linear solution to quantitative data. The reasons for non-linearity reported in the literature are mainly particle size non-uniformity, packing or high absorption of the sample (Blanco et al., 1999). As the particle size was monitored and the standards exhibited comparable particle size this could be excluded. Sample thickness or path length is source of spectral variability and a critical part of a quantitative measurement (e.g. Bakeev 2008; Germer et al., 2014). In the mid-IR the path length is generally measured in micrometres, or tenths of millimetres, whereas millimetre and centimetre path lengths are used in NIR to measure comparable levels of light absorption (Bakeev 2008). In diffuse reflectance mode, the sample thickness is typically controlled by using samples that are infinitely thick relative to the penetration depth of NIR light into a solid material (Germer et al., 2014). The effect of sample thickness measured in this work ranged from 2.5 to 15 mm and did not show a significant difference in NIR response. The polynomial regression was partially attributed to different densities of the investigated minerals causing packing problems although these might not be the sole cause.

2.5.2 Raman spectroscopy quantification

While it is generally accepted that a linear relationship exists between Raman signal intensity and concentration, the spectral intensity of the Raman shift also relates to several factors, notably polarizability, molecular site symmetries, instrument variables, differences in particle sizes and the degree of order in materials. Further, magnesium and calcium carbonates form anisotropic crystals which can lead to broadening of peaks caused by longitudinal and transverse splitting (White 1974), although results indicate that where the beam sampled area is 100 μm diameter and mode grain sizes are 4-7 μm then the effects of anisotropic optical properties are limited relative to the modal abundance of the constituent minerals within the sampled area.

It is evident that the fabricated mineral standards do not show the same Raman intensity. Given that instrument settings remained constant throughout the analyses and that SEM and PSA indicate fairly uniform particle size distributions, it is likely that differences in intensity stem largely from differences in polarizability of the four mineral species, perhaps, with the intensity increasing with increasing ratio of calcium to magnesium cations in the molecule. However other additional effects may also apply. In the fabricated reference material spectra, the v_1 peak for huntite shows a higher intensity than that of hydromagnesite (Figure 2.2). Given that the synthetic hydromagnesite is texturally comparable to natural hydromagnesite, and is devoid of spectral evidence for short range disorder associated with rapid conditions of synthesis, available data suggests that the principal causative factor for the differences in measured intensities for the two mineral phases stems from a higher electron density in huntite during excitation, relative to hydromagnesite.

The potential effect of particle size on Raman spectral intensity has been investigated in several studies. However, the outcomes are still unclear and in some cases are in contradiction (Pellow-Jarman et al., 1996). To further investigate the possible effect of particle size on Raman peak intensity, separate experiments were undertaken and discussed in the next chapter as well as in the final discussion.

2.6 Conclusion

The findings show it is possible to use Raman to quantify quaternary carbonate mineral mixtures with high accuracy. However, absolute values cannot be used if instrument variables are changed and would require two-point recalibration for different spectrometers and experimental settings. The multivariable chemometric methods gave better results than monovariable peak height calibration. The most accurate results with respect to sample error were provided by the PCR+ SNV method. From multivariable models the calibration employing the PCR+ method achieved lower sample error than that of the PLS method. The best calibration method was found to be principle component regression with SNV correction applied. The sample error for this quantification method was on average 10.8 % of the component value (Kristova et al., 2013). The monovariable linear calibration method gave a strong calibration with R^2 = 0.9860, 0.9859, 0.9734 and 0.9505 for huntite, hydromagnesite, dolomite and magnesite respectively. However independent samples were measured with average sample error of 20 % of component value. The spectral area of the v_1 symmetrical stretching mode proves to be suitable for identification as well as for quantitative work thanks to data manipulation software. Single peak height Raman measurements offer a simple solution where complex mathematical models cannot be applied, for example when dealing with spectra with abnormalities or fluorescence. Four carbonate minerals were investigated by near infrared spectroscopy and their spectra described. However attempted four-way near-infrared calibration did not show satisfactory results but there have been found some interesting facts about the effect of sample compression.

3 The effect of the particle size on the fundamental vibrations of the [CO_3^{2-}] anion in calcite

3.1 Introduction

Explanation of particle size effects on the spectra of carbonate minerals is subject to many theoretical mathematical approaches (e.g. Lane 1999; Hapke 2012) although experimental demonstrations of the effect of the particle shape and its transformation with size reduction are lacking. Calcite was chosen as a model mineral in the experiment because the minerals vibration spectra are firmly established (e.g., White 1974).

The [CO_3^{2-}] anion in calcite shows four internal modes: the v_1 symmetrical stretch (Raman active), the v_2 out-of-plane bend (infrared-active), the v_3 anti-symmetric stretching and the v_4 in-plane bending mode. The latter two are infrared and Raman active (e.g., White 1974). It is well established that the positions of these infrared and Raman bands measured from a single uniaxial calcite crystal are dependent on whether the measurement is taken transversely or longitudinally relative to the optical axis of the crystal (White 1974; Lane 1999). Conversely measurements from powdered samples are assumed to minimize crystal axis dependency, i.e. emissivity of ordinary and extraordinary rays (Lane 1999). Hence measurements taken from powders do not provide a precise representation of either the transverse or longitudinal measurement but fall somewhere between the two (White 1974).

Spectral intensities (infrared absorption and Raman intensity) are generally considered proportional to concentration by Boguer-Lambert-Beer law or by other mathematical formulae derived from the fundamental law of quantitative spectroscopy (e.g., Griffiths and Haseth 2007; Sherazi et al., 2011; Chen et al., 2012; Kristova et al., 2013). However infrared spectra acquired from powdered calcite and other mineral species are known to undergo changes as a function of particle grain size (e.g. Hunt and Logan 1972; Salisbury and Wald 1992; Hirsch and Arnold 1993; Lane 1999). The effect of particle size on the spectral resolution of the fundamental vibrations of the [CO_3^{2-}] anion in calcite were identified in infrared emission studies and have been divided into three classes of behaviour (Hunt and Vincent 1968; Vincent and Hunt 1968; Lane 1999). Type 1 behaviour shows a decrease in spectral contrast with decreasing particle size. Type 2

shows an initial decrease in spectral contrast with decreasing particle size until reaching a critical particle size, at which point the original emissivity trough reverses into a peak (and *vice versa* for reflectance) with decreasing particle size. Type 3 behaviour involves an increase in spectral contrast with decreasing particle size (Hunt and Vincent 1968). The calcite v_3 internal mode shows type 1 behaviour, whereas the ν_2 and ν_4 [CO_3^{2-}] internal modes show type 2 behaviour (Salisbury and Wald 1992; Lane 1999). One of the main conceptual interpretations arising from these differing type behaviours is that two competing factors contribute to the observed spectral response, i.e. part of the spectral signal comes from the specular (surface-scattered) component and part from volume of sample grains (diffuse) component, the relative contribution of the two components to the observed spectral response evolving as a function of grain refinement (Vincent and Hunt 1968).

The Fresnel equation has been employed to predict type behaviour based on the refractive index of calcite (e.g. Hapke 1981; Salisbury et al., 1987; Lane 1999) which contains a real (*n)* and imaginary *(k)* component, where (*n*) indicates refractive index and (*k*) correlates to absorption i.e. the amount of absorption loss when the electromagnetic wave propagates through the material (Griffiths and Haseth 2007). Both *(n)* and (*k)* are dependent on the wavelength. The critical diameter for a transition in optical properties is related to the absorption coefficient (α) and is proportional to wavelength (λ) and (*k*) defined as (e.g. Salisbury et al. 1987; Lane 1999):

$$\alpha = 4\pi k/\lambda \qquad \text{(Equation 3.1)}$$

At the same time the absorption coefficient corresponding to transmittance (*T*) is given by (e.g. Vincent and Hunt 1968; Salisbury et al., 1987):

$$T = e^{-\alpha d} \qquad \text{(Equation 3.2)}$$

where *d* is the mean photon path length through grains. In general when material possesses a sufficiently large *k* and αd is $>> 1$ it means that the surface reflection may also be large and the material is referred to as optically thick (Salisbury et al., 1987). Optically thin materials possess sufficiently small *(k)* values that αd is ≤ 1. Consequently

volume (diffuse) scattering dominates. Accordingly the reflectance spectrum is then qualitatively similar to the transmittance spectrum. With respect to the v_3 internal mode for calcite, the optically thick-thin transition resides in the *ca.* 63 μm (and smaller) particle size fraction (Lane 1999).

Carbonates exhibit a large *k* value over short wavelength intervals associated with their fundamental molecular vibration bands (Salisbury et al., 1987). Details of the real and imaginary indices (*n* and *k*) for calcite can be found in a study by Lane (1999). Semi-quantitative expression of the optical constants (*n* and *k*) in regions of fundamental modes may be substituted into the Fresnel equation. Then calcite's strongest mid-infrared peak ν_3 (at *ca.* 1400 cm^{-1}) corresponds to emissivity minima (low *n* and large *k*) i.e. low volume scattering and high reflectance, the ν_3 peak shows type 1 behaviour (Lane 1999). Based on the same principal, bending mode ν_4 (712 cm^{-1}) is attributed opposite i.e. type 2 behaviour due to larger volume scattering component. Bending mode ν_4 has a lower absorption coefficient, because although ν_4 corresponds to low real part of refractive index *n*, its imaginary part *k* is also lower while the mode ν_4 is located at higher wavelength.

The effect of powder particle sizes on IR spectral measurements has also been explained in terms of Mie theory, which relates the refractive index of a particle relative to the surrounding medium and a size parameter (Hapke 2012). The theory strictly applies to spherical particles that are small in size in comparison with the wavelength of incident light (Conel 1969; Hapke 1981; 2008; 2012). However, particle size reduction often imparts change in particle shapes, the effect of which on IR spectra has been discussed in very few studies and primarily in the context of inhomogeneity in powdered samples (Serna et al., 1987; Pecharroman and Iglesias 2000). However, it has been shown that the reflectance spectra of optically uniaxial (α-Fe_2O_3) particles, measured as bulk material pressed in pellets, changes with the axial ratios of the particles (Pecharroman and Iglesias 2000). From values calculated in the same study it is plausible that prolate spheroidal particles with larger axial ratios show spectra including extraordinary modes while oblate spheroidal particles display only ordinary modes. Furthermore, physical compression, packing and porosity of powdered materials also play important roles in shaping the spectral response (e.g. Salisbury and Eastes 1985; Salisbury and Wald 1992; Hapke 2008).

Infrared and Raman spectroscopies are used for semi-quantitative characterisation of materials utilizing ratios of their peak areas or maximum peak heights. Furthermore identification of materials is often performed by matching a spectrum obtained from a sample to a reference spectrum in a library. However, the effect of particle size causes changes in a spectral signal intensity and clarity of individual peaks as well as changes in peak ratios within one spectrum. Therefore, both the above mentioned qualitative and quantitative characterization can be influenced by effect of particle size and e.g. NASA's The Advanced Spaceborne Thermal Emission Reflection Radiometer (ASTER) library contains reference spectra of three different particle sizes (Baldridge et al., 2009). However, by comparison with infrared studies, particle size effects on Raman spectra are poorly documented. Specifically, it is not known how the type-behaviours of [CO_3^{2-}] internal modes in calcite as described by infrared spectroscopy find expression in relation to particle size effects detectable in Raman spectroscopy. Available evidence suggests that the absolute intensity of the [CO_3^{2-}] internal modes of carbonate minerals do vary as a function of powder particle size ranges (e.g. Pellow-Jarman et al., 1996; Kristova et al., 2013). This study examines the effects of powder particle size ranges and the optically thick to thin transition on the fundamental vibrations of the [CO_3^{2-}] anion in calcite by attenuated total reflectance mid-infrared (ATR-IR) and Raman spectroscopy (RS).

3.2 Materials and methods

Large (*ca.* 7 cm longest dimension - Figure 3.1) transparent euhedral calcite crystals (Iceland spar) were manually crushed and dry-milled using a ZrO_2 (Fritsch, planetary monomill) ball mill operating at 250 rpm for 3 minutes. Six sieved fractions were then washed with absolute alcohol to remove any clinging fines. The two finest grain fractions were prepared as follows. The supernatant from washing the samples was filtered and the obtained powder was split into two parts, one of which underwent additional milling under water at 400 rpm for 20 minutes, collectively yielding a total of eight separate particle size fractions.

Figure 3.1: Calcite sample (Iceland Spar, Beachy Head) prior to milling.

Particle size analysis was performed by laser diffraction using a Malvern Mastersizer 2000 particle size analyzer, equipped with single lens detection and dual wavelength measurement by blue and red light. Samples were measured (over range 0.02-2000 μm) suspended in water using a Malvern Hydro 2000G dispersion unit. The ground calcite samples were analyzed without addition of any surface active agent and without

employing an ultrasonic device. Particle sizes and shapes were ascertained by scanning electron microscopy (SEM) (Carl Zeiss, EVO LS15) utilizing a secondary scattering technique. Samples were mounted on specimen stubs and coated with 4 nm platinum (Quorum, Q150T ES sputter coater).

Mid-infrared spectroscopic measurements were performed using a Perkin Elmer, Spectrum 65 spectrometer, fitted with an attenuated total reflectance (ATR) accessory employing a ZnSe crystal. Measurements through the ATR accessory require good contact between the sample and the ZnSe crystal. This was achieved by uniform light manual compaction. The samples were measured in the spectral range 4000-600 cm^{-1} at a resolution of 4 cm^{-1}. Each spectrum was collected from 16 scans and repeated six times on different subsamples to assure representative spectral information. Raman analyses were conducted using a Perkin Elmer Raman Identicheck fitted with a 785 nm diode laser and with a CCD detector, thermoelectrically cooled to -50 °C. The measurements were acquired utilizing a fibre optic probe (spot size of 100 µm at a working distance of 7.5 mm) at 100 mV laser power. The bulk samples of powdered calcite were measured placed in brass holders and covered by a silica-glass slide to ensure a smooth surface interface. Raman spectra were taken in the spectral range 2000-300 cm^{-1} at a resolution of 2 cm^{-1}. Each spectrum was collected from 8 scans for 2 seconds and repeated six times on different randomly selected subsamples to assure representative spectral information and that sample preparation did not result in the polymorphic transition of calcite to aragonite (e.g., Garcia et al., 2002; Li et al., 2014). The latter mineral would show Raman active bands at 704, 1462, 1574 cm^{-1} (e.g. Edwards et al., 2005) for which no evidence was found in any sample. The limit of detection for the Raman system operating on pressed powders is *ca.* 2 w/w % or better (Kristova et al., 2013). All analyses were conducted at 25 °C, at atmospheric pressure at the University of Brighton U. K.

3.3 Results

3.3.1 Particle size and shape analyses

The mode sizes of grain fractions of the powders were measured as 3 µm, 5 µm, 19 µm, 24 µm, 42 µm, 59 µm, 83 µm and 121 µm by laser diffraction (Table 1). Grain size fractions (≥19 µm modal) were washed prior to analysis to remove clinging fines and showed mono-modal distributions. The finest fractions (3 and 5 µm mode) showed poly-disperse profile distributions (Figure 3.2).

particle size fraction [µm]	mode size [µm] by laser diffraction
106-90	121
90-75	83
75-64	59
64-45	42
below 45	24
below 38	19
fines 1	5
fines 2	3

Table 3.1: Calcite particle size fractions and their mode size, measured by laser diffraction.

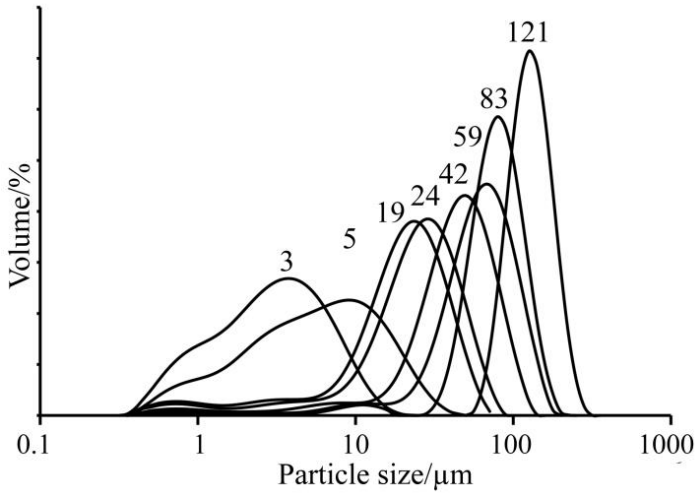

Figure 3.2: Particle size analysis of prepared calcite fractions measured by laser diffraction. Numbers above individual size distributions indicate mode sizes (µm) of the fractions.

SEM analysis indicates that calcite from the largest grain size fraction (121 µm mode) consists of well-cleaved rhombs which show locally intense irregular micro-fracturing, interspersed with finer grained anhedral particles ranging in size from a few micrometers to <0.5 µm (Figure 3.3a). With increasing particle size reduction rhombs become scarcer, show progressively more evidence of micro-fracturing and become more equant (Figure 3.3b, c). Mode size 24 and 19 µm samples contain many irregular fragments with few remaining tabular crystals which range in size from *ca.* 5 to 30 µm (Figure 3.3d, e). The finest fractions are characterized by particles which are largely devoid of planar surfaces. Particle sizes range from *ca.* 6 µm to *ca.* 100 nm and are arranged in agglomerates. The additional very fine particles (<0.4 µm) were not resolved by laser diffraction (Figure 3.3f). SEM also revealed some evidence of snowball structures in the two finest fractions (Figure 3.4).

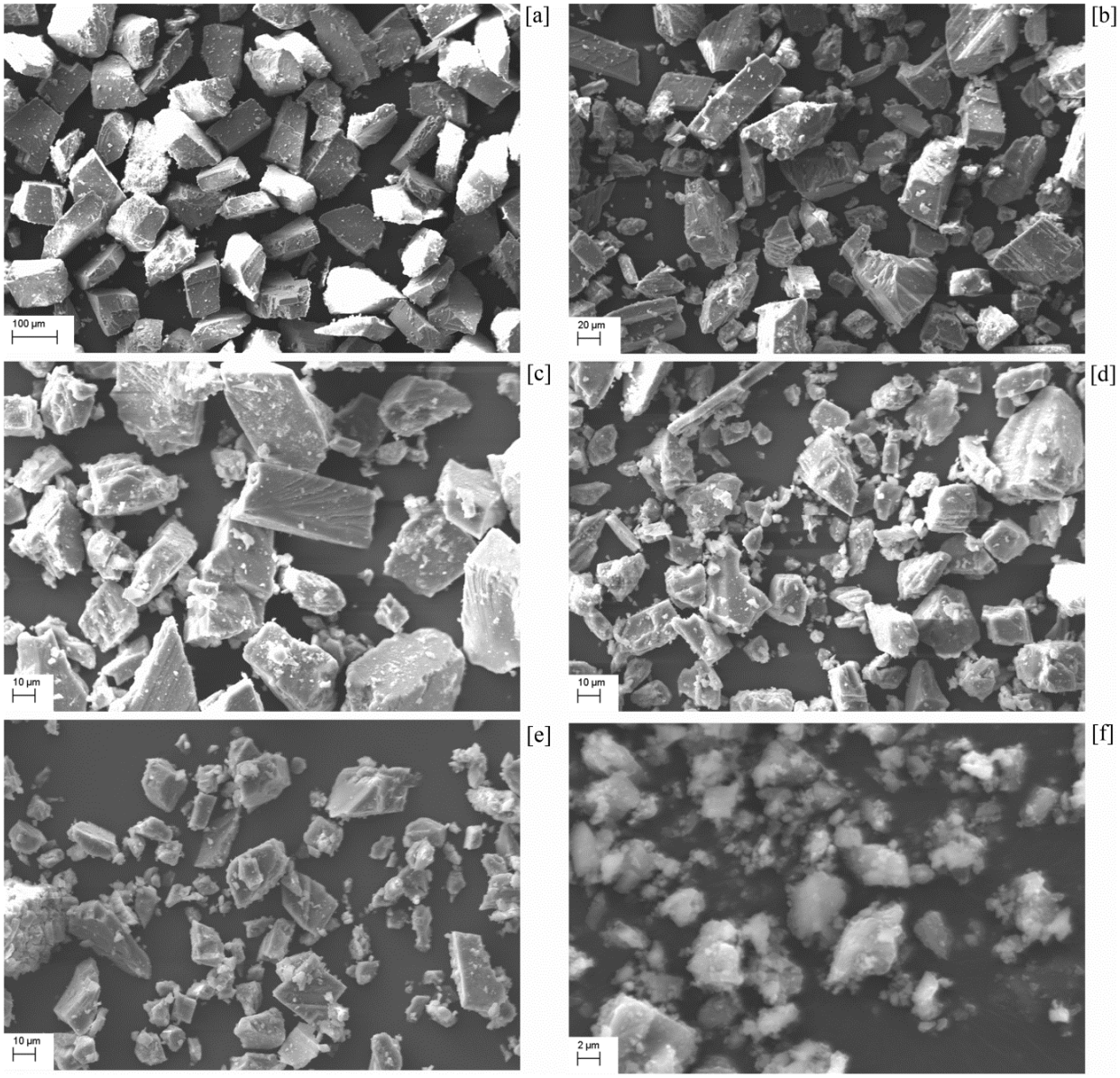

Figure 3.3: Scanning electron microscope images of calcite particles. (a) mode size 121 µm, (b) mode size 59 µm, (c) mode size 42 µm, (d) 24 µm, (e) mode size 19 µm, (f) mode size 3 µm.

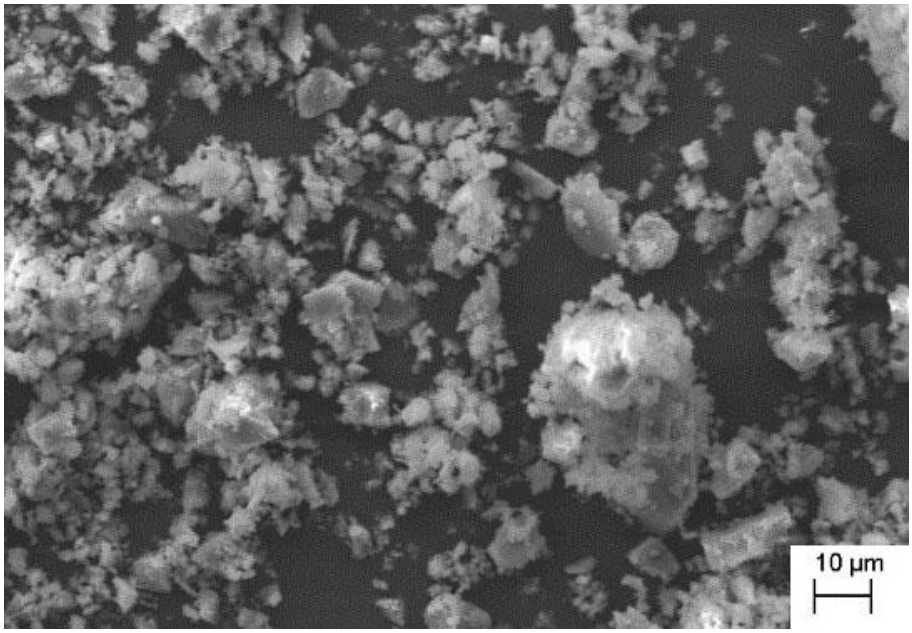

Figure 3.4: Scanning electron microscope image of calcite particles (mode size 5 µm) showing presence of agglomerates (snowball structure).

3.3.2 Mid-infrared spectroscopy

The ATR-IR spectrum of Iceland spar (121 µm powder) is shown in Figure 3.5. The spectrum shows the dominant peak at 1393 cm^{-1} assigned to [CO_3^{2-}] ν_3 asymmetric stretch. The ν_3 peak is asymmetric with a shoulder at 1403 cm^{-1}. The out of plane bending ν_2 band which is the second highest intensity band occurs at 871 cm^{-1} with a subordinate weak peak at 847 cm^{-1}. The in-plane bending mode ν_4 occurs at 712 cm^{-1}. The spectrum also shows weak bands at 1795, 2512, 2874 and 2980 cm^{-1} which are assigned to calcite combination bands and harmonic oscillatory bands (e.g., Böttcher et al., 1997; Cheilakou et al., 2014). The infrared forbidden ν_1 symmetric stretch occurs as a very weak peak at 1088 cm^{-1} (Figure 3.5).

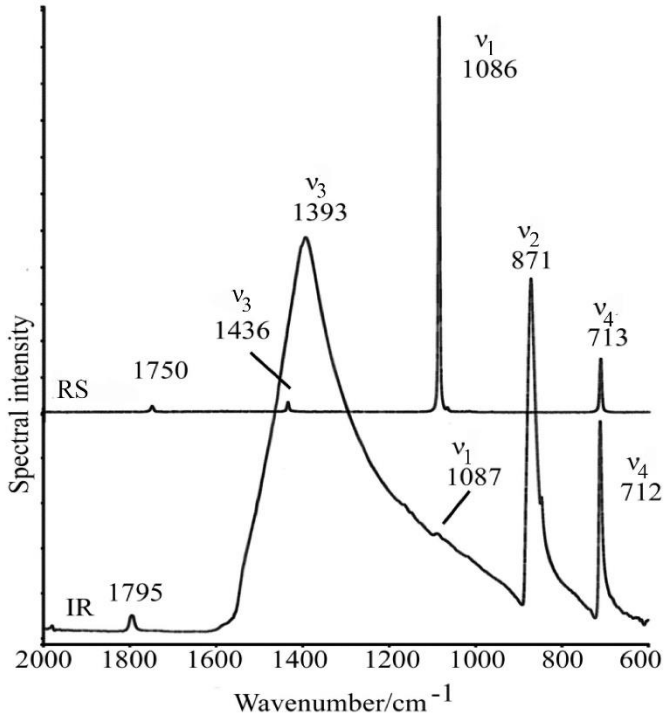

Figure 3.5: The ATR-IR and Raman spectra of powdered (121 µm mode particle size) calcite. Note, the intensity of the v_3 asymmetric stretch and v_4 in-plane bend vibrations of the carbonate anion in Raman spectra of calcite are invariably described as very weak and weak respectively (e.g., Edwards et al., 2005). Conversely v_3 is the strongest feature in the infrared spectrum and v_4 is strong (White 1976).

Measured IR-ATR band maxima in absorbance were used to calculate ratios of the main bending and stretching modes ν_4/ν_3 (712 cm^{-1}/1393 cm^{-1}), ν_4/ν_2 (712 cm^{-1}/871 cm^{-1}) and ν_2/ν_3 (871 cm^{-1}/1393 cm^{-1}). Figure 3.6 shows the absorbance intensity ratios of the bending and stretching modes above plotted against mode grain size fractions. The calculated ratios share the same profile for grain size fractions from 121 µm through to 42 µm mode where the ratios stay unchanged or show very minor changes. Between 42 and 3 µm mode the three ratios sharply decline in a systematic manner from 0.51 to 0.26 [ν_4/ν_3], 0.64 to 0.37 [v_4/v_2] and 0.94 to 0.70 [v_2/v_3], consistent with a non-uniform decrease in spectral contrast of the [CO_3^{2-}] internal modes. The strength of v_4 absorbance decreases preferentially relative to v_2 and v_3. The absorbance intensity of the v_2 mode also decreases relative to v_3 absorbance.

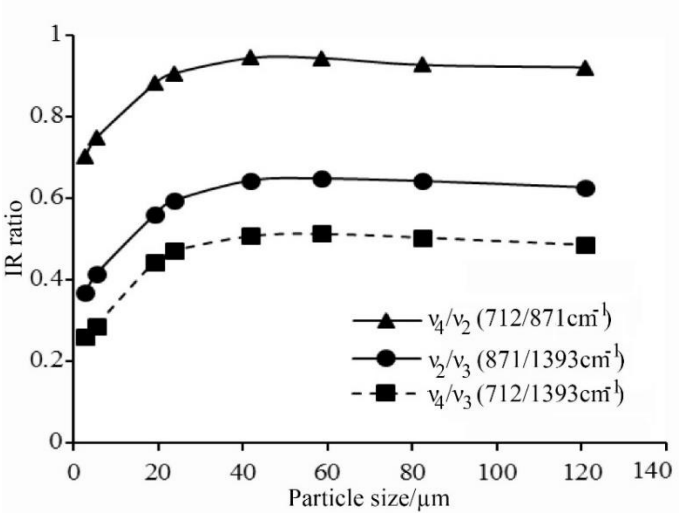

Figure 3.6: Calcite ATR-IR ratios of ν_4/ν_2 (712 cm^{-1}/871 cm^{-1}), ν_2/ν_3 (871 cm^{-1}/1393 cm^{-1}) and ν_4/ν_3 (712 cm^{-1}/1393 cm^{-1}) plotted against grain size (modal sizes in microns).

3.3.3 Raman spectroscopy

The Raman internal modes of calcite were measured at (ν_1) 1086 cm^{-1} (very strong), (ν_4) 713 cm^{-1} (weak) and (ν_3) 1436 cm^{-1} (very weak) (Figure 3.5). The Raman intensity of the bands increased with decreasing particle size from 121 μm until 24 μm mode particle size fraction (Figure 3.7a). Below this size the absolute Raman intensity of all measured bands progressively decreased with decreasing particle size. Detailed views of Raman internal modes changing in intensity with decreasing particle size is shown in Appendix, Figures B.1 and B.2.

Figure 3.7b then shows the [ν_4/ν_3], [ν_1/ν_3] and [ν_4/ν_1] intensity ratios normalised against the corresponding intensity ratio of the 121 μm particle size fraction, with change expressed as a percentage. The [ν_4/ν_3] ratio changes by 22 % (ratio ranges from 4.6 to 5.9). The ratio increases with decreasing particle size over the range 121-59 μm grain size. Thereafter the ratio decreases with decreasing particle size with a possible change in rate of decrease of the ratio between 5 and 3 μm. The average relative standard deviation was calculated to be 4 %. A similar trend is observed for the [ν_1/ν_3] ratio. A significantly smaller change in the [ν_4/ν_1] (*ca.* 5 %) is also evident with the maximum [ν_1/ν_3] ratio obtained from the 42 μm mode sample. The asymmetric stretch (ν_3) is a very weak band in Raman spectroscopy (RS) nevertheless it was clearly resolved and reproducible at all experimental stages.

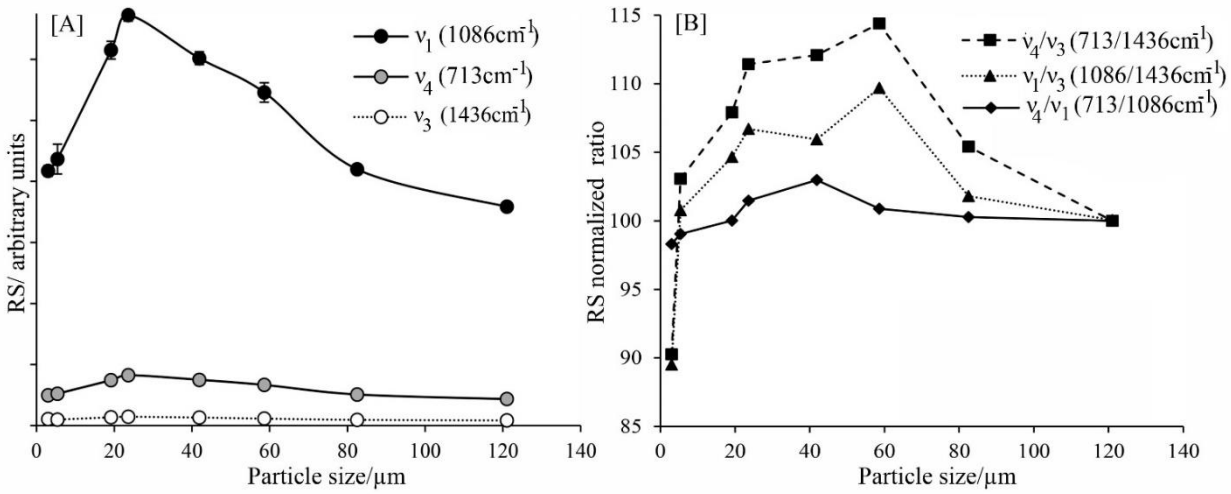

Figure 3.7: [A] Raman intensity (peak heights in absolute values) plotted against grain size (modal sizes in microns). [B] Raman ratios ν_4/ν_3 (713 cm^{-1}/1436 cm^{-1}), ν_1/ν_3 (1086 cm^{-1}/1436 cm^{-1}) and ν_4/ν_1 (713 cm^{-1}/1086 cm^{-1}), normalized to 100 at 121 µm mode particle size fraction and plotted against particle size.

3.4 Discussion

SEM findings indicate the gradational change in dominance of characteristic shapes and three critical size interval ranges. Namely, coarse rhombic fragment dominated powder (121-59 μm) which undergoes progressive transition to intensely micro-fractured equant-shaped grains (*ca.* 59-42 μm to 19 μm), which are then progressively transformed (≤ 5 μm) to sub-micron shards arranged in ramified aggregates. The progressive loss of planar surfaces accompanying grain size reduction with associated increase in micro-fracturing of particles would collectively serve to increase the overall amount of volume scattering (i.e. energy propagation in the matrix after initial boundary interaction relative to specular reflectance), through progressively increasing numbers of inter-particle multiple and intra-particle (internal) scattering events. Because of the large value of *k* associated with the internal modes (e.g., Lane 1999) energy absorbance by the grains would undergo a concomitant increase. The Raman spectra show an overall increase in intensity with grain size reduction over the *ca.* 121 μm to 42 μm particle size range, consistent with some previous findings on the relationship between constituent particle size in powders and Raman intensity (Pellow-Jarman et al., 1996). A possible explanation for the phenomenon may reside in porosity reduction with progressive closer packing of finer grained particles, serving to enhance the intensity of the Raman signal.

Figure 3.8 shows the [ν_4/ν_3] ratio acquired by ATR-IR plotted against the corresponding ratio acquired by Raman. Both sets of data are normalized to 100 % with respect to the 121 μm grain size fraction. The disposition of the data is divisible into three sections, marked intervals A (121-59 μm), B (59-5 μm) and C (5-3 μm) respectively. The IR and Raman results qualitatively correlate with the morphological sub-divisions defined by SEM. The values of normalized change in the [ν_4/ν_3] ratios divided by change in particle size was used to calculate rates of incline and decline for the Raman and ATR-IR [ν_4/ν_3]. During interval A the Raman and ATR-IR [ν_4/ν_3] ratios increase relative to the said ratio for the 121 μm grain size fraction. The incline is 0.23 and 0.09 for RS and ATR-IR respectively. Interval B shows rates of decline of 0.21 (RS) and 0.86 (ATR-IR). Interval C shows rates of decline of 5.57 and 2.87 for RS and ATR-IR respectively (Table 3.2).

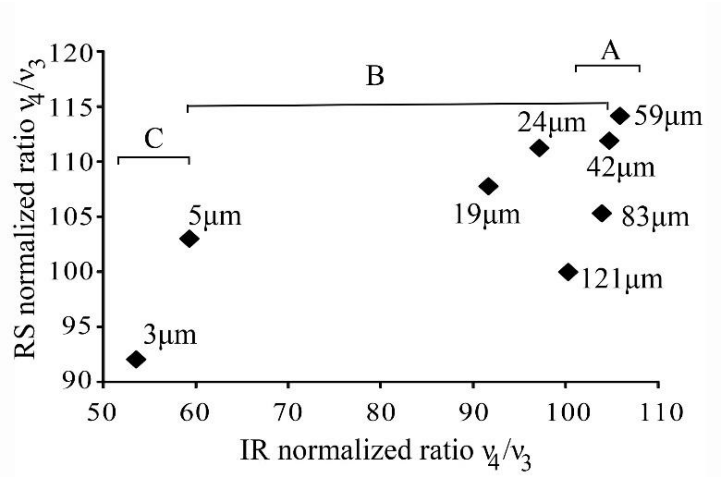

Figure 3.8: Ratios ν_4/ν_3 yielded from IR-ATR (712 cm^{-1}/1393 cm^{-1}) plotted against ratios of RS (713 cm^{-1}/1436 cm^{-1}).

interval	size [µm]	size change [µm]	IR (%) ν_4/ν_3	IR change	IR rate	RS (%) ν_4/ν_3	RS change	RS rate
A1	121		100.00			100.00		
A2	83	38.00	103.63	-3.63	-0.10	105.42	-5.42	-0.14
A3	59	24.00	105.58	-1.95	-0.08	114.40	-8.98	-0.37
total (A1- A3)		62.00		-5.58	-0.09		-14.40	-0.23
B1	59		105.58			114.40		
B2	42	17.00	104.43	1.15	0.07	112.11	2.29	0.13
B3	24	18.00	96.89	7.54	0.42	111.44	0.67	0.04
B4	19	5.00	91.40	5.49	1.10	107.91	3.52	0.70
B5	5	14.00	59.15	45.28	3.23	103.07	4.84	0.35
total (B1-B5)		54.00		46.43	0.86		11.33	0.21
C1	5		59.15			103.07		
C2	3	2.00	53.42	5.74	2.87	91.94	11.13	5.57
total (C1-C2)		2.00		5.74	2.87		11.13	5.57

Table 3.2: Comparison of IR and Raman rates in intervals A, B and C (see Figure 3.8).

ATR-IR and Raman show that the 121 µm-normalised [ν_4/ν_3] ratio increases in the 121-59 µm particle size range with decreasing particle size (Figure 3.8). The ν_4 band possesses a lower absorption coefficient than ν_3 because the value of k is smaller and because ν_4 is located at a higher wavelength value (lower wavenumber) than ν_3 (Lane 1999). Consequently the observed change in the 121 µm-normalised [ν_4/ν_3] ratio may arise because ν_4 would preferentially increase relative to ν_3 because of greater internal scattering (and therefore absorption) of ν_4 relative to ν_3 accompanying particle size reduction within interval A. Accepting this it follows that the RS data which shows a

similar 121 μm-normalised [ν_4/ν_3] trend in the 121-59 μm size interval to ATR-IR (Figure 3.8) may similarly arise from greater internal scattering of ν_4 relative to ν_3 accompanying particle size reduction within interval A. As for any given fixed particle size the relative contribution of the specular and diffuse components to spectral contrast is singular to the specific internal mode. It is also apparent that the rate of change of the 121 μm-normalised [ν_4/ν_3] ratio is discernibly more marked in Raman data than corresponding ATR-IR data (Figure 3.8). One possible reason for this disparity relates to experimental conditions. Specifically the porosity in an ATR-IR analysis can be expected to be significantly lower than in the corresponding Raman analysis because the former technique requires the application of a greater contact pressure upon the powder during data acquisition.

ATR-IR and RS data indicate that the 121 μm-normalised [ν_4/ν_3] ratios undergo pronounced reduction which commences in the 59-42 μm region through to the 5 μm size fraction (Figure 3.8). It is of note that infrared (thermal) emissivity studies of calcite powders identify the optically thick-thin transition as residing in the *ca.* 63 μm (and smaller) particle size fraction (Lane 1999). Hence ATR-IR and Raman data appear to register the same phenomenon. In other words the turn-around in the 121 μm-normalised [ν_4/ν_3] ratio within domain B registers the abrupt transition from the dominance of surface to volume scattering by the ν_3 internal mode, registered in the 121 μm-normalised [ν_4/ν_3] ratio at some value between 59 μm and 42 μm. The 121 μm-normalised [ν_4/ν_3] ratio thereafter declines with decreasing grain size. It is evident that ATR-IR data shows a markedly higher rate of decline in interval B (59-5 μm) than corresponding Raman data (Table 3.2). One possible explanation is a preferential decrease in the dipole moment relative to the polarizability of the molecule.

Raman intensity decreases steeply in powders less than 24 μm particle size (Figure 3.7a). Associated with this the Raman [ν_4/ν_3] [ν_1/ν_3] [ν_4/ν_1] (Figure 3.7a) and ATR-IR [ν_4/ν_2] [ν_2/ν_3] and [ν_4/ν_3] ratios decrease in a systematic manner (Figure 3.6). Equations 3.1 and 3.2 indicate a relationship between particle size and wavelength. Mineral particles may become optically thin when the particle size is equal or smaller than the measured wavelength (Salisbury et al., 1987). The wavelength of the internal modes equate to particle sizes: the asymmetric stretch ν_3 (7 μm), symmetric stretch ν_1 (9 μm), bending modes ν_2 (11 μm) and ν_4 (14 μm). The values are intermediate between the 19 μm and 5 μm modal fraction powders indicating that growing proportions of each powder fraction

from 19μm to 5μm to 3μm contain an increasing population of particles which are optically thin with respect to one or more internal modes. A large majority of the 3 μm mode powder fraction is optically thin with respect to all internal modes (Figure 3.2). It is generally accepted that the spectral contrast of internal modes decrease as particle size decreases and that when separated by more than a wavelength particles behave as optically thin incoherent volume-scatterers. Conversely when packed closely together they scatter coherently as if optically thick surface scattering particles (Salisbury and Wald 1992). Hence the progressive degradation of the overall intensity of contrast of all spectral features at <24 μm is assigned to increasing volume scattering, the growing proportion of optically thin constituents to the population and, their immediate packing arrangement. Differences in internal mode ratios accompanying this transition remain fixed because relative spectral contrast is singular to the specific internal mode.

3.5 Conclusions

Raman and ATR-infrared results show systematic changes in internal mode behaviour as expressed by ratios within the size range 121-3 μm mode range. In particular the [v_4/v_3] ratio (for which both internal modes are Raman and infrared active) is interpreted to undergo an abrupt transition (between 59 and 42 μm size fractions) from specular to coherent diffuse scattering, coincident with loss of crystallographic habit accompanying progressive grain refinement. The v_4 mode is interpreted to be strongly volume diffusive across the range of experimental particle sizes examined. Coherent volume scattering is progressively accompanied by incoherent scattering from 19 μm through to 3 μm modal particle size powders resulting in weakening of spectral contrast. The later samples show abundant agglomerates of sub-micron sized particles. The associated trends in internal mode ratios are assigned to progressively increasing proportions of finer grained fractions crossing of the optical thick-thin transition.

4 Carbonate mineral paragenesis and reaction kinetics in the system MgO-CaO-CO_2-H_2O in presence of chloride or nitrate ions at near surface ambient temperatures.

4.1 Introduction

Investigation of the CaO-MgO-CO_2-H_2O system at ambient temperatures is important for a greater understanding of mineral paragenesis in near-surface conditions and is also a necessary precursor to the aim of storing carbon dioxide in carbonate mineral assemblages (e.g., Cipolli et al., 2004; Orlando et al., 2012; Ballirano et al., 2013). Magnesite [$MgCO_3$] and dolomite [$CaMg(CO_3)_2$] are the most stable magnesium-bearing carbonates under Earth surface conditions. However, it is well documented that in near surface settings carbonate mineral assemblages do not conform to those predicted by equilibrium thermodynamics (e.g., Kazakov et al., 1959; Davies and Bubela 1973; Morse and Casey 1988). Instead, a variety of partially characterized temperature sensitive basic and hydrated magnesium carbonates exist, which in at least some experimental settings appear to be the product of parallel reaction pathways (e.g., Hopkinson et al., 2012). In association with these phases other studies show that the presence of magnesium in solution may suppress calcite formation, facilitate aragonite precipitation (e.g., Park et al., 2008; Hu et al., 2009), lead to huntite [$Mg_3Ca(CO_3)_4$] and/or magnesian calcite formation (e.g., Bishoff 1985; Hopkinson et al., 2008), or give rise to other unstable species such as monohydrocalcite [$CaCO_3 \cdot H_2O$] (Nishiyama et al., 2013). Hence comparatively little is known of the parameters that control the nature of the relationships between calcium and magnesium metastable reaction products, although it seems likely that variation in the [$Mg^{2+}_{(aq)}$: $Ca^{2+}_{(aq)}$] ratio and seeding solutions with carbonate minerals are two parameters likely to exert strong control on mineral paragenesis.

In laboratory experiments calcium and magnesium carbonate minerals are generally synthesised by either mixing solutions of the relevant salt(s) with a solution containing a carbonate or bicarbonate salt (e.g., Hales et al., 2008) or by sparging CO_2 gas through solutions of various salts. The latter method is often accompanied by CO_2 degassing induced by either increasing temperature and/or sonication (e.g. Hopkinson et al., 2012). Various combinations of the methods described above also exist including pH adjustments of the solutions (e.g., Ferrini et al., 2009; Ballirano et al., 2010). Salts

commonly employed include chloride, nitrate and hydroxides. However there does not seem to be any preference for specific starting materials other than the investigation of magnesium chloride in relation to the sequestration of CO_2 in carbonates in saline waters (De Vito et al., 2012). Hence the very nature of the synthesis method may have a bearing on reaction pathways. This study examines carbonate mineral paragenesis by CO_2 sparging and the progress of reaction pathways as a function of time and as a function of the [$Mg^{2+}_{(aq)}$: $Ca^{2+}_{(aq)}$] ratio, aqueous solution seeding with hydromagnesite and, the comparative effect of employing chloride and nitrate salts on mineral paragenesis.

4.2 Methodology

The general experimental procedure involved dispersing powdered $Mg(OH)_2$ (Fluka Analytical, lot. 1442098V) and $CaCl_2.2H_2O$ (Fisher Scientific, lot. 1144526) or calcium nitrate (BDH, lot. 5789920B) in deionized water (300 ml), stirring for 5 minutes and sparging with CO_2 at 150 ml/minute for 4 hours at 25 °C. The pH values were measured intermittently using a Mettler Toledo, MP220 pH meter (±0.01 pH) calibrated against pH 10 (borate), pH 7 (phosphate) and pH 4 (phthalate) NIST-traceable buffers (Fisher Scientific). All starting suspensions had an initial pH *ca.* 10.3. Subsequent to CO_2 sparging the pH stabilised at pH 7. Slurries were then transferred into a shaking water bath, speed 100 rpm (VWR, Clifton) and held at 35 °C for up to 30 days. Slurries were covered with pierced parafilm to avoid evaporation and to allow exchange of gases. Temperature was measured with a Fisher Scientific platinum sensor (Pt-100Ω) thermometer (±0.1°C).

Experiments [A] and [B] employed [$Mg^{2+}_{(aq)}$:$Ca^{2+}_{(aq)}$] ratios of 5:1 and 10:1 respectively. Reaction [S] employed the same [$Mg^{2+}_{(aq)}$:$Ca^{2+}_{(aq)}$] ratio as [A] but was seeded with 0.002 mol of heavy hydromagnesite [$Mg_5(CO_3)_4(OH)_2 \cdot 5H_2O$] (Fisher Scientific, lot. 1164012) in place of 0.01 mol of $Mg(OH)_2$. Experiment [N] employed the same protocol as experiment [A] but with calcium chloride replaced by a molar equivalent of calcium nitrate (Table 4.1). For each experimental set, nine initial preparations were started; each of these nine reactions were arrested sequentially after increasingly longer periods of time, in order to characterize the solid phases and their amounts produced as a function of time. Precipitates recovered by vacuum filtration were dried at room temperature for 48 hours without washing, in an effort to maintain representative concentrations of any

high solubility mineral phases. All samples were dried under identical conditions. The dried samples were lightly ground in an agate mortar prior to analyses. Samples were coded with a letter denoting experiment type and a number indicating experimental duration (in days). Zero days duration refers to samples collected immediately after sparging.

Reaction name	Magnesium salt(s)	Calcium salt	Ratio of Mg:Ca
A	0.1 mol (5.83 grams) magnesium hydroxide [$Mg(OH)_2$]	0.02 mol (2.94 grams) calcium chloride [$CaCl_2.2H_2O$]	5:1
B	0.1 mol (5.83 grams) magnesium hydroxide [$Mg(OH)_2$]	0.01mol (1.47 grams) calcium chloride as [$CaCl_2.2H_2O$]	10:1
S	0.09 mol (5.22 grams) magnesium hydroxide [$Mg(OH)_2$] and 0.002 mol (0.93 grams) magnesium carbonate heavy [$Mg_5(CO_3)_4(OH)_2.xH_2O$]	0.02 mol (2.94 grams) calcium chloride [$CaCl_2.2H_2O$]	5:1
N	0.1 mol (5.83grams) magnesium hydroxide [$Mg(OH)_2$]	0.02 mol calcium nitrate [$Ca(NO_3)_2$] (3.30 grams)	5:1

Table 4.1: Summary of reactants used in experiments.

Precipitates were characterized by Raman and mid-infrared spectroscopy, both conducted at the University of Brighton (U. K.). X-ray powder diffraction (XRD) was performed at the Natural History Museum, London (U. K.). Eight selected samples were also analysed under scanning electron microscope (SEM) and elemental analysis performed by electron probe micro-analyser (EPMA). All analyses were conducted at 25 °C and at atmospheric pressure. Raman analyses were conducted using a Perkin Elmer Raman Identicheck fitted with a 785 nm laser, a CCD detector and a fibre optic probe with 70 mV laser power. The fibre optic probe has a 100 µm spot size at a working distance of 7.5 mm. The samples were measured in the spectral range 2000-150 cm^{-1} at a resolution of 2 cm^{-1}. Each spectrum was collected from 8 scans for 2 seconds and repeated six times on different randomly selected subsamples to assure representative spectral information. The Raman spectra obtained were averaged and baseline corrected; the limit of detection is *ca.* 2 w/w % or better (Kristova et al., 2013). Data manipulation was performed using the software

Spectrum (Perkin Elmer) and PeakFit (Jandel, Scientific Software). Mid-infrared spectroscopic measurements were collected on a Perkin Elmer Spectrum 65 spectrometer fitted with an attenuated total reflection accessory. The samples were measured in the spectral range 4000-600 cm^{-1} at a resolution of 4 cm^{-1}. Each spectrum was collected from 16 scans at 25 °C.

X-ray powder diffraction (XRD) data were collected using a Nonius PDS120 Powder Diffraction System with an INEL curved position sensitive detector. This detector has an output array of 4096 digital channels representing an arc of 120° 2θ and permits the simultaneous measurement of diffracted X-ray intensities at all angles of 2θ across 120° with a static beam-sample-detector geometry. Copper (or, in a parallel set of experiments, cobalt) $K\alpha_1$ radiation was selected from the line focus of the primary beam using a germanium 111 single-crystal monochromator and a post-monochromator horizontal slit. Horizontal and vertical slits were used to restrict the beam to 0.24 by 5.0 mm (or, for Co radiation, 0.14 by 5.0 mm) respectively. Thin-smear powdered samples were mounted on a single-crystal quartz substrate, and measurements made in reflection geometry with the sample surface (spinning in its own plane) at an angle of ~2° to the incident beam. Data collection times were 30 minutes for each sample. NIST Silicon powder SRM640 and silver behenate were used as external 2θ calibration standards and the 2θ linearization of the detector was performed using a least-squares cubic spline function. Mineral phase identification was undertaken by search-match procedures using the PDF-2 database supplied by the International Centre for Diffraction Data (ICDD). The detection limit for mineral phase(s) in mixed assemblages of basic and hydrate magnesium carbonates is *ca.* 5 % modal abundance.

Particle size and shape of powdered aggregates were monitored by SEM utilizing secondary scattering technique. The scanning electron microscope (Carl Zeiss, EVO LS15) was employed to investigate samples mounted on specimen stubs and coated with 4 nm platinum (Quorum Q150T ES sputter coater).

4.3 Results

Figure 4.1 shows representative Raman spectra (further spectra are shown in Appendix, Figure C.1 and C.2). Figure 4.2 summarises the variation of pH and v_1 Raman intensity for the major common phases nesquehonite, dypingite-type [$Mg_5(CO_3)_4(OH)_2 \cdot xH_2O$] and calcium carbonates for each experiment plotted against reaction time. The relative abundance of $CaCO_3$ polymorphs was constrained as the ratio of vaterite (v_4 753 cm^{-1}) to calcite (v_4 713 cm^{-1}) to aragonite (lattice mode 208 cm^{-1}) by peak height. Figure 4.3 illustrates the typical FT-IR and Raman spectra (showing detail of v_1 area). Spectral signatures for majority of Mg and Ca carbonate minerals are well documented e.g. by White (1974), Edwards et al. (2005) and Frost et al. (2009). Mid-infrared data indicate evidence of (OH) groups in samples devoid of evidence for $Mg_5(CO_3)_4(OH)_2 \cdot xH_2O$ suggesting that $Mg(HCO_3,OH) \cdot 2H_2O$ is present in abundance relative to, or possibly to the exclusion of, $Mg(CO_3) \cdot 3H_2O$ in those samples analyzed. A representative IR spectrum is shown in Figure 4.3a, together with examples of curve-fitted Raman spectra in the carbonate v_1 region from four selected samples (Figure 4.3b-e). Further examples of IR spectra are shown in Appendix C, Figures C.3-C.6, additional curve-fitted Raman spectra are shown in Appendix C, Figure C.7. The following section examines these plots in detail, for each experimental time series, with mineral identification confirmed by XRD (Figure 4.4).

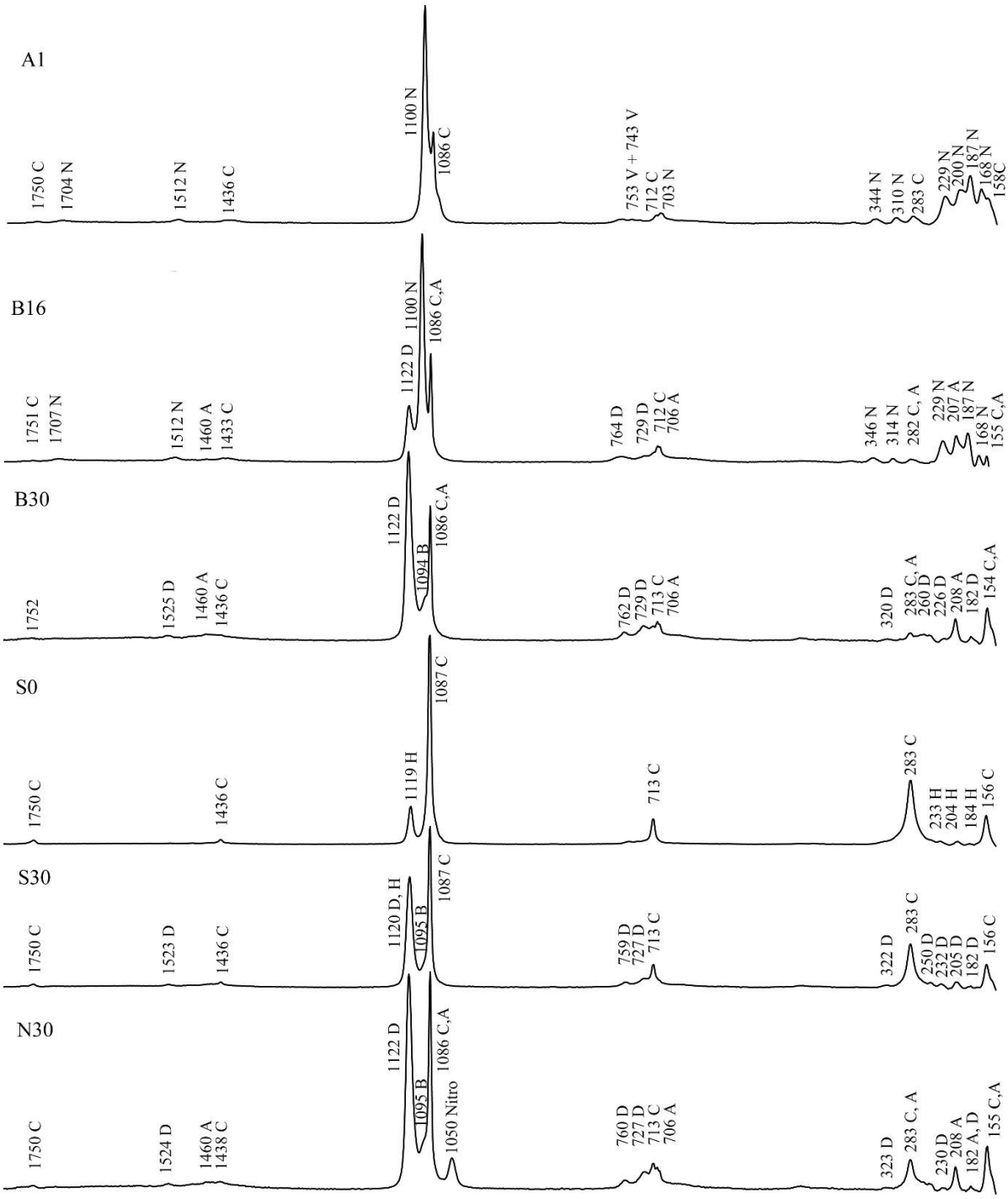

Figure 4.1: Representative Raman spectra in the range 1800-150 cm^{-1}. Coding of mineral phases is as follows –A (aragonite), B (barringtonite), C (calcite), D (dypingite), H (hydromagnesite), N (nesquehonite), Nitro (magnesium nitrate hexahydrate), V (vaterite).

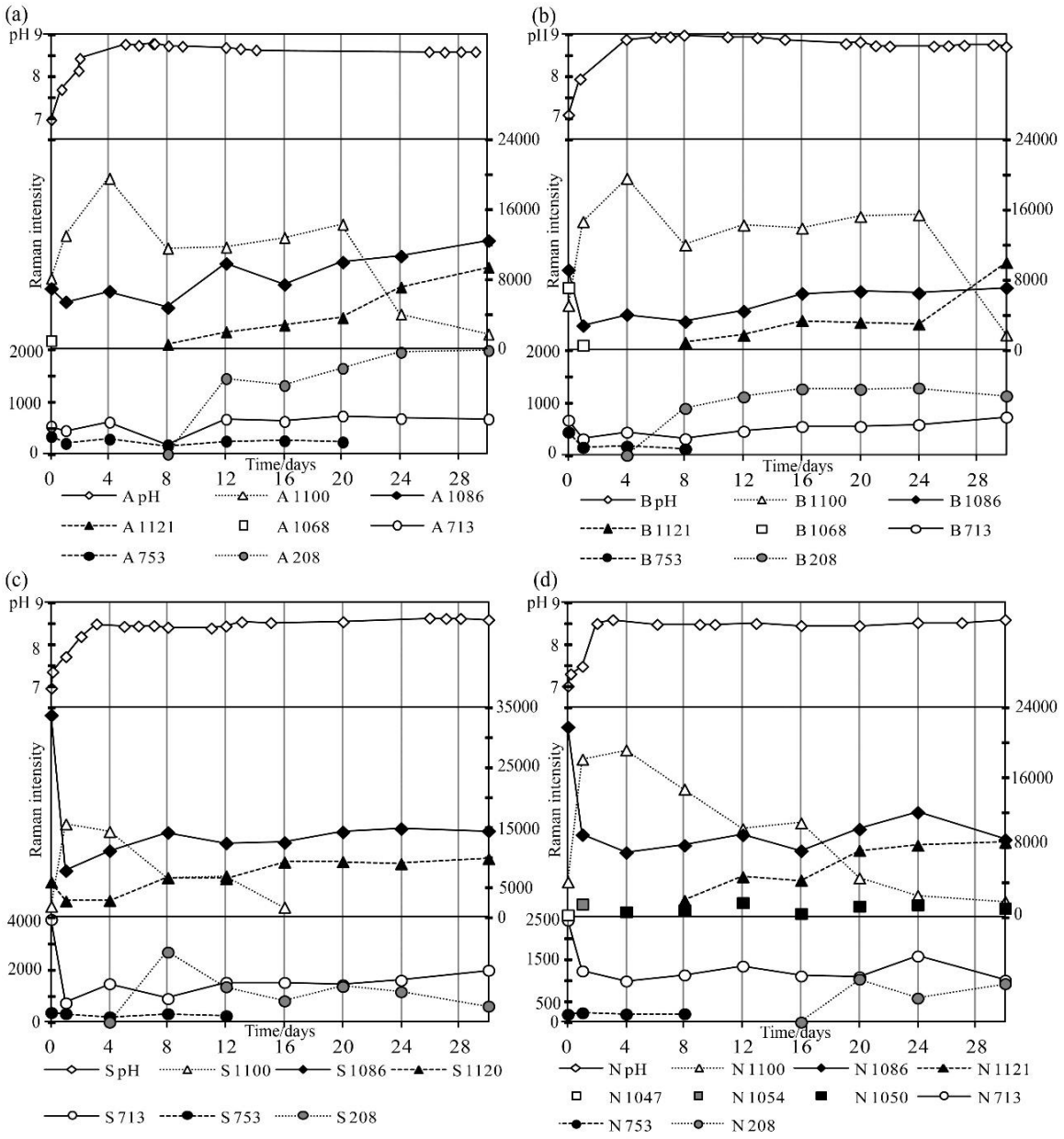

Figure 4.2: Experimental results plotted against time (in days) for: a) Experiment [A], b) Experiment [B], c) Experiment [S], d) Experiment [N] where each shows pH measurements (top), Raman semi-quantitative measurements of ν_1 peaks for main mineral phases plotted in absolute values (middle) and Raman semi-quantitative measurements of calcium carbonate phases in absolute values (bottom).

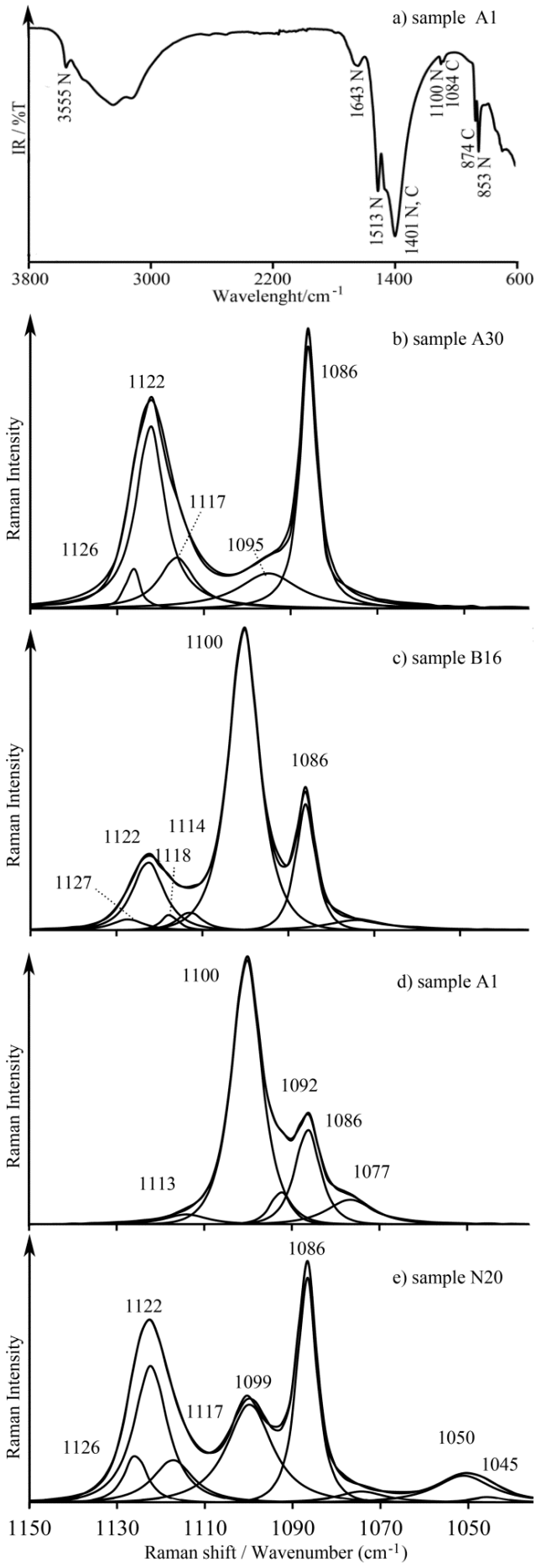

Figure 4.3: Representative (a) FT-IR and (b-e) Raman spectra showing detail of curve fitting in the range 1150-1030 cm^{-1}. a) FT-IR spectrum of A1 sample containing nesquehonite with OH band at 3555 cm^{-1}. N denotes nesquehonite, C denotes calcium carbonate. Vaterite could not be distinguished by IR due to its low concentration and spectral overlap with calcite peaks. Raman spectra for samples b) A30, c) B16, d) A1 and e) N20.

4.3.1 Experiment [A]

Raman and XRD show that Mg-calcite (v_1 1088 cm^{-1}) with subordinate vaterite (v_1 1077 cm^{-1}) were the dominant [$CaCO_3$] polymorphs until (A12), and thereafter aragonite is the main $CaCO_3$ phase produced (Figure 4.1, 4.2a, Appendix Figure C.1 and C.2). Sample (A0) shows a shoulder on the (v_1 1088 cm^{-1}) internal mode at 1069 cm^{-1} consistent with short lived traces of $CaCO_3 \cdot H_2O$ in the system. Evidence for traces of vaterite persists until (A20).

The v_1 band of nesquehonite [$MgCO_3 \cdot 3H_2O$] or [$Mg(HCO_3,OH) \cdot 2H_20$] situated at 1100 cm^{-1} attains maximum intensity in (A4), decreasing and then stabilizing (or marginally increasing) in intensity (A8 - A20) and thereafter rapidly diminishing in intensity (Figure 4.1 and 4.2). From (A8) onwards a band at 1122 cm^{-1} appears and progressively grows in intensity with increasing experimental duration. The band is assigned to dypingite-type [$Mg_5(CO_3)_4(OH)_2 \cdot xH_2O$] phase(s). XRD identified that dypingite [$Mg_5(CO_3)_4(OH)_2 \cdot 8H_2O$] forms first (A4 - A8) with both forms [$Mg_5(CO_3)_4(OH)_2 \cdot 8H_2O$] and [$Mg_5(CO_3)_4(OH)_2 \cdot 5H_2O$] present thereafter.

Analysis of the broad spectral feature at *ca.* 1122 cm^{-1} with a Gaussian Lorentzian function suggests that it consists of four overlapping peaks: the most intense at 1122 cm^{-1}, two weak peaks at 1117 cm^{-1} and 1126 cm^{-1} (Figure 4.3), all of which increase in intensity with increasing experimental duration, plus a poorly resolved very weak band at *ca.* 1114 cm^{-1}.

The position of the high intensity band at 1122 cm^{-1} closely coincides with the reported v_1 [CO_3^{2-}] internal mode for dypingite *ca.* 1120 cm^{-1} (Frost et al., 2009). The origins of the 1117 cm^{-1} and 1126-1127 cm^{-1} bands are uncertain and do not serve to discriminate the eight from five waters of crystallization in $Mg_5(CO_3)_4(OH)_2 \cdot xH_2O$ phases. Previous studies have shown that $Mg_5(CO_3)_4(OH)_2 \cdot xH_2O$ phases show distinct unit cell parameters yet retain essentially uniform short-range order of the CO_3^{2-} anion (Hopkinson et al., 2012). However, studies also indicate that dypingites have variable structural H_2O content and their CO_3^{2-} units are variably distorted (Frost et al., 2009). Further, the 1117 cm^{-1} band closely coincides with the reported v_1 vibration of hydromagnesite at 1116-1119 cm^{-1} (e.g., Edwards et al., 2005; Martinez-Arkanzo et al., 2007) whilst doubling of

v_1 components in the range 1110 cm^{-1} and 1120 cm^{-1} has been assigned to distinct CO_3^{2-} ions in the structure of hydromagnesite (White 1974). Hence, it is possible that doubling of v_1 components in the $Mg_5(CO_3)_4(OH)_2 \cdot xH_2O$ phases reported here extends to higher frequencies than that reported for hydromagnesite. XRD analysis indicates the presence of small quantities of chlorartinite [$Mg_2(CO_3)Cl(OH) \cdot 3H_2O$] in (A0) through to (A24) (Figure 4.4). Raman identification of the mineral phase is complicated by the closely spaced overlapping spectral features in the 1122 cm^{-1} region. However, the main Raman active v_1 internal mode for chlorartinite is reported at 1114 cm^{-1} (RRUFF database). Hence, the very low intensity feature at 1114 cm^{-1} resolved by peak fit software is assigned to chlorartinite.

After 30 days reaction the (A30) diffraction pattern indicates that traces of barringtonite [$MgCO_3 \cdot 2H_2O$] may also be present (d=8.75 Å, Cu=10.1° 2Θ, Co=11.7° 2Θ), a phase for which no Raman spectrum exists. However, the Raman spectra reported here do show a low intensity feature at *ca.* 1094-1095 cm^{-1}. Several carbonate minerals show a strong Raman peak in this area e.g. magnesite, artinite, vaterite and an unnamed hydrous Ca-bearing magnesium carbonate (HCMC) (Queralt et al., 1997; Edwards et al., 2005). However, none of them were identified by XRD. Hence available evidence suggests that barringtonite, or a barringtonite-like magnesium hydrate carbonate, is characterized by a high intensity band at 1094-1095 cm^{-1} and is associated with the decomposition of nesquehonite alongside the generation of volumetrically abundant $Mg_5(CO_3)_4(OH)_2 \cdot xH_2O$ phases.

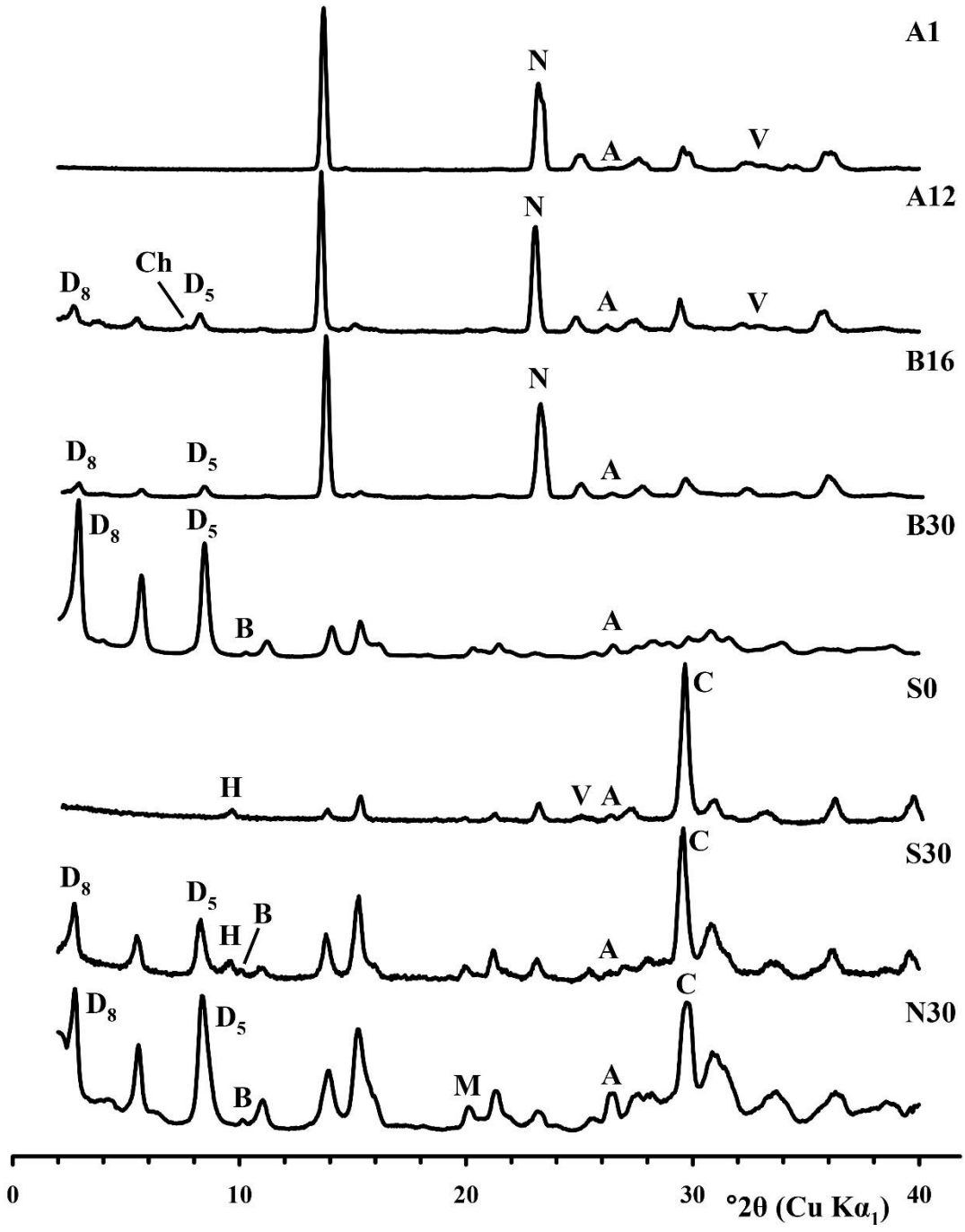

Figure 4.4: Representative X-ray diffraction patterns. Coding of mineral phases is as follows –A (aragonite), B (barringtonite), C (calcite), Ch (chlorartinite), D_5 (dypingite $Mg_5(CO_3)_4(OH)_2 \cdot 5H_2O$), D_8 (dypingite $Mg_5(CO_3)_4(OH)_2 \cdot 8H_2O$), H (hydromagnesite), N (nesquehonite), M (magnesium nitrate hexahydrate), V (vaterite).

4.3.2 Experiment [B]

Sample (B0) shows a predominant peak at 1087 cm^{-1} assigned to $CaCO_3$ polymorphs, a subordinate peak at 1068 cm^{-1} assigned to monohydrocalcite [$CaCO_3 \cdot H_2O$] and a low intensity peak at 1100 cm^{-1} assigned to nesquehonite (Figure 4.2b). XRD and Raman spectroscopy indicate that aragonite is the dominant $CaCO_3$ polymorph although calcite/magnesian calcite grows from day 8 onwards. XRD indicates that traces of chlorartinite [$Mg_2(CO_3)Cl(OH) \cdot 3H_2O$] are present in samples (B0) through to (B20). In common with experiment [A] the 1100 cm^{-1} peak (assigned to nesquehonite) attains its maximum intensity in sample (B4) and then diminishes, coincident with emergence of $Mg_5(CO_3)_4(OH)_2 \cdot xH_2O$ phase(s). In the (B8-B30) time frame XRD indicates that $Mg_5(CO_3)_4(OH)_2 \cdot 8H_2O$ forms first, and is later accompanied by $Mg_5(CO_3)_4(OH)_2 \cdot 5H_2O$. Again analysis of the broad spectral feature at *ca.* 1122 cm^{-1} using a Gaussian Lorentzian function shows that the feature consists of four overlapping peaks: 1122 cm^{-1} (highest intensity) followed by 1117 cm^{-1}, 1126 cm^{-1} and a very weak band at 1114 cm^{-1} (assigned to chlorartinite). Both XRD and Raman also show evidence for $MgCO_3 \cdot 2H_2O$ in the final stages of the experiment (Figures 4.1 and 4.4). These results differ from experiment [A] in three respects. Namely, the abrupt reduction in nesquehonite content towards the end of the experiment commences four days later than in experiment [A], vaterite is not resolved beyond (B8) (compared to (A20)) and monohydrocalcite [$CaCO_3 \cdot H_2O$] is identified in the (B1) sample indicating that it can persist beyond the sparging stage in the experiment [B] regime. Monohydrocalcite is metastable with respect to calcite and aragonite (e.g., Taylor 1975; Kamiya et al., 1977; Munemoto and Fukushi 2008) and readily transforms into either $CaCO_3$ polymorph (Kamiya et al., 1977; Loste et al., 2003).

4.3.3 Experiment [S]

Solids collected after sparging (S0) consisted of calcite (v_1 1088 cm^{-1}), seeded hydromagnesite (v_1 1119 cm^{-1}) and traces of vaterite (v_4 753 cm^{-1}) (Figure 4.1 and 4.2c). Aragonite appears after four days, peaks in concentration in (S8) and thereafter its presence gradually decreases. Vaterite is lost from the system after (S12), whereas calcite (v_4 713 cm^{-1}) marginally increases in concentration throughout. XRD showed that all samples contain hydromagnesite [$Mg_5(CO_3)_4(OH)_2 \cdot 4H_2O$], however, (S0) contains the

least amount. Nesquehonite appears in (S1) and attains a maximum concentration in (S4); it is not resolved beyond (S16). Peak fitting of the Raman spectrum of (S4) in the carbonate v_1 region indicates that nesquehonite formation is followed by the emergence of a weak band at 1125 cm^{-1}, consistent with traces of $Mg_5(CO_3)_4(OH)_2 \cdot xH_2O$ phases. With increasing experimental duration this peak attains parity in intensity (S8-S12) with the v_1 internal mode of nesquehonite, while the hydromagnesite v_1 peak shifts to 1120 cm^{-1}. Between (S16 - S30) the multicomponent $Mg_5(CO_3)_4(OH)_2 \cdot xH_2O$ peak in the v_1 region shows maximum intensity. XRD shows close agreement with Raman findings and indicates traces of barringtonite or a barringtonite-like phase develop at the end of the experiment (S30) (Figure 4.4).

4.3.4 Experiment [N]

Calcite is the dominant $CaCO_3$ polymorph from the outset with aragonite forming between (N16–N30) and traces of a vaterite-like phase present until (N8) (Figure 4.2d). Nesquehonite precipitation occurs in (N1–N4) with later concentrations diminishing, to trace levels by (N30), coincident with a progressive rise in $Mg_5(CO_3)_4(OH)_2 \cdot xH_2O$ content. Specific to experiment [N] is the appearance of Raman active bands at 1047 cm^{-1}, 1054 cm^{-1} and 1050 cm^{-1} (Figure 4.1 and 4.3e). The precise origins of these bands are uncertain although nitrocalcite [$Ca(NO_3)_2 \cdot 4H_2O$)] and nitromagnesite [$Mg(NO_3)_2 \cdot 6H_2O$] have previously been reported with high intensity peaks at 1048 cm^{-1} and 1058 cm^{-1} respectively (Martinez-Arkarazo et al., 2007). Similar Raman bands have also been observed for nitrate adsorption on hydroxide compounds (hydrotalcite) and were assigned to both the non-hydrogen bonded, and the hydrogen bonded, symmetrical stretch of NO_3^- at 1045 $cm^{-1}$and 1050 cm^{-1} respectively (Frost et al., 2005; Frost and Musumeci 2006). Hence, the Raman bands identified in experiment [N] are assigned to nitrate related compounds. XRD detected the presence of magnesium nitrate hexahydrate [$Mg(NO_3)_2 \cdot 6H_2O$] in samples (N16) onwards (Figure 4.4). This may suggest that nitrate-assigned Raman active bands in samples prior to day 16 are caused by product phases either as dispersed inclusions, between structural layers, and/or as a discrete X-ray amorphous phase(s). In common to all experiments sample (N30) shows a low intensity peak at *ca.* 1095 cm^{-1} which is progressively resolved as the concentration of

nesquehonite diminishes. This band is tentatively assigned to barringtonite [$MgCO_3 \cdot 2H_2O$].

4.3.5 SEM

Eight samples were observed under SEM and elemental analysis was performed. Sample B0 showed spherical clusters *ca*. 2-4 μm diameter. These are most likely magnesian calcite with nesquehonite needles growing on their surface after dehydration of MHC (Figure 4.5a). Sample S0 displayed rhombic structures 2-4 μm long (Figure 4.5b). Samples A1 is dominated by nesquehonite needles, up to 100 μm longest dimension with acicular aggregates projecting from their surface (Figure 4.5c). Sample A20 consists of nesquehonite crystals in association with agglomerates of platy dypingite crystals (Figure 5d). Sample A30 (Figure 4.5e) consists of dypingite platy agglomerates resembling the 'deck of cards' textures described by Zhang et al., (2006) and some calcium carbonate crystals.

According to XRD and RS the dominant calcium carbonate in the experiment [A] at time 30 days is aragonite. The SEM-EPMA results show that the samples contain both magnesium and calcium (Figure 4.5). Aragonite typically crystallises in a form of needles however no needles were observed in the final sample [A30] and deformed polyhedron structures were observed instead. Needle-like crystal habits that were analysed in other samples collected during the reaction were composed of Mg carbonates with Ca concentrations detected below 1% weight. Therefore it is plausible that aragonite crystallization during the reactions had non-acicular crystal habits. More EPMA data can be found in Appendix C (Figures C.8-C.15, Tables C.1-C.6) although elemental analysis as expected did not yield sufficient data in analysis of e.g. carbon and nitrogen. Elemental analysis has been performed by EPMA (Electron probe micro-analyser) acquiring compositional information by energy-dispersive spectroscopy and wavelength-dispersive spectroscopy. However, analysing carbon by EPMA is difficult for a number of reasons. The carbon x-ray K line is of low energy and is easily absorbed which means that only the carbon x-rays from the surface of the specimen can be counted. Carbon x-rays are also easily absorbed by the x-ray detector windows. Furthermore, there can be a significant carbon background signal (Rolland et al., 2004). All of the above mentioned

reasons make analysis of carbon by SEM-EPMA inaccurate. However the similar problem happens in other x-ray based techniques like x-ray fluorescence (XRF).

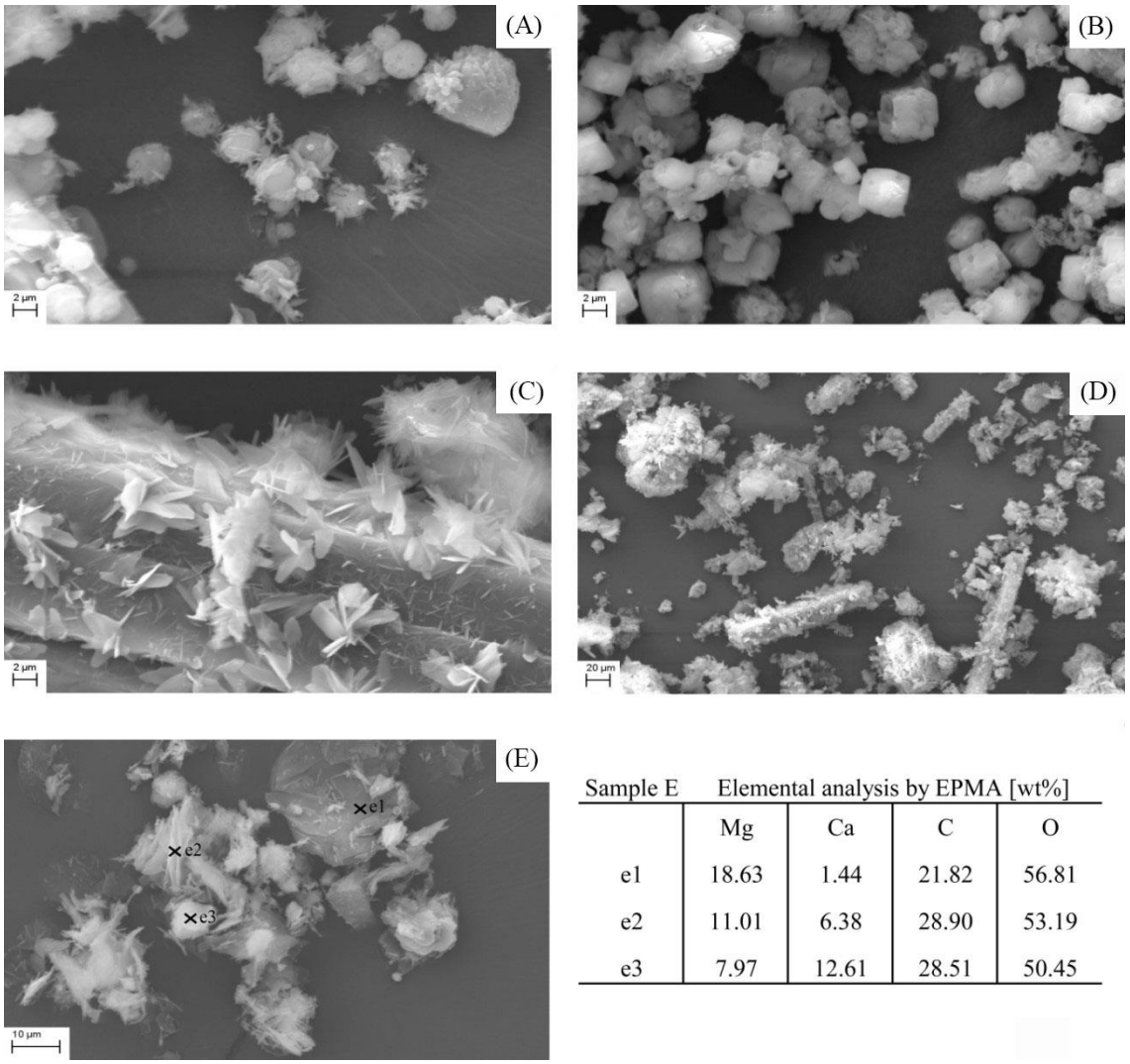

Sample E	Elemental analysis by EPMA [wt%]			
	Mg	Ca	C	O
e1	18.63	1.44	21.82	56.81
e2	11.01	6.38	28.90	53.19
e3	7.97	12.61	28.51	50.45

Figure 4.5: SEM images of experimental precipitates. a) B0 - spherical calcium carbonate clusters with formation of nesquehonite needles; b) S0 - rhombic crystals of calcite with subordinate hydromagnesite agglomerates with no evidence for development of nesquehonite needles on calcite surfaces; c) A1 - overgrowths of nesquehonite needles on large nesquehonite rod-shaped crystal; d) A20 - nesquehonite crystals in association with agglomerates of platy dypingite crystals; e) A30, sites of elemental analysis (by EPMA) are marked by black crosses (e1, e2, e3) and expressed as wt %.

4.4 Discussion

Results suggest that carbonate mineral paragenesis is driven by geochemical feedback between a range of calcium and magnesium carbonate dissolution-precipitation events. Decomposition of nesquehonite [$Mg(HCO_3,OH)\cdot 2H_2O$] leads to formation of magnesium carbonate hydrates [$Mg_5(CO_3)_4(OH)_2.xH_2O$] where these hydrated phases contain 8 and/or 5 molecules of crystalline water. In addition the mineral phases found during the dissolution-precipitation events included chlorartinite [$Mg_2(CO_3)Cl(OH)\cdot 3H_2O$], barringtonite [$MgCO_3\cdot 2H_2O$], magnesian calcite, monohydrocalcite [$CaCO_3\cdot H_2O$], calcium carbonate polymorphs [$CaCO_3$] (calcite, aragonite, vaterite), and magnesium nitrate hexahydrate [$Mg(NO_3)_2\cdot 6H_2O$]. Seeding of the experiment effectively halved the time it takes for nesquehonite to disappear from the system and stimulates some, although limited, post-sparging hydromagnesite growth. Formation of magnesium nitrate hexahydrate [$Mg(NO_3)_2\cdot 6H_2O$] is exclusive to experiment [N]. The individual mineral phases and their reaction kinetics are discussed in sections below.

4.4.1 Presence of chlorartinite.

Traces of chlorartinite [$Mg_2(CO_3)Cl(OH)\cdot 3H_2O$] were detected by XRD in samples from experiments [A] and [B] over the first 20 days, only. The mineral phase initially occurs in association with $Mg(OH)_2$ and $Mg(HCO_3,OH)\cdot 2H_2O$, indicating that its formation preceded, at least in part, nesquehonite decomposition and the coeval generation of $Mg_5(CO_3)_4(OH)_2\cdot xH_2O$ phases. Chlorartinite and artinite have not been reported as metastable intermediates of the nesquehonite to hydromagnesite transition (e.g., Davies and Bubela 1973). Although little is known about the stability field of chlorartinite, low temperature thermodynamic models indicate that the closely related mineral artinite [$Mg_2(CO_3)(OH)_2\cdot 3H_2O$] occupies a pCO_2 stability field between brucite and nesquehonite (Könisberger et al., 1999) and has been reported with between two to four water molecules (e.g., Beck 1950; Kazakov et al., 1959). More recent experiments involving sparging CO_2 through $MgCl_2\cdot 6H_2O$ aqueous solutions have demonstrated that chlorartinite formation was followed by abundant nesquehonite precipitation (Mignardi

et al., 2011; De Vito et al., 2012). This suggests that chlorartinite is likely to be the first carbonate phase formed in our system, accompanying $Mg(OH)_2$ dissolution.

The transition from chlorartinite and artinite to nesquehonite is only partially documented (Kazakov et al., 1959; De Vito et al., 2012). However, in $MgO\text{-}H_2O\text{-}CO_2$ space chlorartinite falls on a line that connects brucite [$Mg(OH)_2$] with nesquehonite (Figure 4.6). No protohydromagnesite [$Mg_5(CO_3)_4(OH)_2{\cdot}11H_2O$] was identified in the experiments documented here, which may suggest that the direct reaction path to nesquehonite was kinetically favoured over the indirect path *via* protohydromagnesite. The apparent absence of chlorartinite in experiment [S] may suggest that accelerated reaction rates in the seeded environment either make the phase extremely short lived, or the direct path from $Mg(OH)_2$ to nesquehonite is kinetically favoured.

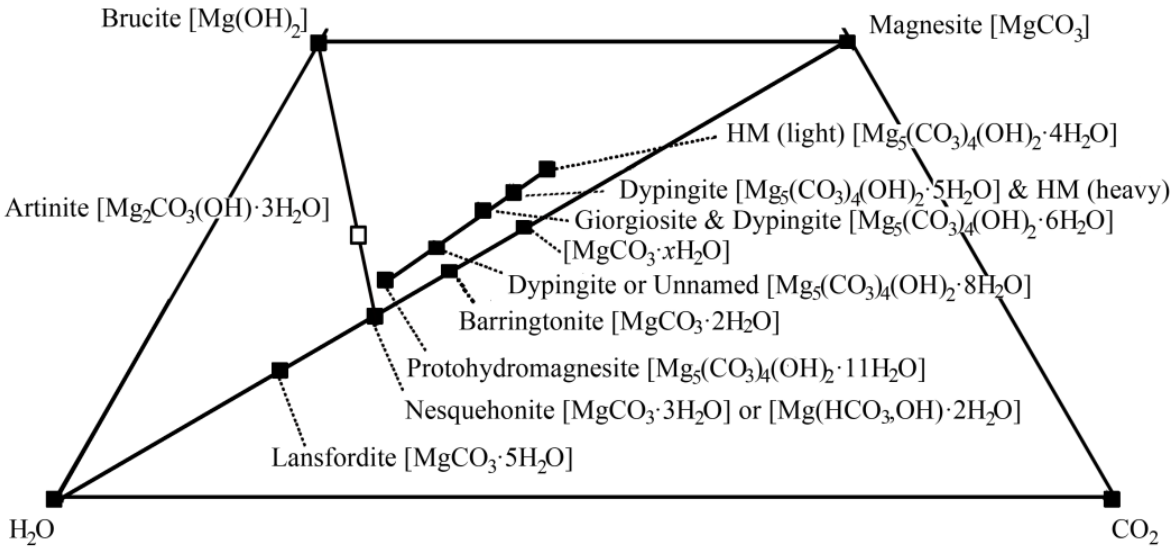

Figure 4.6: The hydrated magnesium carbonate minerals in the system $CO_2\text{-}MgO\text{-}H_2O$, adapted from Canterford et al., (1984) and Hopkinson et al., (2012). A pathway is suggested between brucite, artinite and nesquehonite; see Hopkinson et al., (2012) for further details of mineral names. HM denotes hydromagnesite. Specified values of x in synthesised $MgCO_3{\cdot}xH_2O$ phases include 1.3 and 0.3 H_2O (Zhang et al., 2006). The ternary plot is shown here without its MgO apex.

4.4.2 Hydromagnesite seeding.

Experimental results show that seeding the mother liquor with hydromagnesite effectively halved the time it takes for nesquehonite to disappear from the system, relative to experiments [A] and [B]. Seeding also stimulates post-sparging hydromagnesite growth. Previous studies (e.g., Königsberger et al., 1999; Hopkinson et al., 2012) indicate that in all four experiments the system would have been simultaneously supersaturated with nesquehonite and hydromagnesite, yet formation of hydromagnesite is restricted to experiment [S]. Data also indicates that formation of $Mg_5(CO_3)_4(OH)_2 \cdot xH_2O$ dypingite-type phases (for which no thermodynamic data exists) occurs at the expense of nesquehonite. Combined, this suggests that nucleation of hydromagnesite on existing hydromagnesite seeds is inadequate to ease supersaturation, to the extent that crystallization becomes governed by the disorder of the system (e.g., Goldsmith 1953). Thereby nucleation and growth of nesquehonite occurs in conjunction with hydromagnesite growth.

4.4.3 Presence of barringtonite.

XRD indicates that traces of barringtonite [$MgCO_3 \cdot 2H_2O$] or a barringtonite-like magnesium carbonate hydrate is associated with the decomposition of nesquehonite alongside volumetrically abundant $Mg_5(CO_3)_4(OH)_2 \cdot xH_2O$ phases (with eight and five waters of crystallization) towards the end of all four experiments reported here. Some studies have shown that $MgCO_3 \cdot xH_2O$ phases (where $x \leq 3H_2O$) can be generated during the transformation of nesquehonite to hydromagnesite in an aqueous medium (e.g., Hopkinson et al., 2008). Conversely, other experiments show that the transformation of nesquehonite to hydromagnesite can occur in the absence of resolvable $MgCO_3 \cdot xH_2O$ phases (where $x \leq 3H_2O$). Instead, intermediate $Mg_5(CO_3)_4(OH)_2 \cdot xH_2O$ phases between nesquehonite and hydromagnesite have been reported, which show eleven (Davies and Bubela, 1973) or eight and five waters of crystallization (Hopkinson et al., 2012). It is firmly established that the water content in $MgCO_3 \cdot xH_2O$ phases is strongly affected by synthesis conditions, and that these phases may contain some bicarbonate (Zhang et al., 2006). Furthermore, desiccation of nesquehonite yields $MgCO_3 \cdot H_2O$ (Menzel and Brückner 1930; Dell and Weller 1959) and although the congruency of nesquehonite

dissolution is uncertain, it is possible that dissolution of nesquehonite at least in some settings may involve preferential loss of waters of crystallization and/or breakdown of bicarbonate to yield barringtonite.

$$Mg(HCO_3,OH)\cdot 2H_2O \rightarrow MgCO_3\cdot 2H_2O + H_2O_{(aq)}$$

The potential significance of this proposed reaction, combined with the fact that conditions of synthesis affect the magnesium hydrate water content and the possibility that nesquehonite may undergo incongruent water loss, is that an alternative starting point may be thus generated prior to the parallel reaction pathway (in particular transformation of metastable $Mg_5(CO_3)_4(OH)_2\cdot xH_2O$ phases towards hydromagnesite [$Mg_5(CO_3)_4(OH)_2\cdot 4H_2O$]). Variations in the nature and appearance of the $Mg_5(CO_3)_4(OH)_2\cdot xH_2O$ phases will be governed by the precursor or evolving chemistry of the unstable magnesium hydrate species. This interpretation accounts for the apparent disparities in the numbers and types of mineral phases reported to arise from the nesquehonite to hydromagnesite transition. Accepting this, it also follows that the mineral protohydromagnesite [$Mg_5(CO_3)_4(OH)_2\cdot 11H_2O$] which shows the closest compositional similarity to nesquehonite, reported composition $MgCO_3\cdot 3H_2O$ (Davies and Bubela 1973), may represent the closest approach to congruent dissolution of nesquehonite and thereby the most extended possible parallel reaction pathway of $Mg_5(CO_3)_4(OH)_2\cdot xH_2O$ phases to hydromagnesite. During this study, barringtonite was detected only in end samples from 30 days. The minerals chlorartinite and barringtonite were only found at specific stages in the experiments. Given that the conditions of drying were identical for all experimental samples it seems unlikely that chlorartinite and barringtonite (or barringtonite-like magnesium hydrate carbonate) would be secondary phases drying related in origin.

4.4.4 Behaviour of calcium carbonate phases.

Monohydrocalcite [$CaCO_3\cdot H_2O$] is restricted in occurrence to the opening period (*ca.* 1 day) of experiment [B] in which the mineral occurs alongside magnesian calcite, lesser quantities of vaterite and progressively abundant nesquehonite. It has been observed (Nishiyama et al., 2013) that monohydrocalcite formation concurrent with nesquehonite

requires the presence of magnesium in solution and more CO_3^{2-} than $Ca^{2+}_{(aq)}$ because the high hydration energy of magnesium prevents quick $CaCO_3 \cdot H_2O$ dehydration to anhydrous calcium carbonate. Evidently these conditions were temporarily met during the onset of experiment [B]. In this respect our experimental results, which indicate that a magnesium to calcium ratio of 10 or more is required for $CaCO_3 \cdot H_2O$ formation, are in keeping with the previous findings of Nishiyama et al., (2013). The disappearance of monohydrocalcite is coincident with the widespread onset of nesquehonite precipitation, suggesting that the latter process is coincident with $CaCO_3 \cdot H_2O$ dehydration. It has been suggested that $CaCO_3 \cdot H_2O$ forms via the transformation of a calcium-rich hydrated magnesium-bearing amorphous carbonate precursor (Nishiyama et al., 2013), in which the transformation to monohydrocalcite occurs because dehydration is prevented by the presence of an external layer composed of hydrous Mg-carbonate. Accepting this, it follows that $CaCO_3 \cdot H_2O$ dehydration may have arisen because of the loss of hydrated Mg carbonate external groups from an amorphous carbonate precursor as a consequence of nesquehonite formation.

Experimental results show that the dominant anhydrous carbonate to form in the early stages of the experiments is magnesian calcite, with subordinate vaterite. Subsequently the dominant metastable polymorph is aragonite. Vaterite is commonly formed in experimental settings when $CaCO_3$ is rapidly precipitated (e.g., Hopkinson et al., 2008). The vaterite polymorph is unstable with respect to calcite and in an aqueous medium can rapidly transform to calcite through dissolution-precipitation reactions. The Mg^{2+} ion is known to accelerate this crystal transformation process (Chen et al., 2006).

Previous studies indicate that the presence of magnesium can retard or inhibit calcite crystallization and kinetically favour the formation of aragonite (e.g., Berner 1975; Reddy and Wang 1980). However independent studies show that if the MgO-CaO-CO_2-H_2O system exists at high supersaturation then calcite precipitates first (Fernandez-Diaz et al., 1996; Hu and Deng 2004) thereby potentially accounting for the presence of magnesian calcite prior to the onset of aragonite formation in the experiments documented here. Another possible reason favouring magnesian calcite formation relative to aragonite during CO_2 sparging relates to the higher solubility of the calcium salts (chloride, nitrate) relative to $Mg(OH)_2$, which may have facilitated reaction between calcium ions and CO_2 earlier than reactions between magnesium and CO_2. Previous

experimental studies have shown significant differences in reaction times between bicarbonate with calcium and magnesium ions (Bonales et al., 2013).

Aragonite formation relative to calcite is favoured when the precipitation rate, and especially the supply rate of CO_3^{2-} ions, is high (Hu and Deng 2004). In the experiments documented here, aragonite mainly precipitated during nesquehonite dissolution which is consistent with aragonite formation in conditions of low supersaturation with respect to calcium with nesquehonite dissolution providing a supply of CO_3^{2-} and Mg^{2+} ions. Results also show that although nesquehonite is unstable with respect to dypingite there is some evidence for more than one wave of nesquehonite formation (Figure 4.2). This may be consistent with a scenario in which the rate of nesquehonite dissolution proceeds at a faster rate than dypingite formation, in the process generating excess bicarbonate which is then periodically consumed during the formation of aragonite and nesquehonite until the excess bicarbonate is depleted.

Employing nitrate salts in the synthesis programme had no marked effect on the crystal chemistry of nesquehonite nor the overall nature of magnesium carbonate paragenesis in comparison to experiment [A]. However, aragonite formation in experiment [N] occurs conspicuously later than in experiments [A], [B] or [S]. One possible explanation is that aragonite precipitation was suppressed until nitrate depletion was achieved through nitro-magnesium carbonate [$Mg(NO_3)_2 \cdot 6H_2O$] generation.

4.5 Conclusions

Experiments [A] and [B] demonstrate that dissolution of $Mg(OH)_2$ by CO_2 sparging facilitated chlorartinite [$Mg_2(CO_3)Cl(OH) \cdot 3H_2O$] generation and abundant nesquehonite [$Mg(HCO_3,OH) \cdot 2H_2O$] formation. From this it is suggested that chlorartinite may represent a first formed intermediate between brucite [$Mg(OH)_2$] and nesquehonite. The absence of chlorartinite in a hydromagnesite-seeded environment suggests either that accelerated reaction rates made the phase extremely short lived, or that the direct path from $Mg(OH)_2$ to nesquehonite was kinetically favoured. Progressive decomposition of nesquehonite [$Mg(HCO_3OH) \cdot 2H_2O$] is accompanied by the generation of abundant

$Mg_5(CO_3)_4(OH)_2{\cdot}xH_2O$ mineral phases with subordinate barringtonite [$MgCO_3{\cdot}2H_2O$] detected after 30 days reaction. The latter mineral is interpreted to result from incongruent dissolution of nesquehonite. This further suggests that the length of the $Mg_5(CO_3)_4(OH)_2{\cdot}xH_2O$ reaction pathway from nesquehonite to hydromagnesite may be a precise function of nesquehonite dissolution kinetics and/or conditions of synthesis, thereby accounting for the disparity in experimental results reported from independent investigations on the nesquehonite to hydromagnesite transition (e.g., Davies and Bubela 1973; Zhang et al., 2006; Hopkinson et al., 2008, 2012).

In agreement with previous studies, when the magnesium to calcium ratio exceeds 10 or more, as in experiment [B], monohydrocalcite [$CaCO_3{\cdot}H_2O$] is produced. Loss of monohydrocalcite from the system coincides with nesquehonite formation, and is consistent with geochemical feedback between Ca and Mg carbonates driving mineral paragenesis. Magnesian calcite formation followed by aragonite generation coincident with nesquehonite formation and its subsequent transformation to dypingite-type phases is common to the four experiments (Kristova et al., 2014). This is consistent with aragonite formation being favoured in conditions of low supersaturation with respect to calcium, with nesquehonite dissolution providing a supply rate of CO_3^{2-} and Mg^{2+} ions. The differing solubilities of the calcium salts relative to $Mg(OH)_2$ may also have significant bearing on the particular $CaCO_3$ polymorph that nucleates and grows. Formation of magnesium nitrate hexahydrate [$Mg(NO_3)_2{\cdot}6H_2O$] is exclusive to experiment [N], the appearance of which exerts strong control on the timing of aragonite formation.

5 Final discussion

Carbonate rocks form about 25 % of the stratigraphic record, contain 50 % of the world's oil and serve as host rocks for important mineral deposits making studies of them of economic as well as academic interest (e.g., Gaffey 1987). Spectroscopies are also increasingly important in the elucidation of chemical and physical pathways of formation and transformation of carbonate minerals. Understanding of carbonation reactions will also potentially lead to the development of methods for the capture of CO_2 and/or the simultaneous production of industrially useful minerals (e.g., Hales et al., 2008; Frost et al., 2008a; Orlando et al., 2012). One of the long-term methods to store CO_2 is to convert it into thermodynamically stable mineral carbonates. Phase transformations in the Mg-carbonate system are known to be impacted by pH, temperature, and CO_2 and H_2O partial pressure (e.g. Königsberger et al., 1999; Hopkinson et al., 2008; Hänchen et al., 2008; Hopkinson et al., 2012). Naturally occurring silicate minerals such as serpentinites as well as alkaline industrial wastes can be used to capture and store CO_2 (Cipolli et al., 2004; Orlando et al., 2012; Gadikota et al., 2015). Brucite carbonation is of specific interest for CO_2 sequestration (e.g., Zhao et al., 2010; Fricker and Park 2013), particularly as a component of ultramafic mine wastes that can be exploited for its high reactivity (e.g. Harrison et al., 2015). In addition, spectroscopic investigations of carbonates are deemed important in planetary exploration programmes including characterisation of fine particles in dusts (e.g. Edwards et al., 2005; Rividi, et al. 2010).

The objectives of this study were to 1) provide an analytical means to employ portable Raman and NIR spectroscopies in a capacity for fully quantitative analysis of carbonate mineral mixtures, 2) apply the spectroscopic findings to advanced understanding of the real time kinetics of reaction pathways in low temperature experimental settings in the system CaO-MgO-CO_2-H_2O. These aims were achieved although the NIR technique did not yield satisfactory results and Raman spectroscopy is limited by effect of particle size, further findings are discussed below.

The first aim, quantitative analysis by RS and NIR, has been assessed by a four-way quantification procedure. The calibration by RS shows accuracy and precision comparable to laboratory-based position-sensitive XRD. However, during this study there were recognized theoretical as well as technical limitations which are worthy of

further discussion. Amongst the issues of RS applications to carbonate analysis are overlapping bands of separate carbonate mineral phases, identification of short-range order and particle size effects.

During the quantitative work, the quaternary mixtures were prepared knowing that some of the minerals' main RS bands are just a few wavenumbers apart. These overlapped bands of four or less components were resolved with chemometrics. However the number of components in a mixture that can be securely identified is limited. It is hard to foresee how many components in a mixture could be successfully resolved by RS. This issue is compounded by the fact that Raman spectral positions described in literature vary usually by few wavenumbers where data might be influenced and spectra shifted for various reasons coming from instrument (calibration, resolution of the instrument), sample (axis dependency, disorder in sample, level of hydration of molecule) or data manipulation (peak assignment).

The four carbonate minerals (hydromagnesite, magnesite, dolomite and huntite) were also investigated by NIR although NIR did not yield a satisfactory 4-way quantification model even though data manipulation was performed in combination with several spectral pre-processing methods. The NIR spectral intensity is related to concentration although it has been reported that its absolute value can be influenced by sample packing, grain size, presence of air moisture etc. Our findings indicate that there is not one sole cause for failing of the carbonate calibration by NIR. It seems that the fine particle size and associated adsorption of moisture contributed to other factors such as misbalance between strong features in NIR spectrum of hydromagnesite and very weak bands in spectra of other measured carbonate minerals. The work of Gaffey (1986) implies that Lambert's Law appears to describe NIR absorption features in carbonates regardless of the form of the sample i.e., powders and/or rock. It is plausible that this apparent disparity in conclusions may stem from the fact that samples investigated by Gaffey were coarser grain size (*ca.* 38-500 μm) in comparison to samples utilized in this work (4-7 μm).

Particle sizes of measured samples in quantitative analysis chapter were controlled (modes 4-7 μm) and particle size distributions were assessed by scanning electron microscopy and laser diffraction. This was done to minimize the potential of particle size effects significantly influencing spectral contrast as well as relative ratios of peak heights,

which were investigated in a separate experiment, in which the effects of particle size on the fundamental vibrations of the [CO_3^{2-}] anion in calcite were analysed by total attenuated reflectance infrared spectroscopy (ATR-IR) and RS. Results show that both ATR-IR and Raman indicate two critical points in internal mode behaviour of the Raman and infrared active ν_4 and ν_3 internal modes, the first at between 42-59 μm size range and the second between 19 and 5 μm. Results are interpreted in terms of specular to volume (diffuse) coherent transitions of internal modes and with further grain refinement internal mode specific optically thick to thin transitions (more details can be found in relevant chapter.

There is no reason to suppose that this relationship between particle size and [CO_3^{2-}] internal mode behaviour is unique to calcite. To explore this possibility a small pilot study was conducted on dolomite. Five size fractions of dolomite were prepared and measured by Raman spectroscopy. The first four fractions were separated by sieving and the finest fraction created by further milling of the smallest sieved sample. Spectroscopic analysis were performed on lightly pressed samples in aluminum sample holders prepared in the same manner as samples in the quaternary quantification. The mode sizes of the fractions measured by PSA laser diffraction were 145 μm, 98 μm, 56 μm, 15 μm and 2 μm. The Raman intensity increased with decreasing particle size until reaching 56 μm (Figure 5.1). Below this size the Raman intensity decreased with decreasing size. The Raman intensity increase was *ca.* 15 % in the 145-56 μm sample range. The decrease in intensity was somewhat smaller (*ca.* 6 %) in the 56-2 μm sample size range.

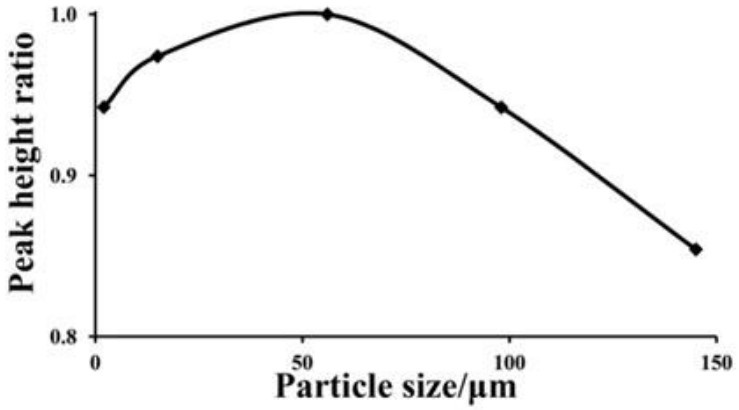

Figure 5.1: Particle size effect on Raman intensity of dolomite, plotted as peak height ratio I/I_{max} (i.e. measured intensity/maximum intensity measured from 56 μm particle size fraction) against particle size.

Hence, evidence suggests that the Raman signal increases as the grain size decreases, but then subsequently the intensity decreases with an increased proportion of very fine particles. One possible interpretation is that the observed relationship registers a shift in relative contribution of particle sizes, packing, and surface defect concentration to the observed intensity. In the case of comparatively large particles, the measured intensity reflects primarily the relative contribution of voids and particles. With decreasing particle sizes (nanometer scale) the intensity decreases primarily as a function of high-defect concentrations in closely packed small particles. Therefore it seems likely that particle size effects may well be common to all carbonates, but this remains to be systematically explored.

The Raman quantitative measurements were compared to XRD results which gave very similar values suggesting that quantification has not been compromised by particle size effects because the grain size distributions were sufficiently narrow and particles were small enough allowing measurements of representative sample within measurements of the spectrophotometer spot size (100 μm) (Figure 2.3 is repeated here to demonstrate this). In addition SEM observations show that the size of the measured samples was smaller than those found by laser diffraction. At the same time the findings from the size experiment on dolomite shows that the size range (change in size) was greater than the change in internal mode behaviour.

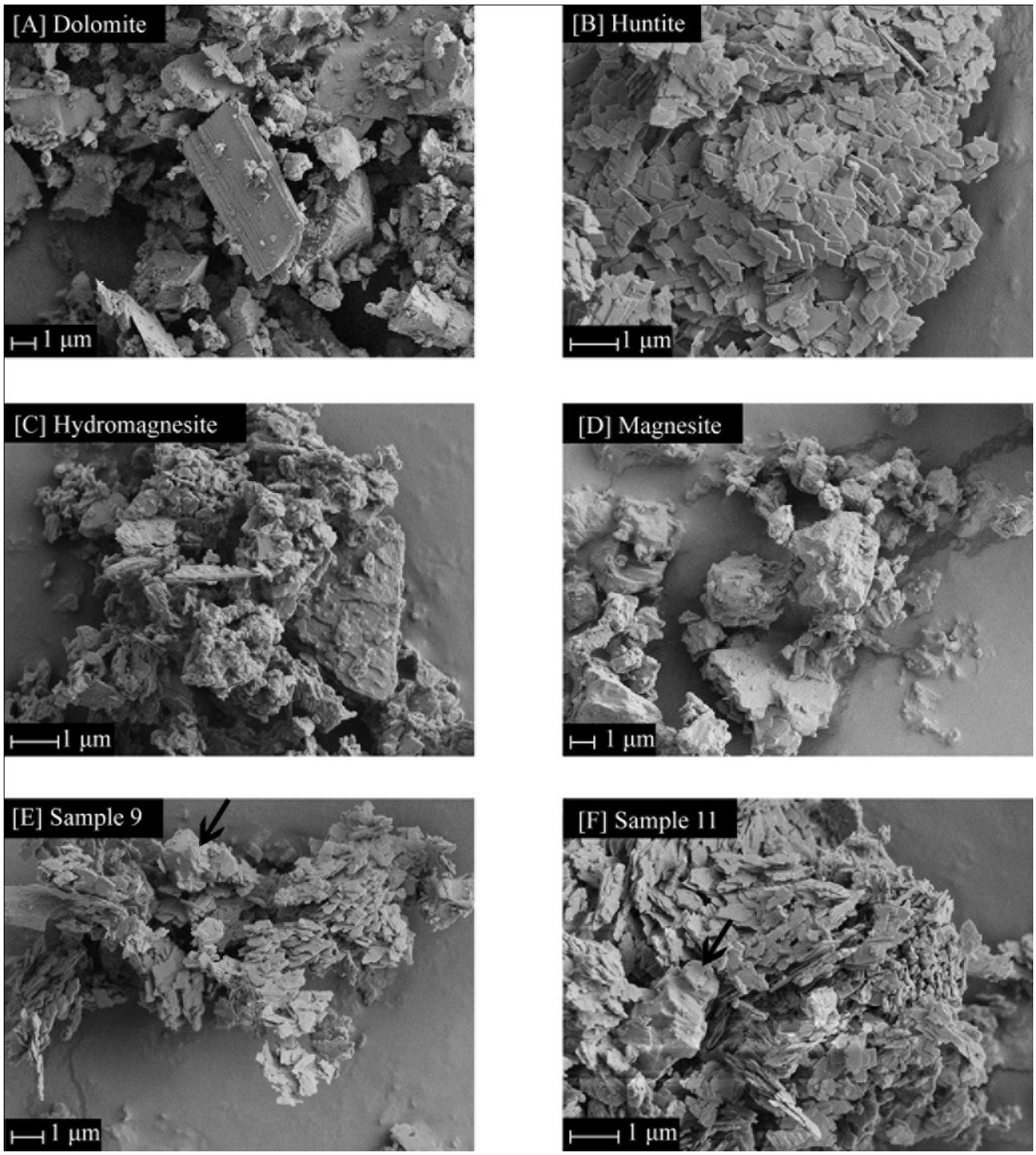

Figure 5.2: Back-scattered scanning electron microscope images of: a) Dolomite reference material, b) Huntite reference material, c) Synthetic hydromagnesite reference material, d) Magnesite reference material, e) Aggregate of interspersed hydromagnesite and huntite platelets, with conchoidal fractured magnesite rhomb, marked with arrow (sample 9, Table 2.1), f) Aggregate of micron-sized huntite plates, interspersed with similarly sized fragments of dolomite, alongside a *ca*. 1.4 µm long residual coarse grained dolomite crystal, marked with arrow (sample 11, Table 2.1).

RS has been successfully utilized in characterisation of synthetic powder samples yielded during carbonation reaction in the CaO-MgO-CO_2-H_2O system. However, while in the four-way calibration RS and XRD gave broadly the same results, differences between analyses by RS and XRD were evident in the characterisation of minerals during carbonation reaction. Each technique (RS and XRD) was able to provide different details of the reaction and at the same time reassure finding from each other technique. For example XRD gave more detail on hydrated magnesium carbonates while RS was able to detect some mineral phases in earlier samples than XRD. The investigation of carbonation reactions by XRD could discriminate the basic magnesium carbonate hydrates [$Mg_5(CO_3)_4(OH)_2 \cdot xH_2O$] containing 5 and 8 molecules of water. However these could be only distinguished by XRD and not by RS. This may be explained by order of the measurement i.e. short-range order (RS) and long range order (XRD). Short-range order refers to interaction on distance approximate to first or second neighbouring atoms e.g. functional groups of a molecule, whereas long-range order refers to unit cell dimensions. In other words the minerals may vary only in their long-range order level i.e. their polarizability may remain the same. At the same time there is an absence of a comprehensive international certified Raman spectroscopic library, for instance, the spectrum of barringtonite is yet to be published. On the other hand RS was able to detect some mineral phases in earlier samples in comparison to XRD. For example bands of nitrate phases were detected by Raman in all samples from day zero while XRD detected the presence of magnesium nitrate hexahydrate [$Mg(NO_3)_2 \cdot 6H_2O$] in samples from sixteenth day (N16) onwards (Figures 4.2 and 4.4). This is possibly due to an amorphous or poorly crystalline character of the mineral phases during the early reaction stages. Another explanation may be that nitrate-assigned Raman active bands in samples prior to day 16 are caused by product phases either as dispersed inclusions or bands adsorbed between structural layers.

Previous studies showed that multiple pathways exist for carbon sequestration in MgO-CO_2-H_2O (e.g. Davies and Bubela 1973; Hopkinson et al., 2008; Hänchen et al., 2008; Hopkinson et al., 2012). There are only a few studies that investigated a system combining magnesium and calcium as well as carbon dioxide, water and chloride or nitrate salts and these studies used different condition such as temperature and CO_2 saturation during the reaction stages (e.g. Hopkinson et al., 2008). Our results despite the different reaction conditions during the latter stages of the reaction have very similar

initial conditions, including the presence of calcium chloride. The overall findings are in broad agreement that decomposition of nesquehonite [$Mg(HCO_3,OH)\cdot 2H_2O$] leads to formation of magnesium carbonate hydrates [$Mg_5(CO_3)_4(OH)_2.xH_2O$] where these hydrated phases contain varying amount of crystalline water and the reaction in its early stage is accompanied by formation of other phases such as e.g. magnesian calcite, vaterite, monohydrocalcite etc. However, our study shows that one of the early phases is chlorartinite. The absence of chlorartinite in a study by Hopkinson et al. (2008) may be due to removal of some CO_2 from the reaction system by its filtration at a very early stage (after sparging). Chlorartinite formation initially occurred in association with $Mg(OH)_2$ and $Mg(HCO_3,OH)\cdot 2H_2O$ and was detected by XRD in samples from experiments [A] and [B] over the first 20 days. The results from this study indicate that chlorartinite formation preceded, at least in part, nesquehonite decomposition and the coeval generation of $Mg_5(CO_3)_4(OH)_2\cdot xH_2O$ phases. This is in accordance with other studies where artinite type minerals (pseudoartinite, chlorartinite) were found at the onset of the carbonation reaction (De Vito et al., 2012; Harisson et al., 2016). However chlorartinite and artinite have not been reported as metastable intermediates of the nesquehonite to hydromagnesite transition (e.g., Davies and Bubela 1973). Little is known about the stability field of chlorartinite, and the mineral stability needs to be ascertained.

Future work

Findings from investigations of the effect of particle size on IR and RS measurements of carbonate minerals as well as the results from carbonation reaction open up many interesting possibilities for future research. These include investigations of choice of an 'ideal size range' for quantitative carbonate measurements in terms of optically thick to thin transition. Different particle size fractions of calcite measured in this work were prepared by grinding and further sieving. This process led to defects on the individual crystals and it would be interesting to compare particle size effect results to the same effect on particles precipitated in a small particle size which would not contain as many defects.

Research on the system $CaO\text{-}MgO\text{-}CO_2\text{-}H_2O$ confirms that complex arrays of metastable mineral phases are produced during CO_2 sequestration at low near surface temperatures

(*ca.* 35°C). If the aim is to not only sequester CO_2 but find industrial applications for the resultant magnesium bearing carbonate minerals, the products of synthesis will be gauged on purity, particle size and shape distributions. In case of the industrial mineral hydromagnesite, which finds application in the mineral flame retardant market, as it is water bearing and 37.8 wt % of each mineral consists of CO_2, experimental results suggest that the mineral formed at 35 °C is dypingite. Carbonate content of dypingite is *ca.* 36.3 % although thermal properties of synthetic dypingite are less favourable due to its earlier onset values of water decomposition which also happens over more steps then in hydromagnesite (e.g. Botha and Strydom 2001; Frost et al., 2008b). The dypingite's attainment of desired particle sizes (1 μm mean) and shape (platy habit) are achievable at low temperatures, although agglomeration is problematic. More importantly the presence of undesired acicular metastable hydrates compromises the issue of shape consistency and, it may well be the case that attainment of high purity hydromagnesite assemblages at experimental time scales can only be actualised by synthesis at temperatures above the nesquehonite → hydromagnesite transition, which is frequently cited as 52 °C (e.g., Davies and Bulbela 1973; Hopkinson et al., 2008).

NIR of carbonate minerals is a far less investigated area than mid-IR and RS. Carbonate bands found in the NIR region are not fully understood and, it is not yet known how bands occurring in the mid-IR and Raman spectra relate to bands found in the NIR region. However, given that carbonate-related bands in the NIR region are overtones and combination bands (e.g., Gaffey 1986) of internal mode vibrations, or else at least in part stem from anharmonic coupling of degenerate internal mode(s) with external (lattice) modes (Hopkinson and Rutt 2016), it seems likely that carbonate mineral NIR spectral features may well be sensitive to as yet undocumented particle grain size effects.

References

Addadi, L., Raz, S. and Weiner, S. (2003) Taking Advantage of Disorder: Amorphous Calcium Carbonate and Its Roles in Biomineralization. *Advanced Materials*, 15, 959-970.

Alderman, A. R. (1965) Dolomitic sediments and their environment in the south-east of South Australia. *Geochimica Cosmochimica Acta*, 29, 1355-1365.

Alonso-Zarza, A. M. and Martín-Pérez, A. (2008) Dolomite in caves: Recent dolomite formation in oxic, non-sulfate environments. Castañar Cave, Spain. *Sedimentary Geology*, 205, 160–164.

Alonso-Zarza, A. M, Martin-Perez, A., Martin-Garcia, R., Gil-Pena, I., Melendez, A., Martinez-Flores, E., Hellstrom, J. and Munoz-Barco, P. (2011) Structural and host rock controls on the distribution, morphology and mineralogy of speleothems in the Casta˜nar Cave (Spain). *Geological Magazine,* 148, *pp. 211–225.*

Andersen, F. A. and Brecevic, L. (1991) Infrared spectra of Amorphous and Crystalline Calcium Carbonate. *Acta Chemica Scandinavica*, 45, 1018-1024.

Ballirano, P., De Vito, C., Ferrini, V., and Mignardi, S. (2010) The thermal behaviour and structural stability of nesquehonite, $MgCO_3 \cdot 3H_2O$, evaluated by *in situ* laboratory parallel-beam X-ray powder diffraction: New constraints on CO_2 sequestration within minerals. *Journal of Hazardous Materials*, 178, 522–528.

Bakeev, K. A., (2008) Process Analytical Technology: Spectroscopic Tools and Implementation Strategies for the Chemical and Pharmaceutical Industries, pp 472, Blackwell Publishing Ltd, Oxford.

Baldridge, A. M., Hook, S. J., Grove, C. I. and Rivera, G. (2009) The ASTER spectral library version 2.0. *Remote Sensing of Environment*, 113, 711–715.

Ballirano, P., De Vito, C., Mignardi, S. and Ferrini, V. (2013) Phase transitions in the Mg-CO_2-H_2O system and the thermal decomposition of dypingite, $Mg_5(CO_3)4(OH)_2.5H_2O$: Implications for geosequestration of carbon dioxide. *Chemical Geology*, 340, 59-67.

Beck, C.W. (1950) Differential thermal analysis curves of carbonate minerals. *American Mineralogist*, 12, 985-1013.

Berner, R. A. (1975) The role of magnesium in the crystal growth of calcite and aragonite from sea water. *Geochimica et Cosmochimica Acta*, 39, 495-504.

Berntsson, O., Danielsson, L.-G., Johansson, M. O. and Folestad, S. (2000) Quantitative determination of content in binary powder mixtures using diffuse reflectance near infrared spectrometry and multivariate analysis. *Analytica Chimica Acta*, 419, 45-54.

Bischoff, W. D., Sharma, S. K. and Mackenzie, F. T. (1985) Carbonate ion disorder in synthetic and biogenic magnesian calcites: a Raman spectral study. *American Mineralogist*, 70, 581-589.

Bischoff, W. D., Bertram, M. A., Mackenzie, F. T., and Bishop, F. C. (1993) Diagenetic stabilization pathways of magnesian calcites. *Carbonates and Evaporates*, 8, 82-89.

Blanco, M., Coello, J., Iturriaga, H., Maspoch, S. and de la Pezuela, C. (1997) Effect of Data Preprocessing Methods in Near-Infrared Diffuse Reflectance Spectroscopy for the Determination of the Active Compound in a Pharmaceutical Preparation. *Applied Spectroscopy*, 51, 240-246.

Blanco, M., Coello, J., Iturriaga, H., Maspoch, S. and Pages, J. (1999) Calibration in non-linear near infrared reflectance spectroscopy: a comparison of several methods. *Analytica Chimica Acta*, 384, 207-214.

Blanco, M. and Villarroya, I. (2002) NIR spectroscopy: a rapid-response analytical tool. *Trends in Analytical Chemistry*, 21, 240-250.

Bonales, L.J., Muñoz-Iglesias, V., Santamaría-Pérez, D., Caceres, M., Fernandez-Remolar, D. and Prieto-Ballesteros, O. (2013) Quantitative Raman spectroscopy as a tool to study the kinetics and formation mechanism of carbonates. *Spectrochimica Acta Part A*, 116, 26-30.

Botha, A. and Strydom, C. A. (2001) Preparation of magnesium hydroxy carbonate from magnesium hydroxide. *Hydrometallurgy,* 62, 175-183.

Böttcher, M. E., Gehlken, P.-L. and Steele, D. F. (1997) Characterization of inorganic and biogenic magnesian calcites by Fourier Transform infrared spectroscopy. *Solid State Ionics*, 101-103, 1379-1385.

Brady, P. V., Krumhansl, J. L. and Papenguth, H. W. (1996) Surface complexation clues to dolomite growth. *Geochimica et Cosmochimica Acta*, 60, 727-731.

Bugay, D. E. (2001) Characterization of the solid-state: spectroscopic techniques. *Advanced Drug Delivery Reviews*, 48, 43-65.

Burns, G. (1977) Introduction to Group Theory with Applications, in Materials Science Series, editors Alper, A.M. and Nowick, A.S. Academic Press, Inc. New York, pp 1-429.

Burns, S. J., McKenzie, J. A. and Vasconcelos, C. (2000) Dolomite formation and biogeochemical cycles in the Phanerozoic. *Sedimentology*, 47 (Suppl. 1), 49-61.

Calvo, J. P., Stamatakis, M. G. and Magganas, A. C. (1995) Clastic huntite in upper Neogene formations of the Kozani basin, Macedonia, northern Greece. *Journal of Sedimentary Research*, A65, 627-632.

Canterford, J. H., Tsambourakis, G. and Lambert, B. (1984) Some observations on the properties of dypingite $Mg_5(CO_3)_4(OH)_2{\cdot}5H_2O$, and related minerals. *Mineralogical Magazine*, 48**,** 437-442.

Carache, M., Herrero, A. and Carmona, P. (2002) Raman Analysis of White Spots Appearing in the Shell of Argenitne Red Shrimp (Pleoticus muelleri) during Frozen Storage. *Journal of Food Science*, 67, 2892-2895.

Cheilakou, E., Troullinos, M. and Koui, M. (2014) Identification of pigments on Byzantine wall paintings from Crete (14th century AD) using non-invasive Fiber Optics Diffuse Reflectance Spectroscopy (FORS). *Journal of Archaeological Science*, 41, 541-555.

Chen, T., Neville, A. and Yuan, M. D. (2006) Influence of Mg^{2+} on $CaCO_3$ formation-bulk precipitation and surface deposition. *Chemical Engineering Science*, 61, 5318-5327.

Chen, Z. P., Li, L. M., Jin, J. W., Nordon, A., Littlejohn, D., Yang, J., Zhang, J. and Yu, R. Q. (2012) Quantitative Analysis of Powder Mixtures by Raman Spectrometry: the influence of particle size and its correction. *Analytical Chemistry*, 84, 4088-4094.

Choquette, S. J., Travis, J. C., Zhu, C. and Duewer, D. L. (2002) Wavenumber Standards for Near-infrared Spectroscopy, Handbook of Vibrational Spectroscopy, *Chalmers, J.M. and Griffiths P.R. (ed.)*, Published by: John Wiley.

Cipolli, F., Gambardella, B., Marini, L., Ottonello, G. and Vetuschi Zuccolini, M. V. (2004) Geochemistry of high-pH waters from serpentinites of the Gruppo di Voltri (Genova, Italy) and reaction path modelling of CO_2 sequestration in serpentinite aquifers. *Applied Geochemistry*, 19, 787–802.

Cole, W. F. and Lancucki, C. J. (1975) Huntite from Deer Park, Victoria, Australia. *American Mineralogist*, 60, 1l30-1131.

Coleyshaw, E. E., Crump, G. and Griffith, W. P. (2003) Vibrational spectra of the hydrated carbonate minerals ikaite, monohydrocalcite, lansfordite and nesquehonite. *Spectrochimica Acta Part A*, 59, 2231-2239.

Conel, J. E. (1969) Infrared Emissivities of Silicates: Experimental Results and a Cloudy Atmosphere Model of Spectral emission from Condensed particulate Mediums. *Journal of Geophysical Research*, 74, 1614-1634.

Culka, A., Jehlicka, J., Vandenabeele, P. and Edwards, H. G. M. (2011) The detection of biomarkers in evaporate matrices using a portable Raman instrument under Alpine conditions. *Spectrochimica Acta Part A*, 80, 8-13.

Dandeu, A., Humbert, B., Carteret, C., Muhr, H., Plasari, E., and Bossoutrot, J. M. (2006) Raman Spectroscopy – A Powerful Tool for the Quantitative Determination of the Composition of Polymorph Mixtures: Application to $CaCO_3$ Polymorph Mixtures. *Chemical Engineering & Technology*, 29, 221-225.

Davies, P. J., and Bubela, B. (1973) The transformation of nesquehonite into hydromagnesite. *Chemical Geology*, 12, 289-300.

Davies, P. J., Bubela, B. and Ferguson, J. (1977) Simulation of carbonate diagenetic processes: Formation of dolomite, huntite and monohydrocalcite by the reaction between nesquehonite and brine. *Chemical Geology*, 19, 187-214.

De Leeuw, N. H. and Parker, S. C. (2001) Surface-water interactions in the dolomite problem, *Physical Chemistry Chemical Physics*, 3, 3217-3221.

De Vito, C., Ferrini, V., Mignardi, S., Cagnetti, M. and Leccese, F. (2012) Progress in carbon dioxide sequestration via carbonation of aqueous saline wastes. *Periodico di Mineralogia*, 81, 333-344.

Deelman, J. C. (1999) Low-temperature nucleation of magnesite and dolomite. *Neues Jahrbuch für Mineralogie Monatshefte*, 7, Stuttgart, 289-302.

Dell, R. M. and Weller, S. W. (1959) The thermal decomposition of nesquehonite $MgCO_3 \cdot 3H_2O$ and magnesium ammonium carbonate $MgCO_3 \cdot (NH_4)_2CO_3 \cdot 4H_2O$. *Transactions of the Faraday Society*, 55, 2203-2220.

Dennis, A. (2007) Photo-Bleaching and Automatic baseline Correction for Raman Spectroscopy, Perkin Elmer, Technical note. Waltham, USA. www.perkinelmer.com

Dollase, W. A. and Reeder, R. J. (1986) Crystal structure refinement of huntite $CaMg_3(CO_3)_4$, with x-ray powder data. *American Mineralogist*, 71, 163-166.

Domingo, C., Loste, E., Gomez, J., Garcia-Carmona, J. and Fraile, J. (2006) Calcite precipitation by a high-pressure CO_2 carbonation route. *The Journal of Supercritical Fluids*, 36, 202–215.

Doner, H. E. and Lynn, W. C. (1989) Carbonate, Halide, Sulfate, and Sulfide Minerals, in Minerals in Soil Environments, *J.B. Dixon and S.B. Weed (ed.),* Published by: Soil Science Society of America.

Edwards, H. G. M., Villar, S. E. J., Jehlicka, J. and Munshi, T. (2005) FT-Raman spectroscopic study of calcium-rich and magnesium-rich carbonate minerals. *Spectrochimica Acta Part A*, 61, 2273-2280.

Fernandez-Diaz, L., Putnis, A., Prieto, M. and Putnis, C. V. (1996) The role of magnesium in the crystallization of calcite and aragonite in a porous medium. *Journal of Sedimentary Research,* 66, 482-491.

Ferrini, V., De Vito, C., and Mignardi, S. (2009) Synthesis of nesquehonite by reaction of gaseous CO_2 with Mg chloride solution: Its potential role in the sequestration of carbon dioxide. *Journal of Hazardous Materials*, 168, 832–837.

Fevotte, G. (2007) In Situ Raman Spectroscopy for In-line Control of Pharmaceutical Crystallization and Solids Elaboration Processes: A Review. *Chemical Engineering Research & Design*, 85, 906-920.

Fricker, K. J., Park, A.-H. A. (2013) Effect of H_2O on $Mg(OH)_2$ carbonation pathways for combined CO_2 capture and storage. *Chemical Engineering Science,* 100, 332–341.

Friedel, B. (1975) Synthetischer Giorgiosit. *Neues Jahrbuch Mineral Monatsh,* 196–208.

Frost, R. L., Erickson, K. L. and Kloprogge, T. J. (2005) Vibrational spectroscopic study of the nitrate containing hydrotalcite mbobomkulite. *Spectrochimica Acta Part A*, 61, 2919-2925.

Frost, R. L. and Musumeci, A. W. (2006) Nitrate absorption through hydrotalcite reformation. *Journal of Colloid and Interface Science*, 302, 203-206.

Frost, R. L. and Dickfos, M. J. (2007a) Raman spectroscopy of halogen-containing carbonates. *Journal of Raman Spectroscopy*, 38, 1516-1522.

Frost, R. L. and Dickfos, M. J. (2007b) Hydrated double carbonates – a Raman and infrared spectroscopic study. *Polyhedron*, 26, 4503-4508.

Frost, R. L., Bahfenne, S., Graham, J. and Reddy, B. J. (2008a) The structure of selected magnesium carbonate minerals – A near infrared and mid-infrared spectroscopic study, *Polyhedron*, 27, 2069-2076.

Frost, R. L., Bahfenne, S., Graham, J. and Martens, W. N. (2008b) Thermal stability of artinite, dypingite and brugnatellite- implications for the geosequestration of green house gases. *Thermochimica Acta*, 475(1-2), 39-43.

Frost, R. L., Reddy, B. J., Bahfenne, S. and Graham, J. (2009a) Mid-infrared and near-infrared spectroscopic study of selected magnesium carbonate minerals containing ferric iron—Implications for the geosequestration of greenhouse gases. *Spectrochimica Acta Part A*, 72, 597–604.

Frost, R. L., Bahfenne, S. and Graham, J. (2009b) Raman spectroscopic study of the magnesium carbonate minerals – artinite and dypingite. *Journal of Raman Spectroscopy*, 40, 855-860.

Frost, R. L. (2011) Raman spectroscopic study of the magnesium carbonate mineral

hydromagnesite ($Mg_5[CO_3)_4(OH)_2].4H_2O$). *Journal of Raman Spectroscopy*, 42, 1690-1694.

Gadikota, G., Fricker, K., Jang, S. H. and Park, A.-H. A. (2015) Carbonation of Silicate Minerals and Industrial Wastes and Their Potential Use as Sustainable Construction Materials. Edited by: Jin, F., He, L. N., and Hu, Y.H., *Advances in CO_2 Capture, Sequestration, and Conversion, ACS Symposium Series*, Volume: 1194, pp 295-322.

Gaffey, S. J. (1985) Reflectance spectroscopy in the visible and near-infrared (0.35-2.55 μm): Applications in carbonate petrology. *Geology*, 13, 270-273.

Gaffey, S. J. (1986) Spectral reflectance of carbonate minerals in the visible and near infrared (0.35-2.55 microns): calcite, aragonite, and dolomite. *American Mineralogist*, 71, 151-162.

Gaffey, S. J. (1987) Spectral Reflectance of Carbonate Minerals in the Visible and Near Infrared (0.35-2.55 μm): Anhydrous Carbonate Minerals. *Journal of Geophysical Research*, 92, 1429-1440.

Garcia, F., Le Bolay, N. and Frances, C. (2002) Changes of surface and volume properties of calcite during a batch wet grinding process. *Chemical Engineering Journal*, 85, 177–187.

Germer, T. A, Zwinkels, J. C. and Tsai, B. K. (2014) Spectrophotometry: Accurate Measurement of Optical Properties of Materials, pp 560, Volume 46, Elsevier, London.

Goldsmith, J. R. (1953) A "simplexity principle" and its relation to "ease" of crystallization. *Journal of Geology*, 61, 439-451.

Graf, D. L., Eardley, A. J., and Shimp, N. F. (1961) A Preliminary Report on Magnesium Carbonate Formation in Glacial Lake Bonneville. *Journal of Geology*, 69, 219–223.

Griffiths, P. R. and Haseth, J. A. (2007) Fourier Transform Infrared Spectrometry,

Chemical Ananlysis, A Series of Monographs on Analytical Chemistry and Its Applications, Vol. 171, Series Editor J.D. Winefordner, Wiley, Second Edition, pp529.

Gunasekaran, S., Anbalagan, G. and Pandi, S. (2006) Raman and infrared spectra of carbonates of calcite structure. *Journal of Raman Spectroscopy*, 37, 892-899.

Hales, M. C., Frost, R. L. and Martens, W. N. (2008) Thermo-Raman spectroscopy of synthetic nesquehonite – implications for the geosequestration of greenhouse gases. *Journal of Raman Spectroscopy,* 39, 1141-1149.

Hänchen, M., Prigiobbe, V., Baciocchi, R. and Mazzotti, M. (2008) Precipitation in the Mg-carbonate system- effects of temperature and CO_2 pressure. *Chemical Engineering Science*, 63, 1012-1028.

Hapke, B. (1981) Bidirectional reflectance spectroscopy: 1. Theory. *Journal of Geophysical Research: Solid Earth,* 86, 3039–3054.

Hapke, B. (2008) Bidirectional reflectance spectroscopy 6. Effects of porosity. *Icarus,* 195, 918-926.

Hapke, B. (2012) Theory of Reflectance and Emittance Spectroscopy. Pp 1-513, Second Edition, Cambridge University Press, Cambridge.

Harrison, A. L., Dipple, G. M., Power, I. M. and Mayer, K. U. (2015) Influence of surface passivation and water content on mineral reactions in unsaturated porous media: Implications for brucite carbonation and CO_2 sequestration. *Geochimica et Cosmochimica Acta*, 148, 477-495.

Hasse, B., Ehrenberg, H., Marxen, J. C., Becker, W. and Epple, M. (2000) Calcium carbonate Modifications in the Mineralized Shell of the Freshwater Snail *Biomphalaria glabrata*. *Chemistry:A European Journal*, 6, 3679-3685.

Heinz, A., Savolainen, M., Rades, T., Strachan, C. (2007) Quatifying ternary mixtures of different solid-state forms of indomethacin by Raman and near-infrared spectroscopy. *European Journal of Pharmaceutical sciences*, 32, 182-192.

Higgins, S. R. and Hu, X. (2005) Self-limiting growth on dolomite: Experimental observations with in situ atomic force microscopy. *Geochimica et Cosmochimica Acta*, 69, 2085–2094.

Hill, R. J., Canterford, J. H. and Moyle, F. J. (1982) New data for landsfordite. *Mineralogical Magazine,* 46, 453–457.

Hirsch, H. and Arnold, G. (1993) Fourier-Transform Spectroscopy in Remote-Sensing of Solid Planetary Surfaces. *Vibrational Spectroscopy*, 5, 119-123.

Hollingberry, L. A. and Hull, T. R. (2010) The fire retardant behavior of huntite and hydromagnesite – A review. *Polymer Degradation and Stability*, 95, 2213-2225.

Hollingbery, L. A. and Hull, T. R. (2012) The fire retardant effects of huntite in natural mixtures with hydromagnesite. *Polymer Degradation and Stability*, 97, 504-512.

Hopkinson, L. J., Rutt, K. J. and Cressey, G. (2008) The Transformation of Nesquehonite to Hydromagnesite in the System CaO-MgO-H_2O-CO_2: An Experimental Spectroscopic Study. *The Journal of Geology*, 116, 387-400.

Hopkinson, L. J., Kristova, P., Rutt, K. J., and Cressey, G. (2012) Phase transitions in the system MgO-CO_2-H_2O during CO_2 degassing of Mg-bearing solutions. *Geochimica et Cosmochimica Acta*, 76, 1-13.

Hopkinson, L. and Rutt, K. J. (2016) Crystal chemical correlations between the mid and near-infrared in carbonate minerals, *Spectrochimica Acta Part A*, 162, 105-108.

Hu, Z. and Deng, Y. (2003) Supersaturation control in aragonite synthesis using sparingly soluble calcium sulfate as reactants. *Journal of Colloid and Interface Science,* 266, 359–365.

Hu, Z. and Deng, Y. (2004) Synthesis of needle-like aragonite from calcium chloride and sparingly soluble magnesium carbonate. *Powder Technology*, 140, 10– 16.

Hu, Z., Shao, M., Cai, Q., Ding, S., Zhong, C., Wei, X. and Deng, Y. (2009) Synthesis of needle-like aragonite from limestone in the presence of magnesium chloride. *Journal of Materials Processing Technology*, 209, 1607–1611.

Huang, C. K. and Kerr, P. F. (1960) Infrared study of the carbonate minerals. *American Mineralogist*, 45, 311-324.

Hunt, G. R. and Vincent, R. K. (1968) The Behavior of Spectral Features in the Infrared emission from Particulate Surfaces of Various Grain Sizes. *Journal of Geophysical Research*, 73, 6039-6046.

Hunt, G. R. and Logan, L. M. (1972) Variation of Single Particle Mid-Infrared Emission Spectrum with Particle Size. *Applied Optics*, 11, 142-147.

Jaffe, H. H. and Orchin, M. (1965) Symmetry in Chemistry, by John Wiley & Sons, Inc, New York, pp. 191.

Jehlicka, J., Vitek, P., Edwards, H. G. M., Heagraves, M., and Capoun, T. (2009) Application of portable Raman instruments for fast and non-destructive detection of minerals on outcrops. *Spectrochimica Acta Part A*, 73, 410-419.

Jehlicka, J., Culka, A., Vandenabeele P. and Edwards, H. G. M. (2011) Critical evaluation of a handheld Raman spectrometer with near infrared (785nm) excitation for field identification of minerals. *Spectrochimica Acta Part A*, 80, 36-40.

Kaabar, W., Bott, S. and Devonshire, R. (2011) Raman spectroscopic study of mixed carbonate materials. *Spectrochimica Acta Part A*, 78, 136-141.

Kamiya, K., Sakka, S. and Terada, K. (1977) Aragonite formation through precipitation of calcium carbonate monohydrate. *Materials Research Bulletin*, 12, 1095-1102.

Kazakov, A. V., Tikhomirova, M. M. and Plotnikova, V. I. (1959) The system of carbonate equilibria. *International Geological Review,* 1, 1-39.

Kedra-Krolik, K. and Gyericz, P. (2009) Precipitation of nanostructured calcite in a controlled multiphase process. *Journal of Crystal Growth,* 311, 3674-3681.

Kimura, T. And Koga, N. (2011) Thermal Dehydration of Monohydrocalcite: Overall Kinetics and Physico-geometrical Mechanisms. *The Journal of Physical Chemistry A*, 115, 10491-10501.

Kinsman, D. J. J. (1967) Huntite from a carbonate evaporite environment. *American Mineralogist*, 52, 1332-1340.

Kitamura, M., Konno, H., Yasui, A. and Masuoka, H. (2002) Controlling factors and mechanism of reactive crystallization of calcium carbonate polymorphs from calcium hydroxide suspensions. *Journal of Crystal Growth,* 236, 323–332.

Königsberger, E., Königsberger, L.-C., and Gamsjäger, H. (1999) Low temperature thermodynamic model for the system: Na_2CO_3-$MgCO_3$-$CaCO_3$-H_2O. *Geochimica et Cosmochimica Acta,* 63, 3105-3119.

Kristova, P., Hopkinson, L., Rutt, K., Hunter, H. and Cressey, G. (2013) Quantitative analyses of powdered multi-minerallic carbonate aggregates using a portable Raman spectrometer. *American Mineralogist,* 98, 401-409.

Kristova, P., Hopkinson, L. J., Rutt, K. J., Hunter, M. A. and Cressey, G. (2014) Carbonate mineral paragenesis and reaction kinetics in the system MgO–CaO–CO_2–H_2O in presence of chloride or nitrate ions at near surface ambient temperatures. *Applied Geochemistry*, 16-24.

Kristova, P., Hopkinson, L. J. and Rutt, K. J. (2015) The Effect of the Particle Size on the Fundamental Vibrations of the [CO_3^{2-}] Anion in Calcite. *Journal of Physical Chemistry A,* 119, 4891-4897.

Lam, R. S. K., Charnock, J. M., Lennie, A., Meldrum, F. C. (2007) Synthesis-dependant structural variations in amorphous calcium carbonate. *CrystEngComm*, 9, 1226-1236.

Lanas, J. and Alvarez, J. I. (2004) Dolomitic lime: thermal decomposition of nesquehonite. *Thermochimica Acta,* 421, 123-132.

Land, L. S. (1998) Failure to Precipitate Dolomite at 25°C from Dilute Solution Despite 1000-Fold Oversaturation after 32 Years. *Aquatic Geochemistry*, 4, 361-368.

Lane, M. (1999) Midinfrared optical constants of calcite and their relationship to particle size effects in thermal emission spectra of granular calcite. *Journal of Geophysical Research*, 104, 14099-14108.

Langmuir, D. (1965) Stability of carbonates in the system $MgO{-}CO_2{-}H_2O$. *Journal of Geology*, 73, 730-754.

Last, F. M., Last, W. M. and Halden, N. M. (2010) Carbonate microbialites and hardgrounds from Manito Lake, an alkaline, hypersaline lake in the north Great Plains of Canada. *Sedimentary Geology*, 225**,** 34-49.

Le Blond, J. S., Cressey, G., Horwell, C. J., and Williamson, B. J. (2009) A rapid method for quantifying single mineral phases in heterogeneous natural dusts using X-ray diffraction. *Powder Diffraction*, 24, 17-23.

Li, T., Sui, F., Li, F., Cai, Y. and Jin, Z. (2014) Effects of dry grinding on the structure and granularity of calcite and its polymorphic transformation into aragonite. *Powder Technology*, 254, 338-343.

Liebermann, O. (1967) Synthesis of dolomite. *Nature*, 213, 241-245.

Lippmann, F. (1973) Sedimentary carbonate minerals, Springer, Berlin.

Loges, N., Graf, K., Nasdala, L., Tremel, W. (2006) Probing Cooperative Interactions of Tailor-Made Nucleation Surfaces and Macromolecules: A Bioinspired Route to Hollow Micrometer-Sized Calcium Carbonate Particles. *Langmuir*, 22, 3073-3080.

Loste, E., Wilson, R. M., Seshadri, R. and Meldrum, F. C. (2003) The role of magnesium in stabilising amorphous calcium carbonate and controlling calcite morphologies. *Journal of Crystal Growth*, 254, 206-218.

Lou, D., Sun, F., and Li, L. (2007) Study on vibrational modes by group theory and infrared spectra by DFT for calcite crystal. *Chinese Optic Letters*, 5, 370-372.

Martinez-Arkarazo, I., Angulo, M., Zuloaga, O., Usobiaga, A. and Madariaga, J. M. (2007) Spectroscopic characterisation of moonmilk deposits in Pozalagua tourist Cave (Karrantza, Basque Country, North of Spain). *Spectrochimica Acta Part A*, 68, 1058–1064.

Martin-Perez, A., Martin-Garcia, R. and Alonso-Zarza, A. M. (2012) Diagenesis of a drapery speleothem from Castanar Cave: from dissolution to dolomitization. *International Journal of Speleology*, 41, 251-266.

Matousek, P., Towrie, M. and Parker, A. W. (2002) Fluorescence background suppression in Raman spectroscopy using combined Kerr gated and shifted excitation Raman difference technique. *Journal of Raman Spectroscopy*, 33, 238-242.

McKenzie, J. A. and Vasconcelos, G. (2009) Dolomite Mountains and the origin of dolomite rock of which they mainly consist: historical developments and new perspectives. *Sedimentology*, 56, 205-219.

Menzel, H. and Brückner, A. (1930) Studien an kohlensauren Magnesiumsalzen. I. Basische Magnesiumcarbonate. *Zeitschrift für Elektrochemie*, 36, 63–87.

Mignardi, S., De Vito, C., Ferrini, V. and Martin, R. F. (2011) The efficiency of CO_2 sequestration via carbonate mineralization with simulated waste waters of high salinity. *Journal of Hazardous Materials*, 191, 49-55.

Morse, J. W. and Casey, W. H. (1988) Ostwald processes and mineral paragenesis in sediments. *American Journal of Science,* 288, 537-560.

Morse, J. W., Arvidson, R. S. and Lüttge, A. (2007) Calcium Carbonate Formation and Dissolution. *Chemical Reviews*, 107, 342−381.

Mossier-Boss, P. A., Lieberman, S. H. and Newbery, R. (1995) Fluorescence Rejection in Raman Spectroscopy by Shifted-Spectra, Edge Detection, and FFT Filtering Techniques. *Applied Spectroscopy,* 49, 630-638.

Munemoto, T. and Fukushi, K. (2008) Transformation kinetics of monohydrocalcite to aragonite in aqueous solutions. *Journal of Mineralogical and Petrological Sciences,* 103, 345-349.

Nan, Z. D., Shi, Z. Y., Qin, M., Hou, W. G. and Tan, Z. C. (2007) Formation Process and Thermodynamic Properties of Calcite. *Chinese Journal of Chemistry*, *25*, 592—595.

Nashar, B. (1965): Barringtonite – A new hydrous magnesium carbonate from Barrington Tops, New South Wales, Australia. *Mineralogical Magazine,* 34, 370-372.

Nesse, W. D. (2012) Carbonates, Sulfates, Phosphates, Tungstates, Molybdates, and Borates, Introduction to Mineralogy, Oxford University Press, New York, pp 480.

Nishiyama, R., Munemoto, T. and Fukushi, K. (2013) Formation condition of monohydrocalcite from $CaCl_2$–$MgCl_2$–Na_2CO_3 solutions. *Geochimica et Cosmochimica Acta*, 100, 217-231.

Noguchi, N., Shinoda, K. and Masuda, K. (2009) Quantitative analysis of binary mixtures using Raman micro-spectroscopy: Calibration curves for silica and calcium carbonate minerals application to an opaline silica nodule of volcanic origin. *Journal of Mineralogical and Petrological Sciences*, 104, 253-262.

Omelon, C. R., Pollard, W. H. and Marion, G. M. (2001) Seasonal formation of ikaite ($CaCO_3.6H_2O$) in saline spring discharge at Expedition Fiord, Canadian High Arctic: assessing conditional constraints for natural crystal growth. *Geochimica et Cosmochimica Acta,* 65, 1429–1437.

Orlando, A., Lelli, M. and Marini, L. (2012) Production of amorphous hydrated impure magnesium carbonate through ex situ carbonation. *Applied Geochemistry*, 27, 2500–2510.

Pakjamsai, C. and Suwanprateeb, J. (2000) Using FT-Raman spectroscopy for quantitative determination of high filler content in particulated composites. *Journal of Applied Polymer Science*, 78, 1947-1954.

Park, W. K., Ko, S. J., Lee, S. W., Cho, K. H., Ahna, J. W. and Han, C. (2008) Effects of magnesium chloride and organic additives on the synthesis of aragonite precipitated calcium carbonate. *Journal of Crystal Growth*, 310, 2593–2601.

Pecharroman, C. and Iglesias, J. E. (2000) Effect of Particle Shape on IR Reflectance Spectra of Pressed Powders of Anisotropic Materials. *Applied Spectroscopy*, 54, 634-638.

Pellow-Jarman, M., Hendra, P. J., and Lehnert, R. J. (1996) The dependence of Raman signal intensity on particle size for crystal powders. *Vibrational Spectroscopy*, 12, 257-261.

Perchiazzi, N., Merlino, S. (2006) The malachite-rosasite group: crystal structures of glaukosphaerite and pokrovskite. *European Journal of Mineralogy,* 18, (6) 787-792.

Power, I. M., Wilson, S. A., Thom, J. M., Dipple, G. M. and Southam, G. (2007) Biologically induced mineralization of dypingite by cyanobacteria from an alkaline wetland near Atlin, British Columbia, Canada. *Geochemical Transactions,* 8, 13.

Power, I. M., Wilson, S. A., Thom, J. M., Dipple, G. M., Gabites, J. E. and Southam, G. (2009) The hydromagnesite playas of Atlin, British Columbia, Canada: A biogeochemical model of CO_2 sequestration. *Chemical Geology*, 260, 286-300.

Queralt, I., Juliá, R., Plana, F. and Bischoff, J. L. (1997) A hydrous Ca-bearing magnesium carbonate from playa lake sediments, Salines Lake, Spain. *American Mineralogist*, 82, 812-819.

Raade, G. (1970) Dypingite, a new hydrous basic carbonate of magnesium, from Norway. *American Mineralogist*, 55, 1457-1465.

Radha, A. V., Forbes, T. Z., Killian, C. E., Gilbert, P. U. P. A. and Navrotsky, A. (2010) Transformation and crystallization energetics of synthetic and biogenic amorphous calcium carbonate. *Proceedings of the National Academy of Sciences of the United States of America*, 107, 16438–16443.

Raz, S., Hamilton, P. C., Wilt, F. H., Weiner S. and Addadi, L. (2003) The Transient Phase of Amorphous Calcium Carbonate in sea Urchin larval spiculas: The Involvement of Proteins and Magnesium Ions in Its Formation and Stabilization. *Advanced Functional Materials*, 13, 480-486.

Reddy, M. M. and Wang, K. K. (1980) Crystallization of calcium carbonate in the presence of metal ions. *Journal of Crystal Growth*, 50, 470-480.

Rinnan, Å., van den Berg, F., Balling Engelsen, S. (2009) Review of the most common pre-processing techniques for near-infrared spectra. *Trends in Analytical Chemistry*, 28, 1202-1222.

Rividi, N., van Zuilen, M., Philippot, P., Menez, B., Godard, G. and Poidaz, E. (2010), Calibration of Carbonate Composition Using Micro-Raman Analysis: Application to Surface Exploration. *Astrobiology*, 10, 293-309.

Roberts, J. A., Bennett, P. C., Gonzalez, L. A., Macpherson, G. L. and Miliken, K. L. (2004) Microbial precipitation of dolomite in methanogenic groundwater. *Geology*, 32,

277-280.

Rolland, P., Carlino, V. and Vane, R. (2004) Improved Carbon Analysis with Evactron Plasma Cleaning. *Microscopy and Microanalysis*, Volume / Supplement S02, 964-965.

RRUFF database - Chlorartinite (ID no. R060878), available at http://rruff.info/chlorartinite, (Accessed: 12th February 2014).

Russell, M. J., Ingham, J. K., Zedef, V., Maktav, D., Sumar, F., Hall, A. J. and Fallick, A. E. (1999) Search for signs of ancient life on Mars: expectations from hydromagnesite microbialites, Salda Lake, Turkey. *Journal of the Geological Society of London,* 156, 869-888.

Rysgaard, S., Søgaard, D. H., Cooper, M., Pucko, M., Lennert, K., Papakyriakou, T. N., Wang, F., Geilfus, N. X., Glud, R. N., Ehn, J., McGinnnis, D. F., Attard, K., Sievers, J., Deming, J. W. and Barber, D. (2012) Ikaite crystal distribution in Arctic winter sea ice and implications for CO_2 system dynamics. *The Cryosphere Discussions*, 6, 5037–5068.

Salisbury, J. W. and Eastes, J. W. (1985) The Effect of Particle Size and Porosity on Spectral Contrast in the Mid-Infrared. *Icarus*, 64, 586-588.

Salisbury, J. W., Hapke, B. and Eastes, J. W. (1987) Usefulness of Weak Bands in Midinfrared Remote Sensing of Particulate Planetary Surfaces. *Journal of Geophysical Research*, 92, 702-710.

Salisbury, J. W. and Wald, A. (1992) The Role of Volume Scattering in Reducing Spectral Contrast of Reststrahlen Bands in Spectra of Powdered Minerals. *Icarus*, 96, 121-128.

Sanchez-Roman, M., Vasconcelos, C., Warthmann, R., Rivadeneyra, M. and McKenzie, J. A. (2009) Microbial dolomite precipitation under aerobic conditions: results from Brejo do Espinho Lagoon (Brazil) and culture experiments. *International Association of Sedimentologists Special Publication*, 41, 167-178.

Scheetz, B. E. and White, W. B. (1977) Vibrational spectra of the alkaline earth double carbonates. *American Mineralogist*, 62, 36-50.

Schrader, B., Hoffmann, A. and Keller, S. (1991) Near-infrared Fourier transform Raman spectroscopy: facing absorption and background. *Spectrochimica Acta Part A*, 47, 1135-1148.

Selleck, B.W., Carr, P.F. and Jones, B.G (2007) A review and synthesis of glendonites (pseudomorphs after ikaite) with new data: assessing applicability as recorders of ancient coldwater conditions. *Journal of Sediment Research*, 77, 980–991.

Serna, C. J., Ocafia, M. and Iglesias, J. E. (1987) Optical properties of α-Fe_2O_3 microcrystals in the infrared. *Journal of Physics C: Solid State Physics*, 20, 473-484.

Shayan, A. (1984) Strontium in huntites from Geelong and Deer Park, Victoria, Australia. *American Mineralogist*, 69, 528-530.

Sherazi, S. T. H., Ali, M. and Mahesar, S. A. (2011) Application of Fourier-transform infrared (FT-IR) transmission spectroscopy for the estimation of roxithromycin in pharmaceutical formulations. *Vibrational Spectroscopy*, 55, 115–118.

Smith, E. And Dent, G. (2008) Modern Raman Spectroscopy, A Practical Approach, Wiley, Chichester, pp 210.

Stamatakis, M. G. (1995) Occurrence and genesis of huntite-hydromagnesite assemblages, Kozani, Greece: important new white fillers and extenders. Transactions of the Institution of mining and metallurgy section B, *Applied Earth Science*, 104, 179-186.

Stanger, G., (1986) The Hydrologeology of the Oman Mountains. PhD dissertation, Department of Earth Sciences, The Open University, Great Britain.

Stephenson, G. A., Forbes, R. A. and Reutzel-Edens, S. M. (2001) Characterization of the solid state: quantitative issues, *Advanced Drug Delivery Reviews*, 48, 67-90.

Suzuki, J. and Ito, M. (1973) A new magnesium carbonate hydrate mineral, $Mg_5(CO_3)_4(OH)_2 \cdot 8H_2O$, from Yoshikawa, Aichi Prefecture, Japan. *Journal of the Japanese Association of Mineralogists, Petrologists and Economic Geologists,* 68, 353–361.

Tai, C. Y. and Chen, F. B. (1998) Polymorphism of $CaCO_3$ Precipitated in a Constant-Composition Environment, *AIChE Journal*, 44, 1790-1798.

Taylor, G. F. (1975) The occurrence of monohydrocalcite in two small lakes in the south-east of South Australia. *American Mineralogist*, 60, 690-697.

Terada, T., Yamabi, S. and Imai, H. (2003) Formation process of sheets and helical forms consisting of strontium carbonate fibrous crystals with silicate. *Journal of Crystal Growth*, 253, 435–444.

Tlili, M. M., Amor, M. B., Gabrielli, C., Joiret, G. and Rousseau, P. (2001) Characterization of $CaCO_3$ hydrates by micro-Raman spectroscopy. *Journal of Raman Spectroscopy*, 33, 10-16.

Tsukerblat, B. S. (2006) Group Theory in Chemistry and Spectroscopy: A Simple Guide to Advanced Usage, Dover Publications, USA, pp 464.

Uebo, K., Yamazaki, R. and Yoshida, K. (1992) Precipitation mechanism of calcium carbonate fine particles in a three-phase reactor. *Advanced Powder Technology*, 3, 71-79.

Urmos, J., Sharma, S. K. and Mackenzie, F. T. (1991) Characterization of some biogenic carbonates with Raman spectroscopy. *American Mineralogist,* 76, 641-646.

Vagenas, N. V. and Kontoyannis, C. G. (2003) A methodology for quantitative determination of minor components in mineral based on FT-Raman spectroscopy The case of calcite in dolomitic marble. *Vibrational Spectroscopy*, 32, 261-264.

Vagenas, N. V., Gatsouli, A. and Kontoyannis, C. G. (2003) Quantitative analysis of synthetic calcium carbonate polymorphs using FT-IR spectroscopy. *Talanta*, 59, 831-836.

Vandenabeele, P., Jehlicka, J., Vitek, P. and Edwards, H.G.M. (2012) On the definition of Raman spectroscopic detection limits for the analysis of biomarkers in solid matrices. *Planetary and Space Science*, 62, 48-54.

Vandenabeele, P., Edwards, H. G. M. and Jehlicka, J. (2014) The role of mobile instrumentation in novel applications of Raman spectroscopy: archaeometry, geosciences, and forensics. *Chemical Society Reviews*, 43, 2628-2649.

Vasconcelos, C., McKenzie, J. A., Bernasconi, S., Grujic, D. and Tien, A. J. (1995) Microbial mediation as a possible mechanism for natural dolomite formation at low temperatures. *Nature*, 377, 220-222.

Vasconcelos, C. and McKenzie, J. A. (1997) Microbial mediation of modern dolomite precipitation and diagenesis under anoxic conditions (Lagoa Vermelha, Rio De Janeiro, Brazil). *Journal of Sedimentary Research*, 67, 378-390.

Vincent, R. K. and Hunt, G. R. (1968) Infrared reflectance from mat surfaces. *Applied Optics*, 7, 53-59.

Vitek, P., Ali, E. M. A., Edwards, H. G. M., Jehlicka, J., Cox, R. and Page, K. (2012) Evaluation of portable Raman spectrometer with 1064nm excitation for geological and forensic applications. *Spectrochimica Acta Part A*, 86, 320-327.

Walling, E. M., Rock, P. A. and Casey, W. H. (1995) The Gibbs energy of formation of huntite, $CaMg_3(CO_3)_4$, at 298 K and 1 bar from electrochemical cell measurements. *American Mineralogist*, 80, 355-360.

Warthmann, R., van Lith, Y., Vasconcelos, C., McKenzie, J. A. and Karpoff, A. M. (2000) Bacterially induced dolomite precipitation in anoxic culture experiments. *Geology*, 28, 1091-1094.

Wehrmeister, U., Soldati, A. L., Jacob, D. E. and Häger, T. (2010) Raman spectroscopy of synthetic, geological and biological vaterite: a Raman spectroscopic study. *Journal of Raman Spectroscopy*, 41, 193-201.

Wells, R. C. (1915) The solubility of magnesium carbonate in natural waters. *Journal of the American Chemical Society, 37*, 1704-1707.

White, W. B. (1974) The carbonate minerals. In Farmer V.C., The Infrared spectra of minerals, pp 227-282, Mineralogical Society Monograph 4, London.

Xiong, Y. and Lord, A. S. (2008) Experimental investigations of the reaction path in the MgO-CO_2-H_2O system in solutions with various ionic strengths, and their application to nuclear waste isolation. *Applied Geochemistry,* 23, 1634-1639.

Zachmann, D. (1989) Mg-carbonate deposits in freshwater environments. In Möller, P., ed. Magnesite: geology, mineralogy, geochemistry, formation of Mg-carbonates. Monograph Series on Mineral Deposits. Vol 28. Berlin Bornträger, p. 61-94.

Zhang, Z., Zheng Y., Ni Y., Liu Z., Chen, J. and Liang, X. (2006) Temperature and pH dependent morphology and FT-IR analysis of magnesium carbonate hydrates. *Journal of Physical Chemistry*, 110, 12969-12973.

Zhao, L., Sang, L., Chen, J., Ji, J. and Teng, H. H. (2010) Aqueous carbonation of natural brucite: relevance to CO_2 sequestration. *Environmental Science & Technology*, 44, 406-411.

Appendices

Table of Contents

Appendix C - Representative examples of analyses from Carbonate mineral paragenesis and reaction kinetics in the system MgO-CaO-CO_2-H_2O in presence of chloride or nitrate ions at near surface ambient temperatures.

Appendix A - Representative examples of analyses from Quantification of natural carbonates

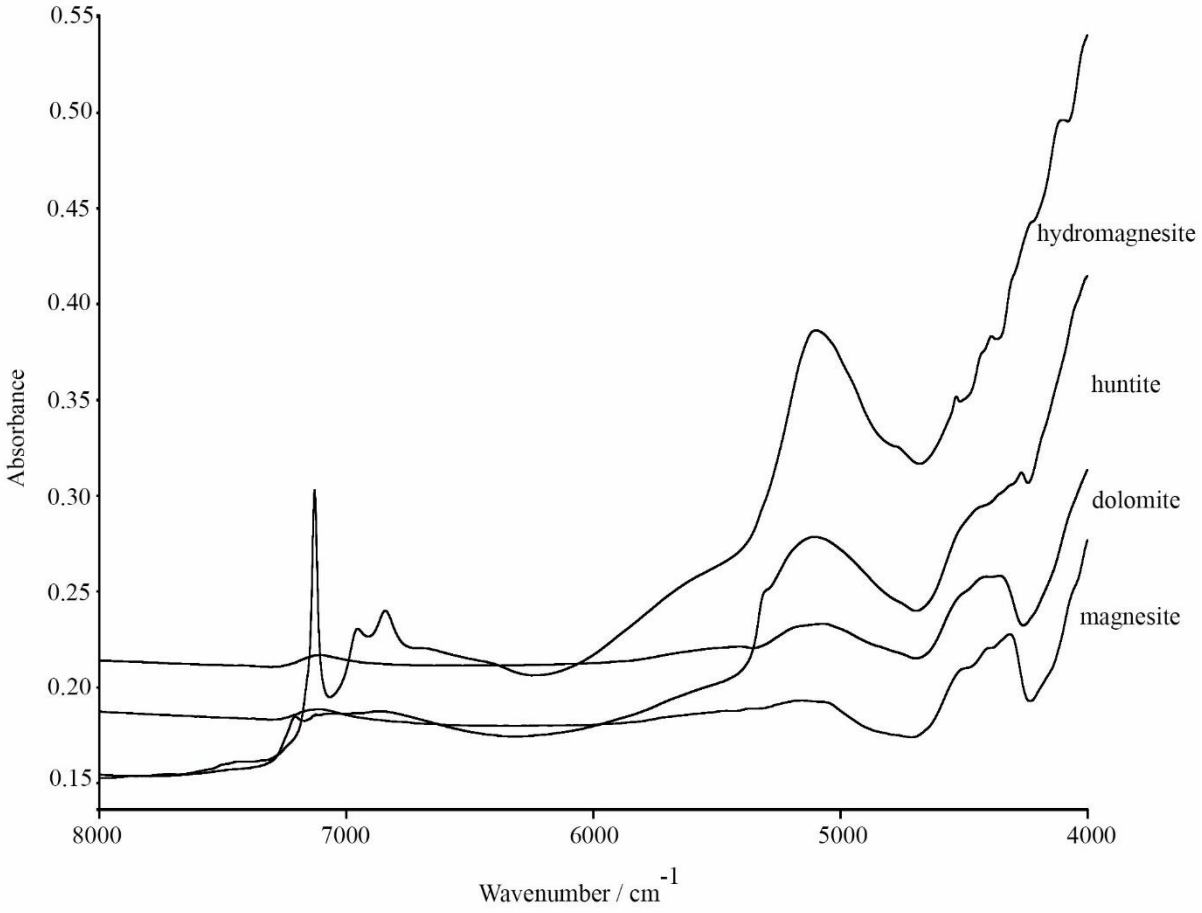

Figure A.1: Near-infrared spectra of mineral standards showing sloping baselines before any data treatment. Spectra shown here are averaged for clarity.

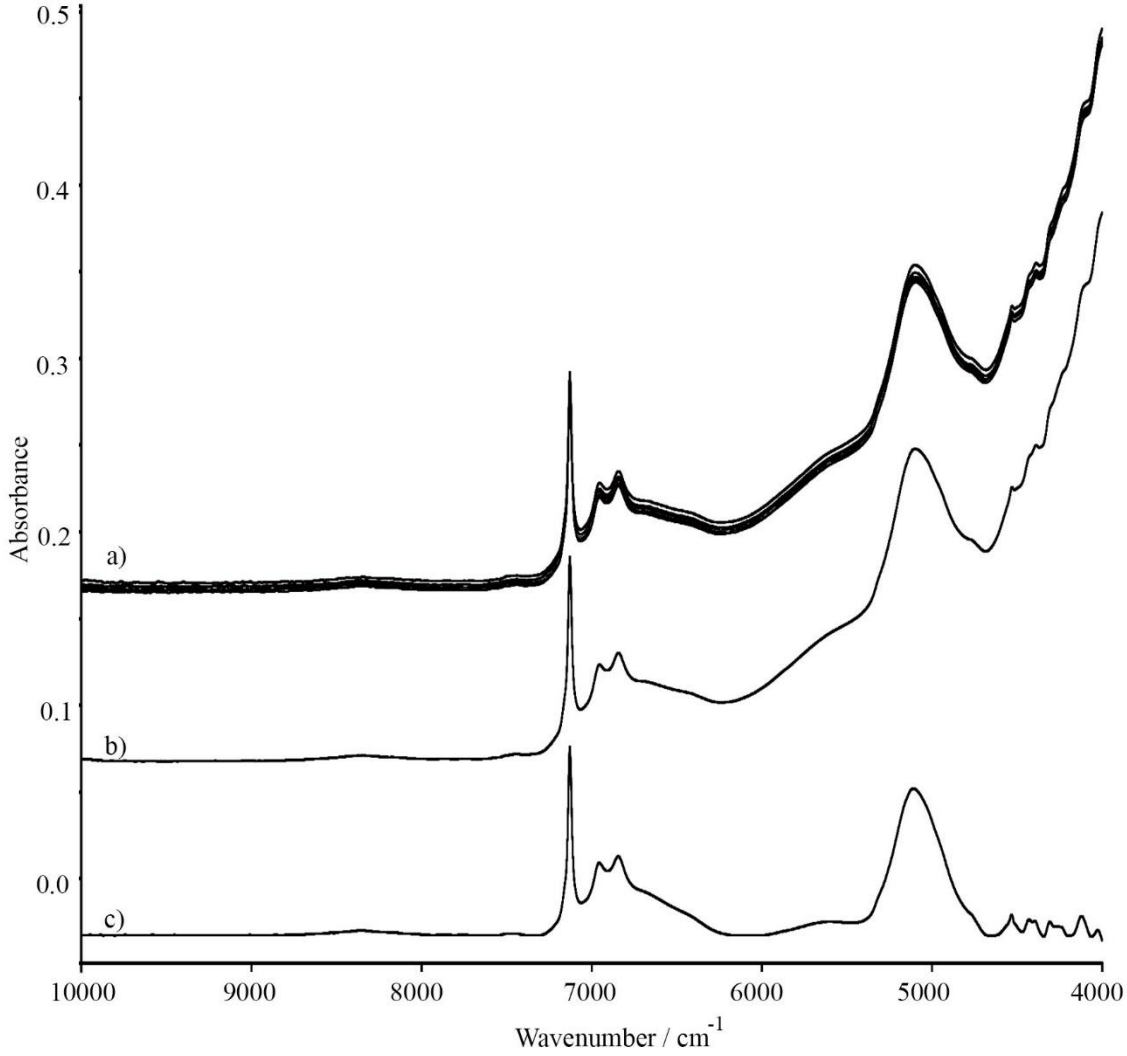

Figure A.2: Near infrared spectra of sample 1 (mixture contains 15.06 % of huntite, 64.92 % hydromagnesite, 12.07 % dolomite and 7.96 % magnesite); (a) raw data of six measured replicates, (b) average measurement (spectrum offset for clarity), (c) spectrum after baseline correction (spectrum offset for clarity).

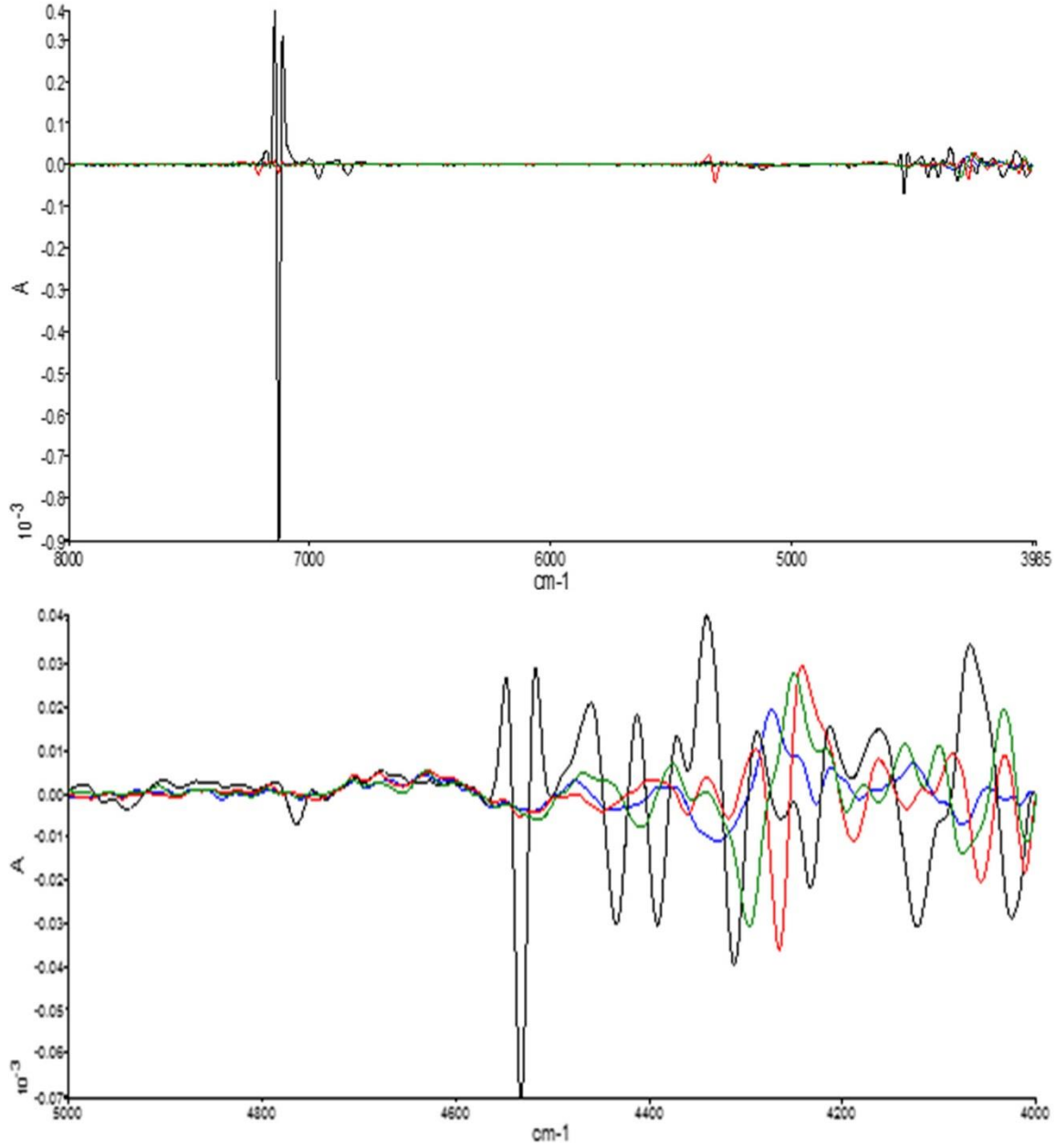

Figure A.3 : Near-infrared spectra of mineral standards shown as second derivatives (9 points). Spectra are shown in ranges 8000-4000 cm^{-1} (top) and 5000-4000 cm^{-1} (bottom). Individual minerals are colour coded - hydromagnesite (black), huntite (red), dolomite (green) and magnesite (blue).

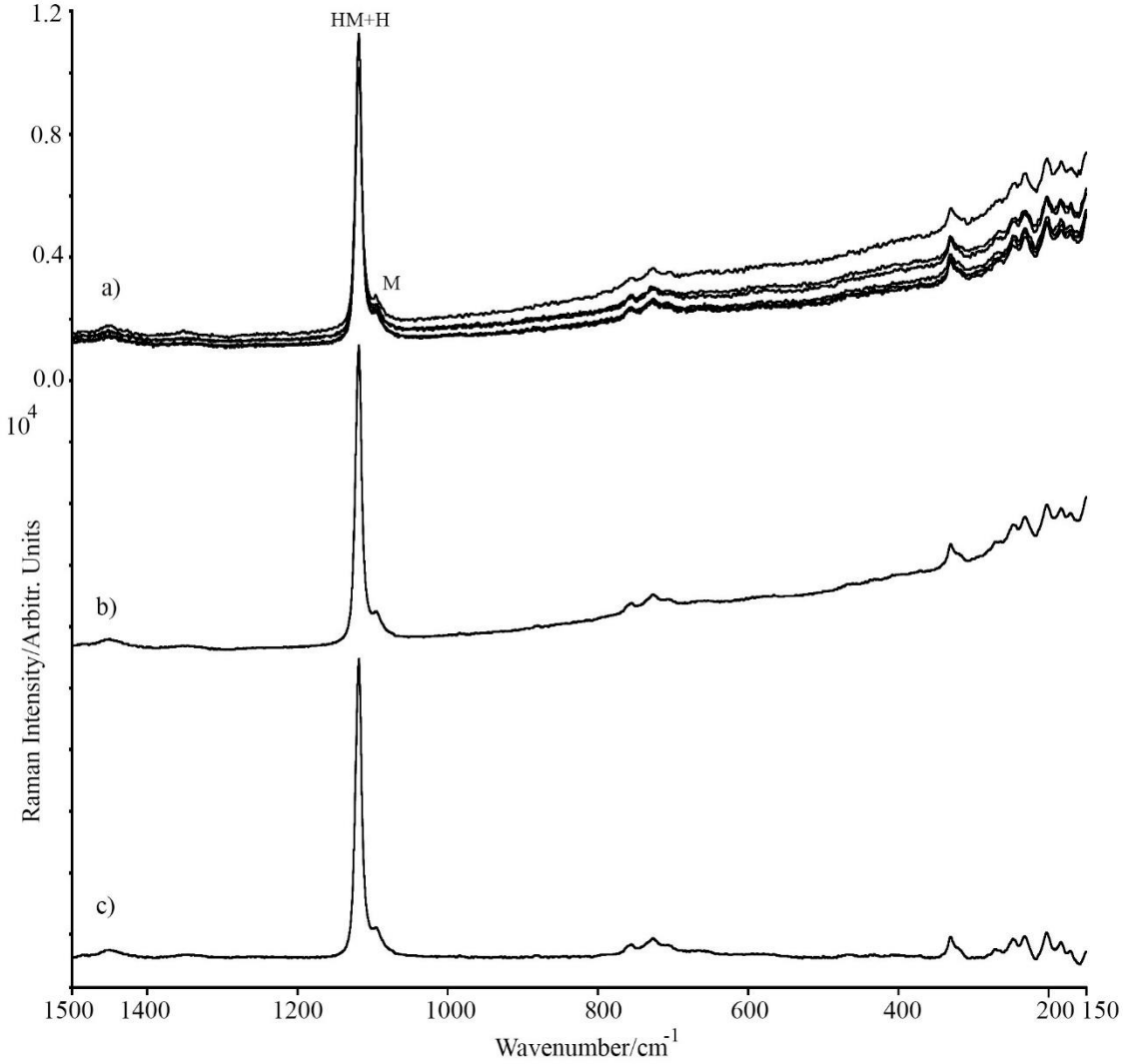

Figure A.4: Raman spectra of sample 17 (mixture contains 2.12 % magnesite, 4.02 % huntite and 93.86 % hydromagnesite); (a) raw data of six measured replicates, (b) average measurement (spectrum offset for clarity), (c) spectrum after baseline correction (spectrum offset for clarity). Coding of mineral phases is as follows –M (magnesite), HM (hydromagnesite), H (huntite).

Group of measurement	Peak height at 1122 cm^{-1} [arbitr. units]	Peak height at 1118 cm^{-1} [arbitr. units]	Peak height at 1097 cm^{-1} [arbitr. units]	Peak height at 1092 cm^{-1} [arbitr. units]
A	10000	17889	16132	2099
B	8130	15059	16347	1514
C	10066	17785	15310	1601
D	9447	17685	15249	1864
E	10642	18999	16529	2232
F	9320	18282	17720	2215
Average	9600.8	17616.5	16214.5	1920.8
Standard deviation	863.2	1341.8	910.0	311.8
Relative standard deviation [%]	9.0	7.6	5.6	16.2
Average relative standard deviation [%]	**9.6**			

Table A.1 Repeatability of the Raman spectroscopic measurement and data manipulation. Sample 1 (containing 15.06 % of huntite, 64.92 % hydromagnesite, 12.07 % dolomite and 7.96 % magnesite) was repeatedly measured, spectra manipulated and curve fitted to calculate error on repeatability. [1]

[1] To evaluate repeatability of the spectroscopic measurements and data manipulation, replicate measurements were taken on one sample to provide six groups of six measurements. Spectra in each group were averaged, baseline corrected, deconvoluted, peak fitted and compared. The relative standard error for quaternary mixtures for these six measurements was calculated to be on average 9.6 % on v_1 peak height that was used in the monovariable model. This error includes potential effects of mixture inhomogeneities.

Independent set 1								
	composition				calculated value			
sample	D [%]	M [%]	H [%]	HM [%]	D [%]	M [%]	H [%]	HM [%]
9	6.01	14.01	69.97	10.01	7.23	12.87	73.48	5.48
3	12.05	0.00	0.00	87.95	10.13	-0.71	0.09	89.04
2	0.00	5.02	92.96	2.02	0.22	5.58	84.49	1.86
11	7.87	12.09	70.24	9.80	8.10	11.71	69.98	8.95
14	0.00	0.00	50.29	49.71	-0.65	0.24	44.36	49.19
	total error				error on value			
9	1.22	1.14	3.51	4.53	20.33	8.14	5.02	45.27
3	1.92	0.71	0.09	1.09	15.93	N/A	N/A	1.24
2	0.22	0.56	8.47	0.16	N/A	11.12	9.11	7.87
11	0.23	0.38	0.26	0.86	2.90	3.14	0.37	8.72
14	0.65	0.24	5.93	0.52	N/A	N/A	11.79	1.05
	average total error set 1 [%]			**1.63**	average error on value [%]			**10.13**

Table A.2: Assessment of quantitative calibration model (PCR+ with SNV applied) for quaternary mixtures measured by RS - Independent validation set 1 with calculated total error and error on value. (N/A denotes not applicable - Error on value was not possible to calculate for zero values due to divisions by zero).

Independent set 2								
	composition				calculated value			
sample	D [%]	M [%]	H [%]	HM [%]	D [%]	M [%]	H [%]	HM [%]
7	15.99	0.00	84.01	0.00	12.42	1.38	80.57	0.61
4	8.02	11.92	50.07	29.99	7.95	11.95	50.97	30.10
1	12.07	7.96	15.06	64.92	12.73	7.80	11.33	67.75
19	0.00	0.00	100.00	0.00	-0.01	0.92	93.24	5.10
13	0.00	0.00	25.79	74.21	-0.35	0.09	30.58	69.12
	total error				error on value			
7	3.57	1.38	3.44	0.61	22.33	N/A	4.09	N/A
4	0.07	0.03	0.90	0.11	0.92	0.25	1.80	0.37
1	0.66	0.16	3.73	2.83	5.47	1.96	24.77	4.36
19	0.01	0.92	6.76	5.10	N/A	N/A	6.76	N/A
13	0.35	0.09	4.79	5.09	N/A	N/A	18.57	6.86
	average total error set 2 [%]			**2.03**	average error on value [%]			**7.58**

Table A.3: Assessment of quantitative calibration model (PCR+ with SNV applied) for quaternary mixtures measured by RS - Independent validation set 2 with calculated total error and error on value. (N/A denotes not applicable - Error on value was not possible to calculate for zero values due to divisions by zero).

Independent set 3								
	composition				calculated value			
sample	D [%]	M [%]	H [%]	HM [%]	D [%]	M [%]	H [%]	HM [%]
12	4.00	6.01	0.00	89.99	4.82	6.43	-1.39	92.84
8	0.00	16.09	0.00	83.91	2.73	18.40	0.70	83.33
6	14.03	2.00	62.04	21.93	10.64	1.91	66.42	16.63
15	14.93	4.27	0.00	80.80	14.07	4.49	0.50	81.91
16	5.98	15.98	78.04	0.00	6.47	15.00	83.29	0.40
	total error				error on value			
12	0.82	0.42	1.39	2.85	20.53	7.05	N/A	3.17
8	2.73	2.31	0.70	0.58	N/A	14.36	N/A	0.69
6	3.39	0.09	4.38	5.30	24.16	4.50	7.06	24.17
15	0.86	0.22	0.50	1.11	5.76	5.11	N/A	1.37
16	0.49	0.98	5.25	0.40	8.19	6.13	6.73	N/A
	average total error set 3 [%]			**1.74**	average error on value [%]			**9.27**

Table A.4: Assessment of quantitative calibration model (PCR+ with SNV applied) for quaternary mixtures measured by RS - Independent validation set 3 with calculated total error and error on value (N/A denotes not applicable - Error on value was not possible to calculate for zero values due to divisions by zero).

Independent set 4								
	composition				calculated value			
sample	D [%]	M [%]	H [%]	HM [%]	D [%]	M [%]	H [%]	HM [%]
10	10.01	9.96	39.94	40.09	10.72	10.01	39.14	40.02
5	2.02	3.96	32.10	61.93	1.42	3.98	35.02	59.73
17	0.00	2.12	4.02	93.86	-1.05	1.15	8.04	91.32
18	13.85	5.13	10.95	70.08	14.54	3.41	9.46	69.47
20	0.00	0.00	0.00	100.00	-1.13	-1.39	0.00	97.38
	total error				error on value			
10	0.71	0.05	0.80	0.07	7.09	0.50	2.00	0.17
5	0.60	0.02	2.92	2.20	29.75	0.61	9.10	3.55
17	1.05	0.97	4.02	2.54	N/A	45.66	100.00	2.71
18	0.69	1.72	1.49	0.61	4.98	33.47	13.63	0.87
20	1.13	1.39	3.88	2.62	N/A	N/A	N/A	2.62
	average total error set 4 [%]			**1.47**	average error on value [%]			**16.05**

Table A.5: Assessment of quantitative calibration model (PCR+ with SNV applied) for quaternary mixtures measured by RS - Independent validation set 4 with calculated total error and error on value. (N/A denotes not applicable - Error on value was not possible to calculate for zero values due to divisions by zero).

	average total error [%]	average error on value [%]
Independent set 1	1.63	10.13
Independent set 2	2.03	7.58
Independent set 3	1.74	9.27
Independent set 4	1.47	16.05
Average for all sets	**1.72**	**10.76**

Table A.6: Summary of independent validation sets 1 to 4 (Tables A.2, A.3, A.4 and A.5)

Appendix B - Representative examples analyses from the effect of the particle size on the fundamental vibrations of the [$CO3^{2-}$] anion in calcite.

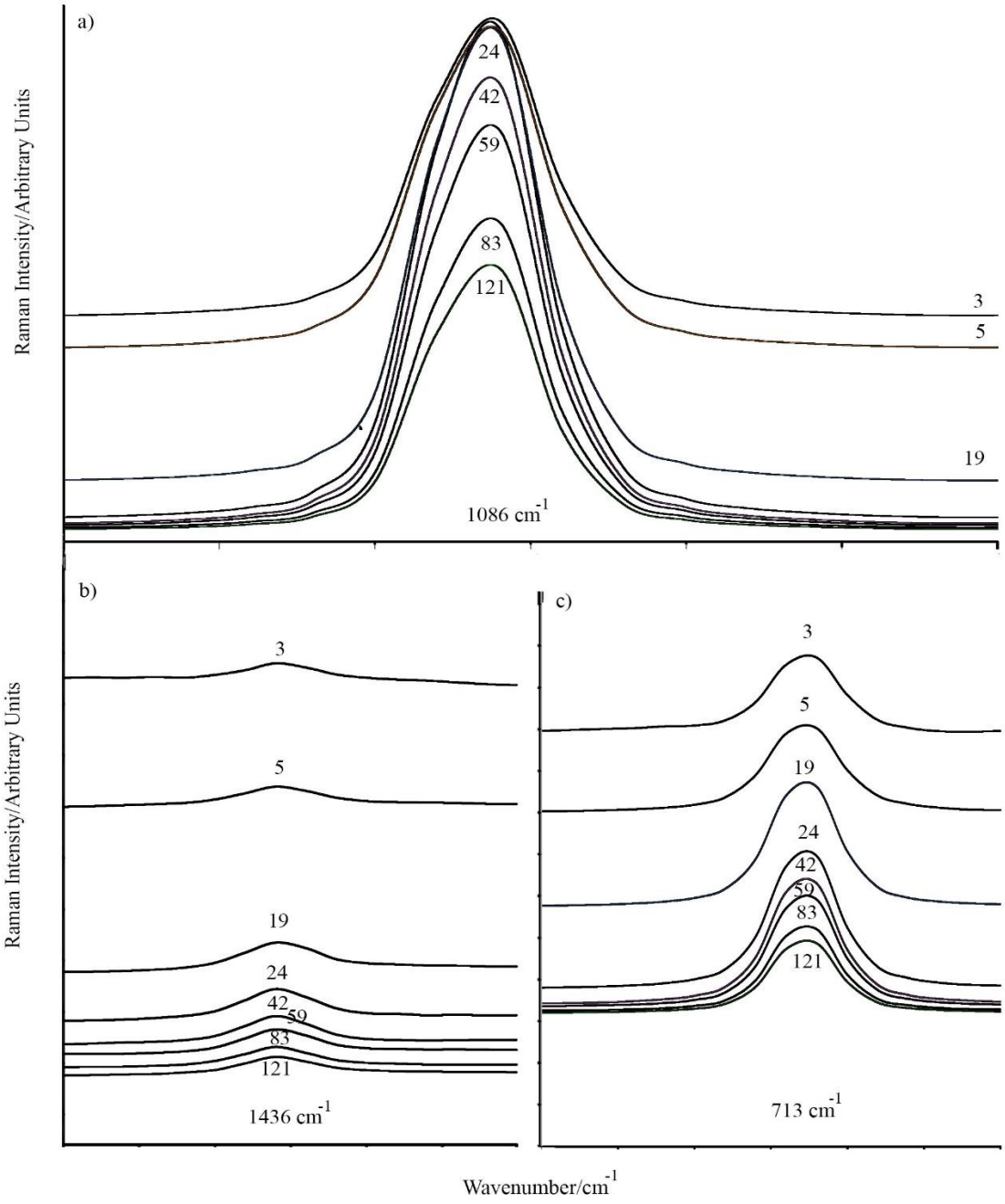

Figure B.1: Raman internal modes of calcite changing in intensity with decreasing particle size. Curves are shown with particle size decreasing from bottom to top (121 µm, 83 µm, 59 µm, 42 µm, 24 µm, 19 µm, 5 µm and 3 µm). a) symmetrical stretch ν_1 (1086 cm^{-1}); b) asymmetric stretch ν_3 (1436 cm^{-1}); c) in plane bending ν_1 (713 cm^{-1}).

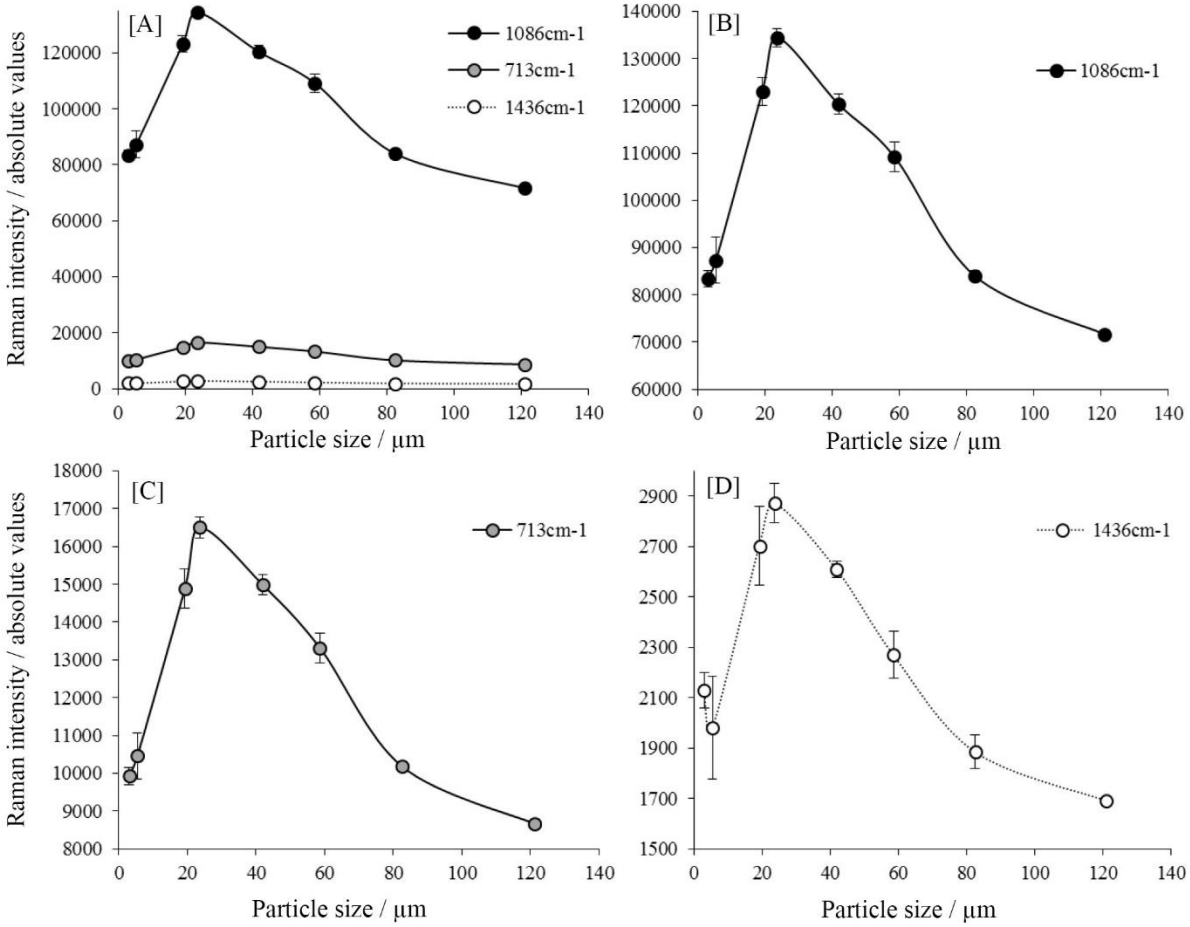

Figure B.2: Raman intensity (peak heights in absolute values) plotted against grain size (modal sizes in microns). [A] Summary of internal modes ν_1 (1086 cm^{-1}), ν_4 (713 cm^{-1}) and ν_3 (1436 cm^{-1}); [B] detail of ν_1 (1086 cm^{-1}); [C] detail of ν_4 (713 cm^{-1}); [D] detail of ν_3 (1436 cm^{-1}).

Appendix C - Representative examples of analyses from Carbonate mineral paragenesis and reaction kinetics in the system MgO-CaO-CO_2-H_2O in presence of chloride or nitrate ions at near surface ambient temperatures.

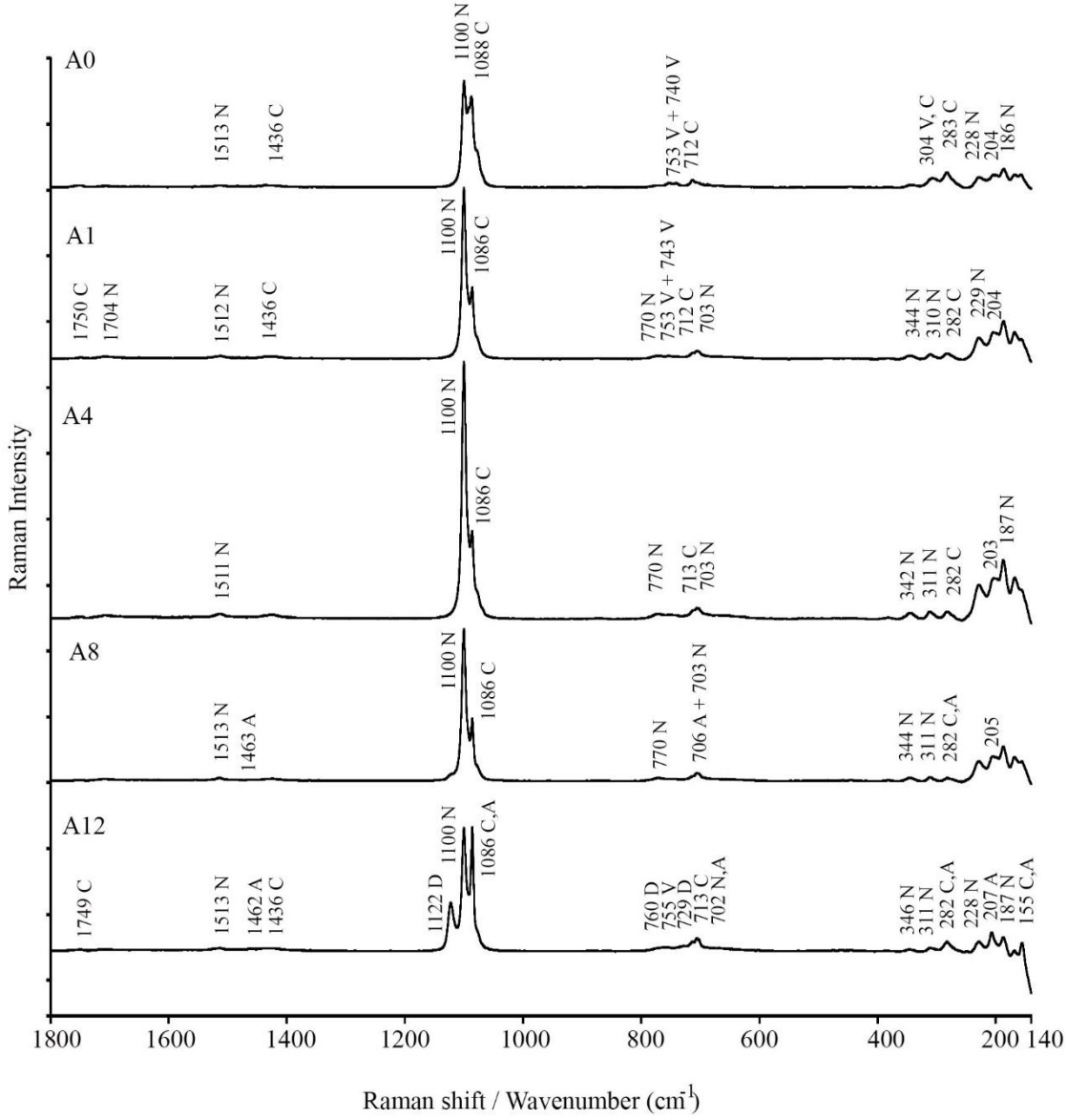

Figure C.1: Raman spectra of experiment A series from time 0 to 12 days measured over range 1800-150 cm^{-1}. Coding of mineral phases is as follows – A (aragonite), C (calcite), D (dypingite), N (nesquehonite), V (vaterite).

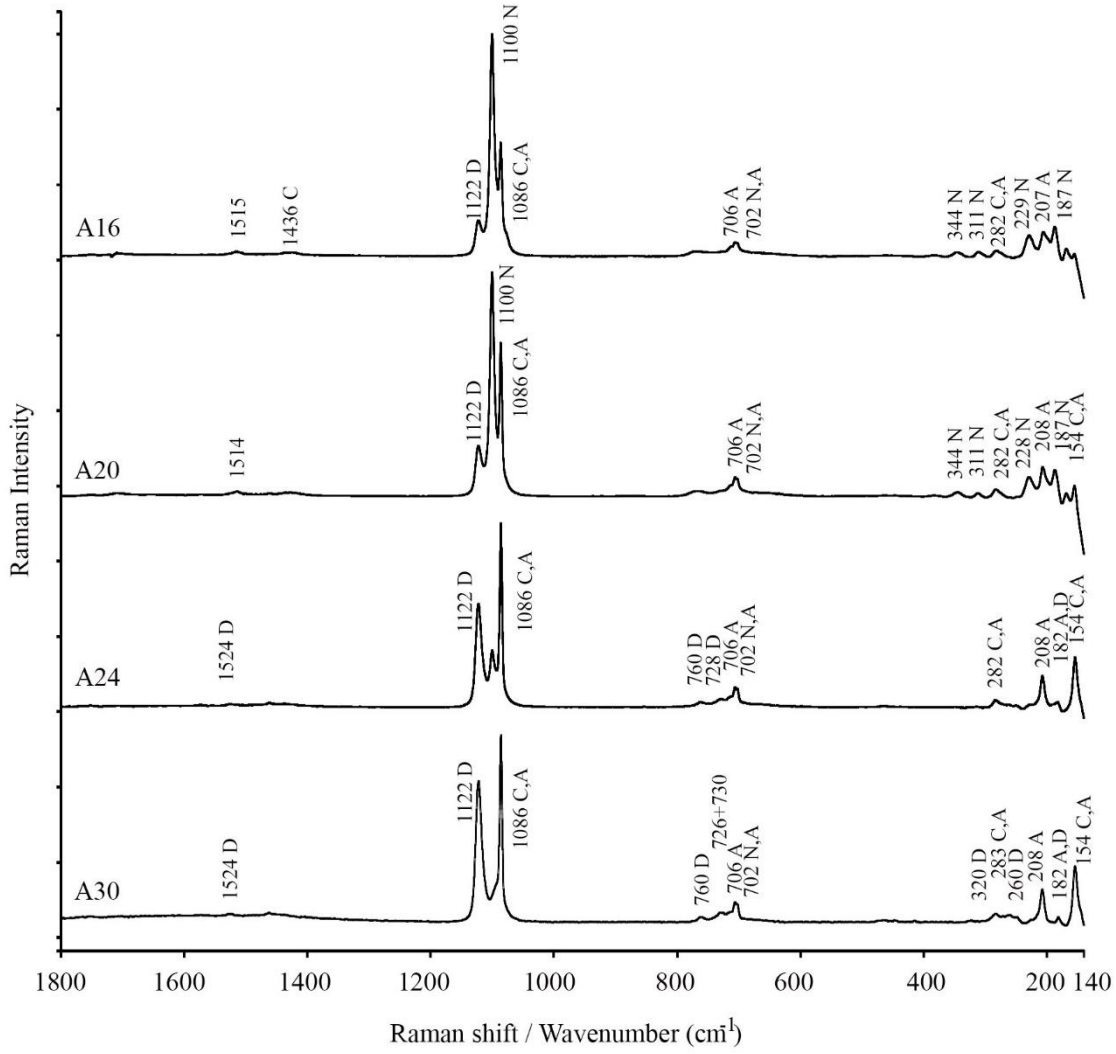

Figure C.2: Raman spectra of experiment A series from 16 to 30 days measured over range 1800-150 cm^{-1}. Coding of mineral phases is as follows – A (aragonite), C (calcite), D (dypingite), N (nesquehonite), V (vaterite).

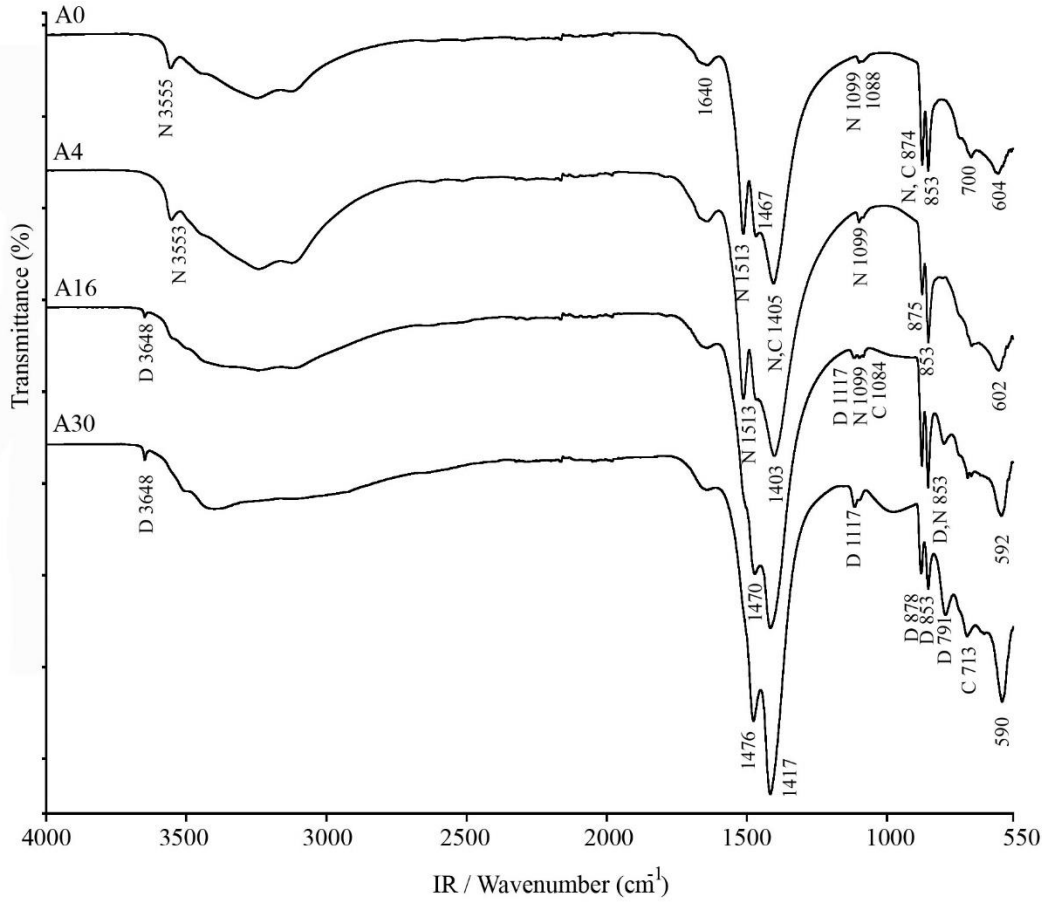

Figure C.3: Representative FT-IR spectra from experiment [A] in the range 4000-550 cm^{-1}. FT-IR spectra of A0 and A4 samples containing nesquehonite with OH band at 3555 cm^{-1}. Coding of mineral phases is as follows – C (calcium carbonate), D (dypingite), N (nesquehonite).[2]

[2] Calcite IR spectrum shows 1393 cm^{-1} with a shoulder at 1403 cm^{-1} (ν_3), 871 cm^{-1} with a subordinate weak peak at 847 cm^{-1} (ν_2), 712 cm^{-1} (ν_4) (Figure 3.5) Aragonite IR bands are found at 1085 cm^{-1} (ν_1), 875/870 cm^{-1} (ν_2), 1465 cm^{-1} (ν_3) (also reported at 1490 cm^{-1}), 712/699 cm^{-1} (ν_4). Nesquehonite IR bands 1097 cm^{-1} (ν_1), 852 cm^{-1} (ν_2), 1518/1469/1415 cm^{-1} (ν_3), 700 and 603 cm^{-1} (Huang and Kerr 1960; White 1974). The calcium carbonate phases showed spectral overlaps and therefore e.g. vaterite could not be distinguished by IR due to its low concentration and spectral overlap with calcite peaks.

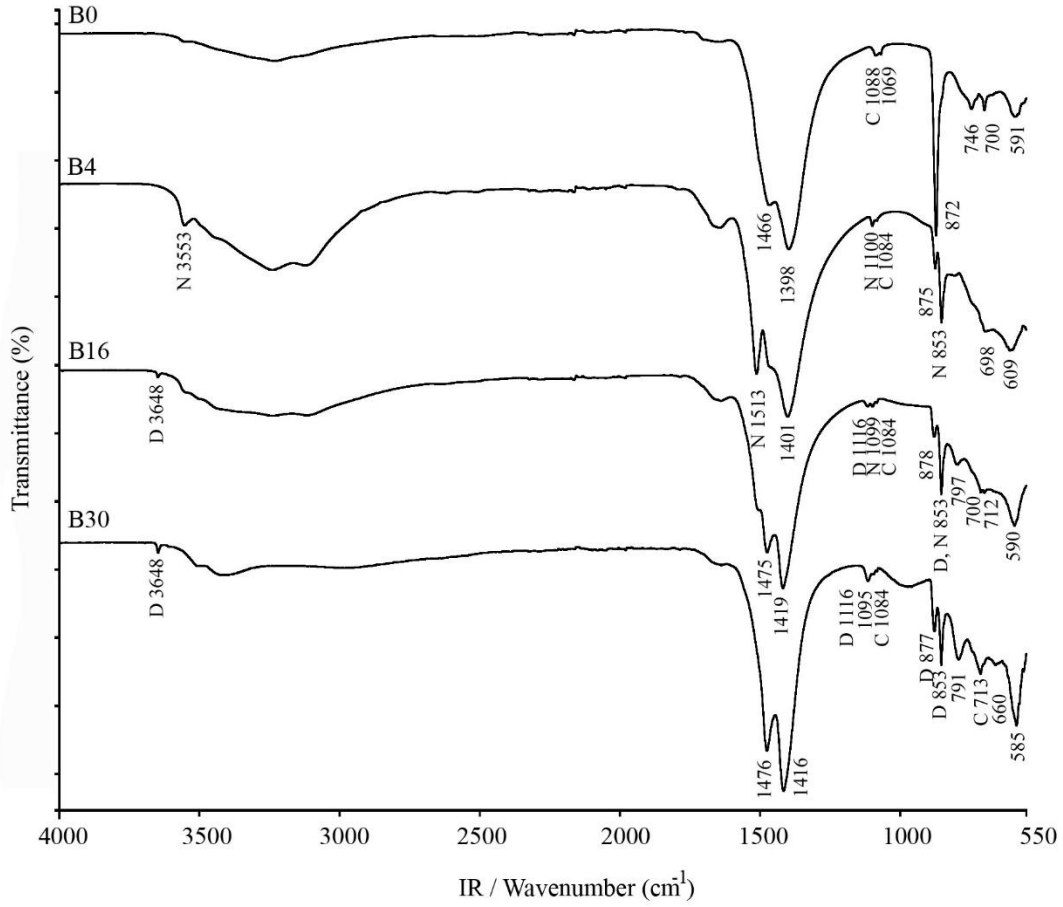

Figure C.4: Representative FT-IR spectra from experiment [B] in the range 4000-550 cm^{-1}. FT-IR spectrum of B4 sample containing nesquehonite with OH band at 3555 cm^{-1}. Coding of mineral phases is as follows – C (calcium carbonate), D (dypingite), N (nesquehonite).[3]

[3] Calcite IR spectrum shows 1393 cm^{-1} with a shoulder at 1403 cm^{-1} (ν_3), 871 cm^{-1} with a subordinate weak peak at 847 cm^{-1} (ν_2), 712 cm^{-1} (ν_4) (Figure 3.5) Aragonite IR bands are found at 1085 cm^{-1} (ν_1), 875/870 cm^{-1} (ν_2), 1465 cm^{-1} (ν_3) (also reported at 1490 cm^{-1}), 712/699 cm^{-1} (ν_4). Nesquehonite IR bands 1097 cm^{-1} (ν_1), 852 cm^{-1} (ν_2), 1518/1469/1415 cm^{-1} (ν_3) (Huang and Kerr 1960; White 1974). The calcium carbonate phases showed spectral overlaps and therefore e.g. vaterite could not be distinguished by IR due to its low concentration and spectral overlap with calcite peaks.

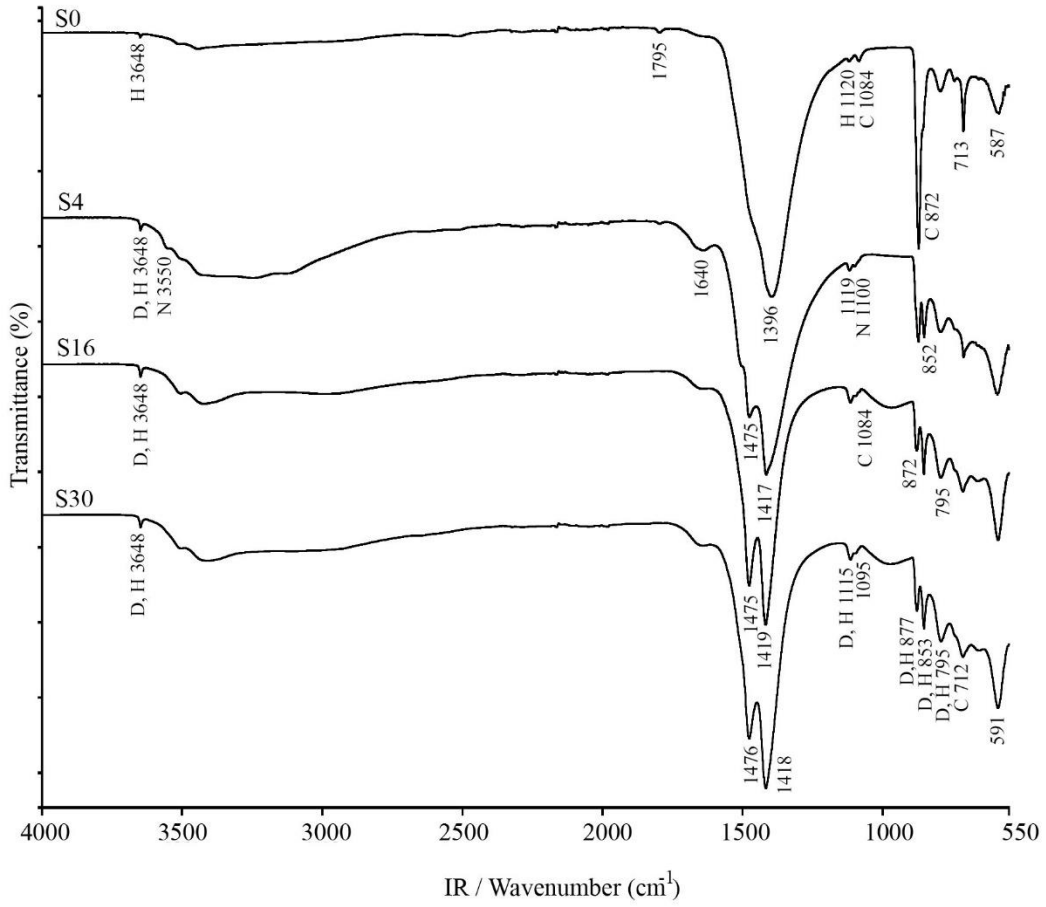

Figure C.5: Representative FT-IR spectra from experiment [S] in the range 4000-550 cm^{-1}. FT-IR spectrum S4 sample containing nesquehonite with OH band at 3555 cm^{-1}. Coding of mineral phases is as follows – C (calcium carbonate), D (dypingite), H (hydromagnesite), N (nesquehonite).[4]

[4] Calcite IR spectrum shows 1393 cm^{-1} with a shoulder at 1403 cm^{-1} (ν_3), 871 cm^{-1} with a subordinate weak peak at 847 cm^{-1} (ν_2), 712 cm^{-1} (ν_4) (Figure 3.5) Aragonite IR bands are found at 1085 cm^{-1} (ν_1), 875/870 cm^{-1} (ν_2), 1465 cm^{-1} (ν_3) (also reported at 1490 cm^{-1}), 712/699 cm^{-1} (ν_4). Nesquehonite IR bands 1097 cm^{-1} (ν_1), 852 cm^{-1} (ν_2), 1518/1469/1415 cm^{-1} (ν_3) (Huang and Kerr 1960; White 1974). The calcium carbonate phases showed spectral overlaps and therefore e.g. vaterite could not be distinguished by IR due to its low concentration and spectral overlap with calcite peaks. Hydromagnesite IR spectrum shows doublet at 1477 cm^{-1} and 1420 cm^{-1} (ν_3), very weak 1120 cm^{-1} and 1110 cm^{-1} (ν_1), medium intensity peaks at 888 cm^{-1} /853 cm^{-1} (with a shoulder at 870 cm^{-1})/796 cm^{-1} and 593 cm^{-1}.

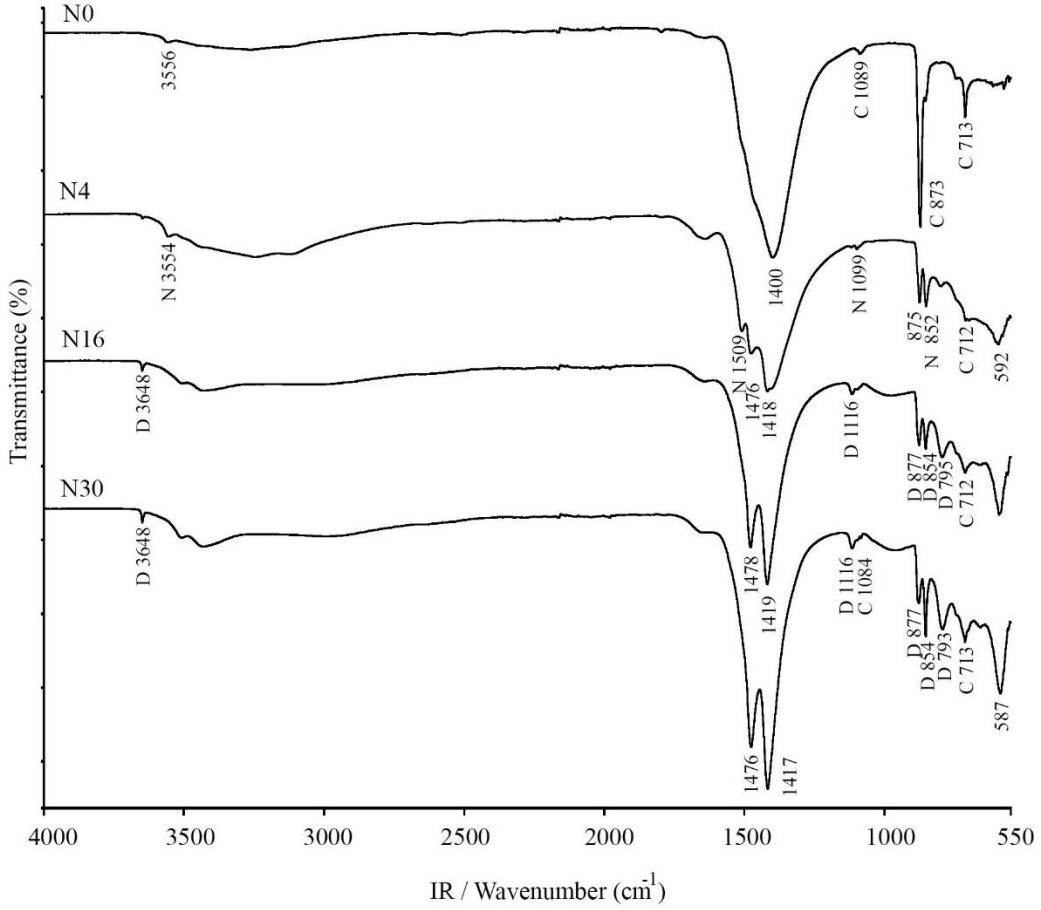

Figure C.6: Representative FT-IR spectra from experiment [N] in the range 4000-550 cm^{-1}. FT-IR spectrum of N4 sample containing nesquehonite with OH band at 3555 cm^{-1}. Coding of mineral phases is as follows –C (calcium carbonate), D (dypingite), N (nesquehonite).[5]

[5] Calcite IR spectrum shows 1393 cm^{-1} with a shoulder at 1403 cm^{-1} (ν_3), 871 cm^{-1} with a subordinate weak peak at 847 cm^{-1} (ν_2), 712 cm^{-1} (ν_4) (Figure 3.5) Aragonite IR bands are found at 1085 cm^{-1} (ν_1), 875/870 cm^{-1} (ν_2), 1465 cm^{-1} (ν_3) (also reported at 1490 cm^{-1}), 712/699 cm^{-1} (ν_4). Nesquehonite IR bands 1097 cm^{-1} (ν_1), 852 cm^{-1} (ν_2), 1518/1469/1415 cm^{-1} (ν_3) (Huang and Kerr 1960; White 1974). The calcium carbonate phases showed spectral overlaps and therefore e.g. vaterite could not be distinguished by IR due to its low concentration and spectral overlap with calcite peaks.

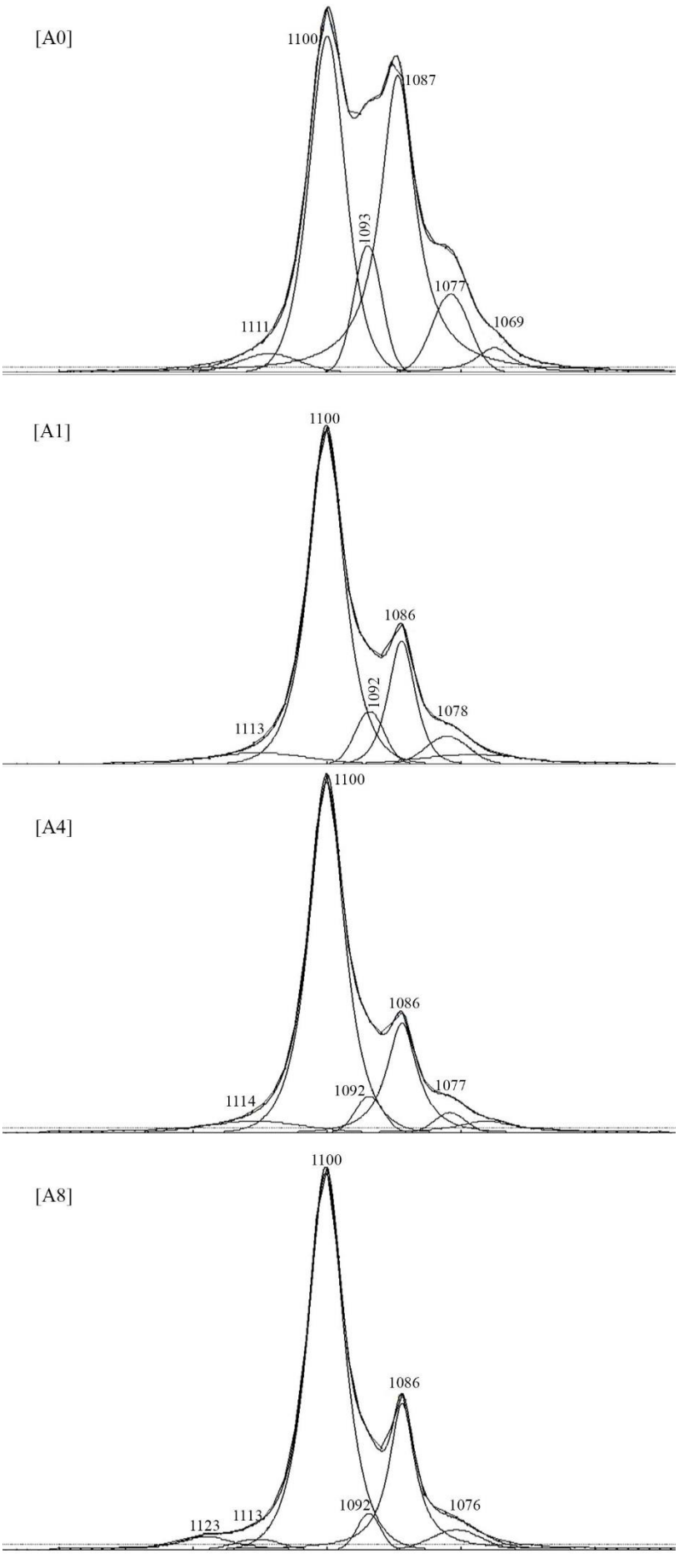

Figure C.7: Representative examples of peak fitted spectra in the range 1200 – 1000 cm^{-1} showing development of [A] series during first eight days (samples A0, A1, A4 and A8). Splitting of the ν_1 band for vaterite (with calcite impurity) has been also reported by Wehrmeister et al., (2009) and peak fitted with RS bands at positions 1091 cm^{-1} (vaterite), 1086 cm^{-1} (calcite impurity), 1081 cm^{-1} (vaterite) and 1075 cm^{-1} (vaterite).

Sample (A0) shows a shoulder on the (ν_1 1077 cm^{-1}) internal mode at 1069 cm^{-1} consistent with short lived traces of $CaCO_3 \cdot H_2O$ in the system.

Strong band at 1100 cm^{-1} belongs to nesquehonite, weak band at 1122 cm^{-1} belongs to dypingite-type / $Mg_5(CO_3)_4(OH)_2 \cdot xH_2O$ phases. Band at 1113 cm^{-1} coincides with chlorartinite (RRUFF database).

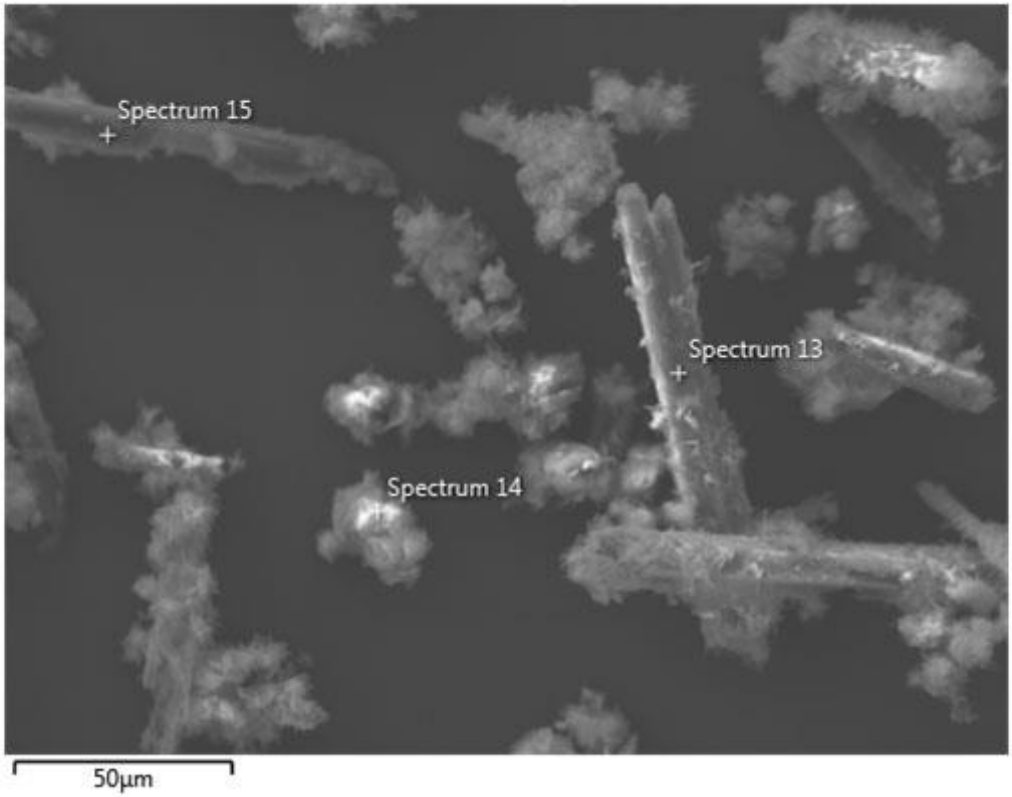

Figure C.8: Representative example of EPMA analysis – Electron image of sample A1 showing analysed carbonate mineral phases. Details of elemental analysis and plots are shown below (Figures C.9, C.10 and C.11, Tables C.1, C.2 and C.3).

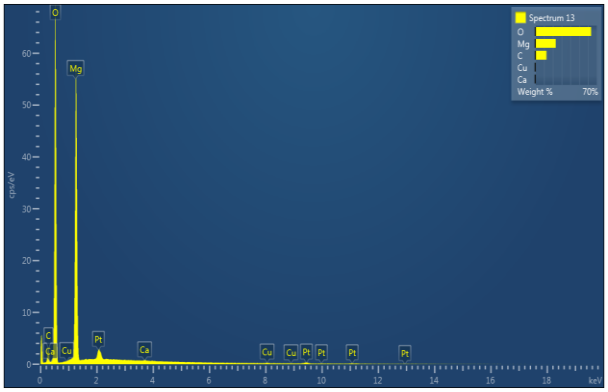

Element	Apparent Concentration	k Ratio	Wt%
C	2.32	0.02321	12.85
O	84.89	0.28567	63.55
Mg	24.04	0.15945	23.26
Ca	0.12	0.00105	0.08
Cu	0.30	0.00302	0.26
Total:			100.00

Fig. C.9: Elemental analysis -sample A1, spectrum 13. Tab. C.1: Composition – A1 spectrum 13.

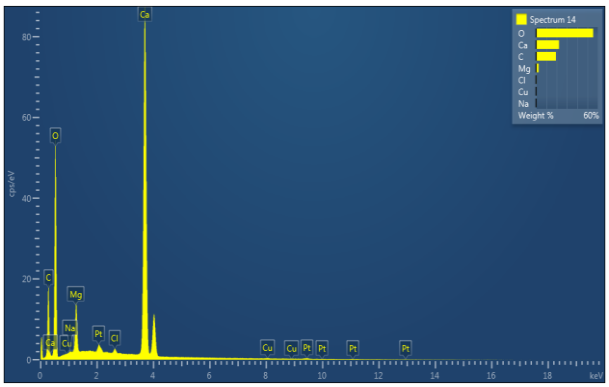

Element	Apparent Concentration	k Ratio	Wt%
C	14.66	0.14656	19.29
O	66.87	0.22503	55.54
Na	0.18	0.00076	0.08
Mg	5.25	0.03481	2.46
Cl	0.66	0.00573	0.21
Ca	75.17	0.67166	22.28
Cu	0.35	0.00351	0.13
Total:			100.00

Fig. C.10: Elemental analysis -sample A1, spectrum 14. Tab. C.2: Composition –A1 spectrum 14.

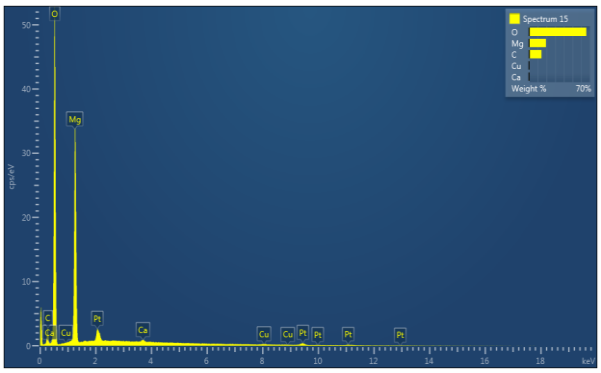

Element	Apparent Concentration	k Ratio	Wt%
C	2.11	0.02113	14.25
O	64.99	0.21870	65.86
Mg	14.64	0.09712	19.39
Ca	0.26	0.00230	0.24
Cu	0.23	0.00227	0.26
Total:			100.00

Fig. C.11: Elemental analysis - sample A1, spectrum 15. Tab. C.3: Composition – A1 spectrum 15.

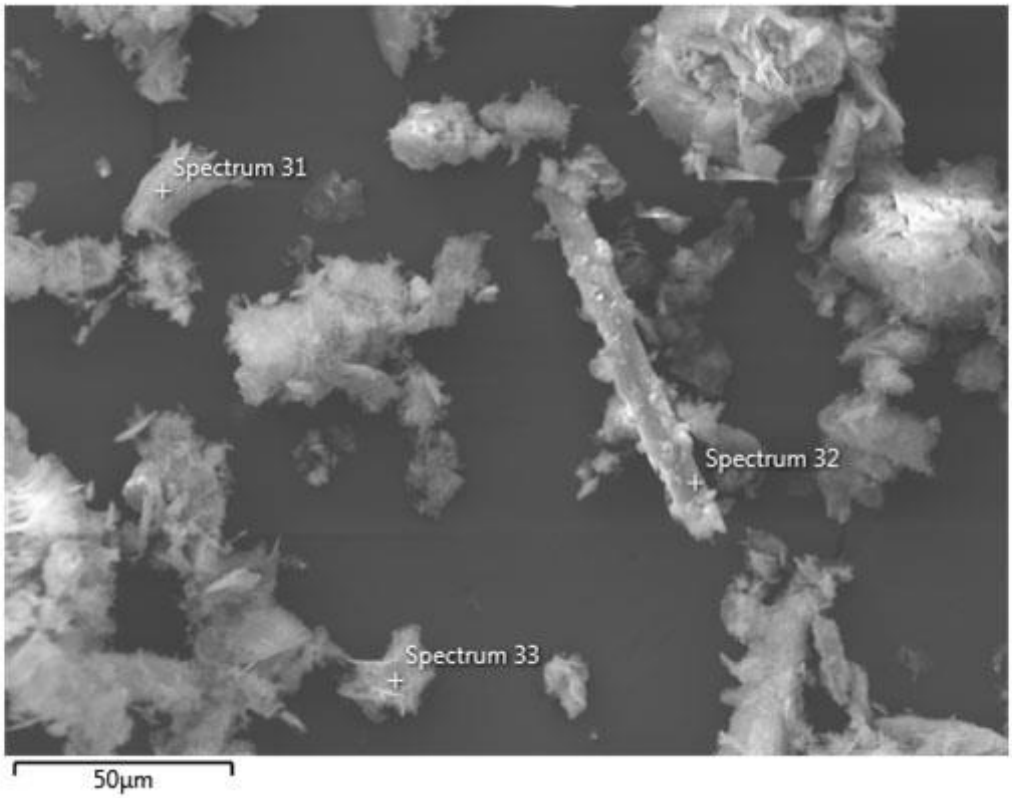

Figure C.12: Representative example of EPMA analysis – Electron image of sample A20 showing analysed carbonate mineral phases. Details of elemental analysis and plots are shown below (Figures C.13, C.14 and C.15, Tables C.4, C.5 and C.6).

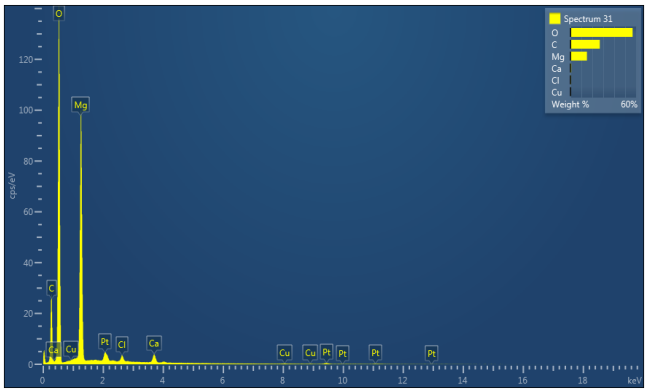

Element	Apparent Concentration	k Ratio	Wt%
C	22.57	0.22568	26.81
O	172.16	0.57932	56.84
Mg	42.31	0.28063	15.10
Cl	1.32	0.01153	0.39
Ca	2.75	0.02454	0.74
Cu	0.36	0.00358	0.12
Total:			100.00

Fig. C.13: Elemental analysis - sample A20, spectrum 31. Tab. C.4: Composition – A20 spectrum 31.

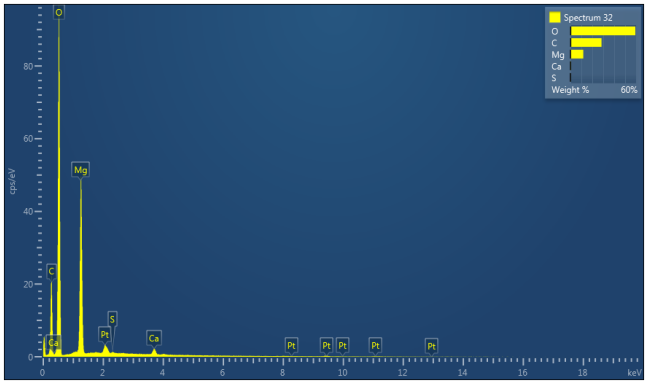

Element	Apparent Concentration	k Ratio	Wt%
C	17.82	0.17815	28.37
O	118.34	0.39821	59.32
Mg	21.03	0.13948	11.71
S	0.11	0.00098	0.05
Ca	1.34	0.01201	0.55
Total:			100.00

Fig. C.14: Elemental analysis - sample A20, spectrum 32. Tab. C.5: Composition – A20 spectrum 32.

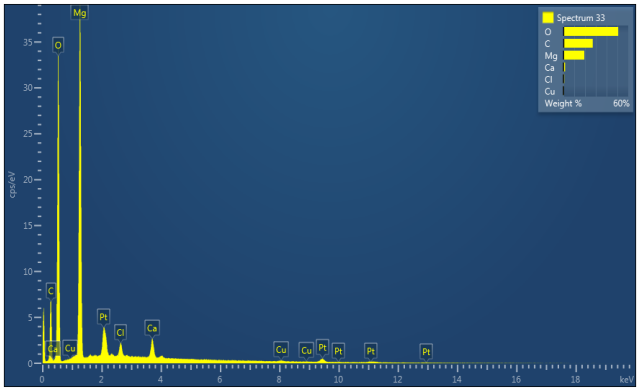

Element	Apparent Concentration	k Ratio	Wt%
C	5.98	0.05978	27.16
O	41.86	0.14086	50.75
Mg	16.75	0.11106	19.29
Cl	0.82	0.00716	0.82
Ca	1.76	0.01572	1.59
Cu	0.34	0.00345	0.39
Total:			100.00

Fig. C.15: Elemental analysis - sample A20, spectrum 33. Tab. C.6: Composition – A20 spectrum 33.